UNRAVELLING THE CONFORMATIONAL DYNAMICS OF α-SYNUCLEIN'S FOLDING PATHWAY BY HYDROGEN - DEUTERIUM EXCHANGE MASS SPECTROMETRY IN THE PRESENCE OF PHOSPHOLIPID NANODISCS

IRINA OGANESYAN

A THESIS SUBMITTED TO THE FACULTY OF
GRADUATE STUDIES IN PARTIAL FULLFILMENT
OF THE REQUIREMENTS FOR THE DEGREE OF
MASTER OF SCIENCE

GRADUATE PROGRAM IN CHEMISTRY
YORK UNIVERSITY
TOROTO, ONTARIO

August 2018

Abstract

Conformational changes of the α-synuclein protein during docking into a phospholipid membrane is suspected to play a central role in neuronal cell death during Parkinson's disease. This intrinsically disordered protein obtains its secondary helical structure through a pathway of transition states. These states, when improperly folded, are prone to stack into hydrophobic β-sheets, which later lead to the formation of fibrils and Lewy bodies – the hallmarks of Parkinson's. The ability to elucidate key transition intermediates of α-synuclein will clarify the mechanism used in the development of this disease and help facilitate the screening of drugs for the treatment of all α-synucleinopathies. In this research, Time-Resolved Hydrogen/Deuterium Exchange Mass Spectrometry coupled with the nanodiscs technology as artificial membrane was employed to unravel structural behaviour of this protein in the presence of phospholipid bilayer. As a result, the conformational behaviour of αSN indicated rather a transient interaction with phospholipid bilayer than binding to the nanodisc. The key regions of the most structural rearrangements during the interaction with the lipid membrane were identified and were consistent with the published literature. Based on the results of the kinetic HDX studies, the data proposed an evidence for the structural intermediate of αSN which was proposed in different theories on αSN's conformational behaviour *in vivo*.

Acknowledgements

This work would not be possible without a great help and sincere support of many people I have had the pleasure to meet during my academic career. I would like to express my very great appreciation to my supervisor, Dr. Derek Wilson, for his valuable and constructive suggestions during the planning and development of this research work. Special thanks should be given to my research supervisors – Dr. Gerald Audette, Dr. Mark Bayfield and Dr. Yi Sheng for their patient guidance, enthusiastic encouragement and useful critiques of this research work. I wish to acknowledge the help provided by Anurag Tandon and his colleagues at Tanz Centre for Research in Neuro-degenerative Diseases on expression protocols and samples of αSN, as well as, Dr. Gerald Audette for kindly providing plasmids for MSPs. I am particularly grateful for the assistance given by Howard Hunter in NMR studies. I would also like to extend my thanks to Andrew James in Sanofi Pasteur for introducing me to the field of proteomics. And, of course, my deepest appreciation goes for people that worked side by side with me every day – Cristina Lento, Kerene Brown, Shaolong Zhu, Peter Liuni, Shenbaga Moorthy, Ruth Knox, Lisa Szymkowicz, Lucienne Nouchikian, Xiaojing Huang, John Van Nostrand, and Ayat Yaseen. It has been a great honor to work with you and I have learned so much during these two years from each of you. Last, and definitely not least, I would like to say my biggest "thank you" to my family: my parents - Lidiya Tsvetkova and Artur Oganesyan, my sister – Bela Oganesian, and my boyfriend – Minhao Zhang. Thank you so much for being with me at the highest and lowest moments of my life during this academic career. There are no words to describe how important you were for the development of this research. Thank you all very much!

TABLE OF CONTENTS

CHAPTERS

LIST OF TABLES

LIST OF FIGURES

LIST OF ABBREVIATIONS

Alternative Splicing (AS)

Alpha-Synuclein (αSN)

Alzheimer's Disease (AD)

Ammonium Persulfate (APS)

Amyloid β-Protein (Aβ)

Apolipoprotein A-I (Apo-AI)

Bovine Serum Albumin (BSA)

Cetyltrimethylammonium Bromide (CTAB)

3-[(3-Cholamidopropyl)-Dimethylammonio]-1-Propanesulfonate (CHAPSO)

Circular Dichroism (CD)

Collision Energy (CE)

Column Volume (CV)

Critical micelle concentration (CMC)

Dihexanoylphosphatidylcholine (DHPC)

3,4-Dihydroxyphenylacetic Acid (DOPAC)

Dimyristoylphosphatidylcholine (DMPC)

Electron Capture Dissociation (ECD)

Electrospray Ionization (ESI)

Formic acid (FA)

Gamma-Aminobutyric acid (GABA)

Gamma (Γ)-Glutamyl Carboxylase (GGCX)

High-Affinity Consensus Propeptide (pCon)

High Density Lipoproteins (HDL)

Hydrogen/Deuterium exchange (HDX)

Intrinsically disordered protein (IDP)

Intrinsically Disordered Protein Regions (IDPRs)

Ion mobility spectrometry (IMS)

Isopropyl β-D-1-Thiogalactopyranoside (IPTG)

Kanamycin (Kan)

Lewy bodies (LB)

Lewy neurites (LN)

Lipid-to-Protein (L:P) ratio

Luria-Bertani (LB)

Mass spectrometry (MS)

Matrix Assisted Laser Desorption/Ionization (MALDI)

Membrane Proteins (MPs)

Membrane Scaffold Proteins (MSPs)

MWCO – Molecular Weight Cut-Off

Multiple System Atrophy (MSA)

Non-Amyloid-Beta Component (NAC)

Nuclear Magnetic Resonance (NMR)

Parkinson's Disease (PD)

Phosphatidylethanolamines (PEs)

Phenylmethylsulfonyl Fluoride (PMSF)

Phosphatidylglycerols (PGs)

Phosphatidylinositols (PIPs)

Phosphatidylserines (PSs)

Poly-Methyl Methacrylate (PMMA)

Post-translational modifications (PTMs)

Size Exclusion Chromatography (SEC)

Sodium Dodecyl Sulphate (SDS)

Sodium Dodecyl Sulfate Polyacrylamide Gel Electrophoresis (SDS-PAGE)

Styrene Maleic Acid Co-Polymer (SMA)

Tetramethyl Ethylenediamine (TEMED)

Time-of-Flight (TOF)

Time-Resolved Electrospray Ionization HDX-MS (TRESI-HDX)

Trifluoroacetic acid (TFA)

Trisaminomethane (Tris)

Vitamin K Dependent (VKD)

LIST OF PUBLICATIONS

1. Oganesyan, I., Lento, C. & Wilson, D. J. Contemporary hydrogen deuterium exchange mass spectrometry. Methods (2018). doi:10.1016/J.YMETH.2018.04.023

Chapter 1: Introduction

1.1. Hydrogen/Deuterium Mass Spectrometry (HDX-MS) – a Powerful Tool for Studying Conformational Dynamics of Proteins

1.1.1. Mass Spectrometry

Mass spectrometry (MS) is an analytical technique that ionizes molecules and measures these ions according to their specific mass-to-charge ratio (m/z) [1,2]. The history of MS started with the construction of the very first mass spectrometer termed "parabola spectrograph". In 1907 it was built by the Nobel Prize winner - J.J. Thomson on the basis of W. Wien studies on deflecting channel rays in a magnetic field [3,4]. In 1913, Thomson reported the first successful mass spectrometry result, a photographic plate with separate impact marks for the two isotopes Ne^{20} and Ne^{22} [4,5]. This marked the start of mass spectrometry as a scientific field! Up until the late 1980's, MS was mainly used for analysing low molecular weight molecules as no other method existed at the time for putting larger molecules (like biomolecules and their complexes) in the gas phase. In 1988 and 1989, K. Tanaka and J. B. Fenn were able to circumvent the problem of placing intact macromolecules in the gas phase and produce the two main Nobel Prize winning soft ionization techniques of today – Matrix Assisted Laser Desorption/Ionization (MALDI) and Electrospray Ionization (ESI), respectively [6–9]. Soft ionization techniques coupled with more and more advanced mass spectrometers was the start to a new direction in MS research - powerful analytical methods in life sciences and medicine. One of these young analytical techniques which emerged into the world of biochemistry 20 years ago was Hydrogen/Deuterium exchange (HDX) Mass Spectrometry.

1.1.2. Hydrogen Deuterium Exchange

HDX is a chemical reaction involving the substitution of a covalently bound labile hydrogen atom with deuterium [10]. The origins of HDX as a bioanalytical approach can be traced to the work of Linderstrøm-Lang and colleagues at the Carlsberg laboratories in 1950s, which focussed on HDX at the amide backbone of peptides/proteins [11,12]. Initially, the goal of their studies was measuring stability of hydrogen bonds involved in the formation of secondary protein structures using HDX [12–20]. Later, they recognized that exchange in the amide backbone of the protein relates to conformational changes, which was the first study of protein dynamics using this method [11,12,21,22]. Hence, the 'central dogma' of HDX was born –exchange at the amide backbone (hydrogens are shown in teal in Figure 1) of a protein reflects its conformational dynamics, which correlates to its fundamental properties and ultimately to biological function [12,23–31].

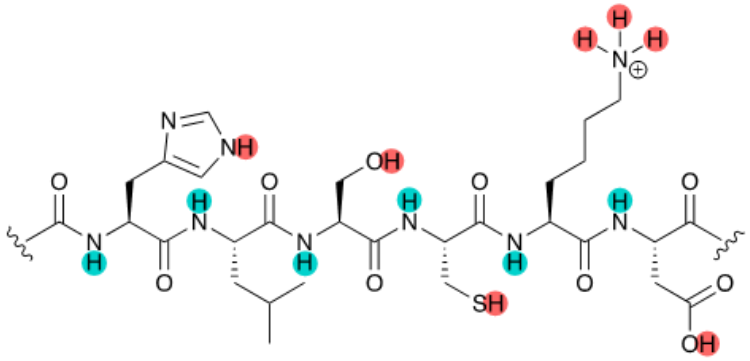

Figure 1. Different hydrogen types in the sample peptide His-Leu-Ser-Cys-Lys-Asp. The exchangeable backbone amide hydrogens are depicted in teal, and the labile side-chain protons are depicted in salmon-pink color. Carbon-bound unexchangeable hydrogens are not indicated.

Interestingly, HDX was primarily monitored by Nuclear Magnetic Resonance (NMR) until mass spectrometers were coupled with ESI and MALDI, but the rapid rise of HDX-MS related publications over the last 20 years is a testament to it's broad applicability in biochemistry, and its complementarity to the classical tools of structural biology [12,23–26,32]. Compared to HDX-NMR,

HDX-MS has the advantage of having virtually no size limitation and can require substantially less protein material, but it typically does not provide atomic-level resolution [27,33,34]. Modern HDX-MS combined with new separation and advanced MS technologies, such as ultra-high resolution mass separation, ion mobility spectrometry (IMS) and non-ergodic fragmentation, has become an essential tool in the investigation of protein-protein, protein-membrane, protein-small molecule interactions, as well as drug development, epitope mapping and bio-therapeutics [35–40].

1.1.2.1 HDX Fundamentals

HDX in a protein can occur at any site containing a labile hydrogen (-OH, -SH, -NH), but the amide hydrogens on the peptide backbone are by far the most commonly monitored in HDX experiments (Figure 1) [20–22,30,41,42]. These hydrogens are uniformly distributed along the polypeptide chain (except for prolines) and form critical hydrogen bonding networks within and between secondary structural elements of the protein, thus, even relatively subtle perturbations in the higher order structure of the protein will often affect the exchange rate of HDX at 'backbone' amides [20–22,30,41,42]. Also, at neutral pH, backbone amide protons undergo exchange at a rate that is amenable to measurement (*i.e.*, ms – days, depending on the extent to which the intrinsic rate is attenuated by structure) [44]. In addition, the exchange at amide backbones is highly quenchable at low pH and low temperature allowing for monitoring of the dynamics at various time scales [45,46].

The chemistry of proton transfer at unprotected amide hydrogens is catalyzed by acid, base or water in some cases [28]. In base-catalyzed HDX (predominant at pH above 3), the amide proton is removed by a hydroxide ion forming an amidate anion, which is then reprotonated by

deuterium oxide (Figure 2a). Acid catalysis (main below pH 3) has two competing pathways. The first possible mechanism involves deuteration of the amide nitrogen atom by D_3O^+, followed by proton abstraction by water, regenerating the acid (Figure 2b). However, since the amide oxygen is more basic than the amide nitrogen, the preferred pathway is initiated by the protonation of the amide oxygen atom, significantly acidifying the NH proton which is then removed by water, regenerating the acid (Figure 2c). The nitrogen atom in the resulting imidic acid is then deuterated by surrounding D_3O^+, and tautomerizes to the deuterated amide (Figure 2c).

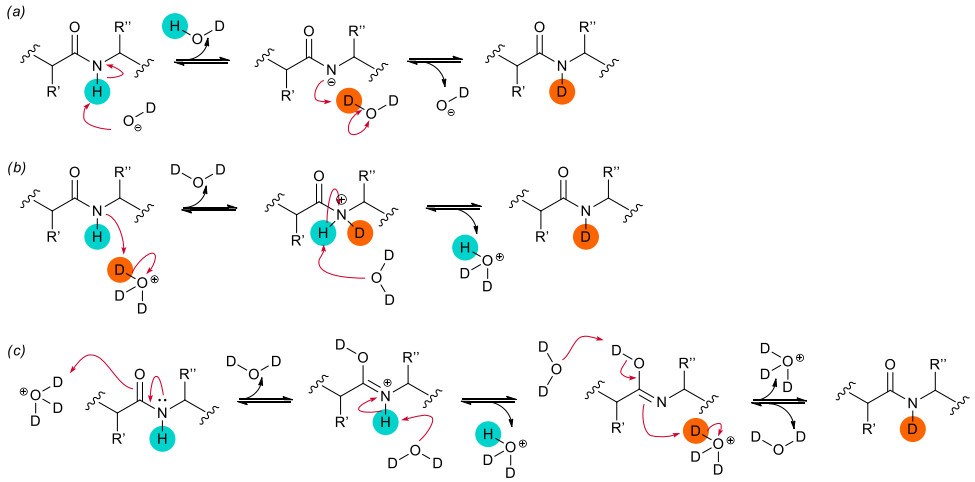

Figure 2. Schematic of base- and acid-catalyzed HDX of amide backbone protons in solution. (a) Base-catalysis, (b) acid-catalysis through N-protonation, (c) acid-catalysis via O-protonation.

The chemical HDX rate constant (k_{ch}) for the amide hydrogen follows equation (1):

$$k_{\mathrm{ch}} = k_{int,acid}[H_3O^+] + k_{int,base}[OH^-] + k_{int,water}[H_2O] \qquad (1)$$

where $k_{\mathrm{int,acid}}$ and $k_{\mathrm{int,base}}$ are the rate coefficients for the acid- and base-catalyzed exchange, and $k_{\mathrm{int,water}}$ is the intrinsic coefficient of water-catalyzed proton transfer [28,42]. The HDX rate is highly dependent on four factors – hydrogen bonding (strongest influence in folded proteins), solvent accessibility, pH and temperature [11,45,47,48,43,49]. Other important factors include steric effects of

nearby amino acid groups, solvent composition of the HDX reaction and pressure in the system [47,43,50].

Starting with temperature and pH, they define the "quenching conditions" – environmental settings that can significantly slow down the rate of HDX, so that accurate deuterium uptake profiles at various time points can be measured without the occurrence of back-exchange (loss of deuterium label) [12,25,32,51]. The usual quenching conditions are pH_{min} (pH 2.5-3) and 0°C which slows the exchange reaction up to five orders of magnitude compared to pH 7 and 23°C [26,30,31,33].

Solvent abstraction of the amide hydrogen is always a rate limiting step, therefore, amide hydrogen involved in stable hydrogen bonding or deeply buried within the protein interior may elongate HDX reaction times from milliseconds to days [45,47]. HDX kinetics in folded polypeptides follows a model that amides can exist in either an exchange-incompetent (N-H_{closed}) state due to hydrogen bond participation or solvent inaccessibility, or exchange-competent (N-H_{open}) state where the proton can be abstracted [13,52]. However, proteins are not static, and N-H_{closed} hydrogen can become N-H_{open} through various levels of structural unfolding or "breathing motions" [23,53]. In this case, the model of HDX kinetics for a folded protein can be depicted as equation (2):

$$NH_{\text{closed}} \underset{k_{\text{cl}}}{\overset{k_{\text{op}}}{\rightleftharpoons}} NH_{\text{open}} \xrightarrow{k_{\text{ch}}} ND_{open} \underset{k_{\text{op}}}{\overset{k_{\text{cl}}}{\rightleftharpoons}} ND_{\text{closed}} \quad (2)$$

where k_{op} and k_{cl} are the rate constants for the opening and closing motions of the protein and k_{ch} is the intrinsic ('chemical') rate of exchange. Since proteins in solution are in equilibrium between open and closed states, the rate of HDX is mainly affected by the rates of unfolding/folding (k_{op}, k_{cl}) and chemical HDX rate constant, k_{ch}. Therefore, the exchange rate

constant (k_{HDX}) of amides in structured proteins, where hydrogen bonding and solvent accessibility factors influence the rate of HDX, can be expressed by equation (3):

$$k_{\text{HDX}} = \frac{k_{\text{op}} \times k_{\text{ch}}}{k_{\text{op}} + k_{\text{cl}} + k_{\text{ch}}} \tag{3}$$

where K_{op} is the equilibrium constant for the transition from 'open' state to 'closed' state [23,53]. When $k_{\text{op}} >> k_{\text{cl}}$, the protein stays in the unfolded state and HDX is governed mainly by k_{ch} [21,53]. However, under native-like conditions, $k_{\text{op}} << k_{\text{cl}}$ as the hydrogen bonding network for much of the protein will be highly stable. In this case, the observed hydrogen exchange rate (k_{HDX}) simplifies to equations (4), (5), and (6):

$$k_{\text{HDX}} = \frac{k_{\text{op}} \times k_{\text{ch}}}{k_{\text{cl}} + k_{\text{ch}}} \tag{4}$$

$k_{\text{cl}} \ll k_{\text{ch}}$ ↙ $k_{\text{cl}} \gg k_{\text{ch}}$ ↘

$$k_{\text{HDX}} = k_{\text{op}} \ (\text{EX1}) \qquad k_{\text{HDX}} = \frac{k_{\text{op}}}{k_{\text{cl}}} \times k_{\text{ch}} = K_{\text{op}} k_{\text{ch}} \ (\text{EX2}) \tag{5), (6}$$

Therefore, the two kinetic limits of exchange are: 1) $k_{\text{cl}} << k_{\text{ch}}$ where refolding of the protein to the NH_{closed} state is much slower than the rate of HDX, and 2) $k_{\text{cl}} >> k_{\text{ch}}$ where refolding of the protein occurs much faster than HDX. These two regimes are called EX1 ($k_{\text{cl}} << k_{\text{ch}}$) and EX2 ($k_{\text{cl}} >> k_{\text{ch}}$), respectively, and can be depicted in MS spectra (Figure 3). In the EX2 regime (most common), the rate of HDX is much slower than the rate of refolding to the NH_{closed} state, so only a fraction of the available amide hydrogens will undergo deuterium exchange before the closing event. This results in a gradual increase in the m/z centroid of the isotopic envelope over time, where this isotopic envelope represents only one population of averaged closed and open states (Figure 3a) [12,54]. In the EX1 regime, refolding process to the closed state is slower than the

exchange rate, so almost all amides become fully exchanged in a correlated manner. This is evidenced by a bimodal distribution - two m/z envelopes representing a fully-exchanged protein population (higher m/z species), and a non-exchanged one (lower m/z envelope) (Figure 3b). Over the course of deuterium exchange, all non-exchanged protein populations shift to the exchanged species (Figure 3b) [12,54].

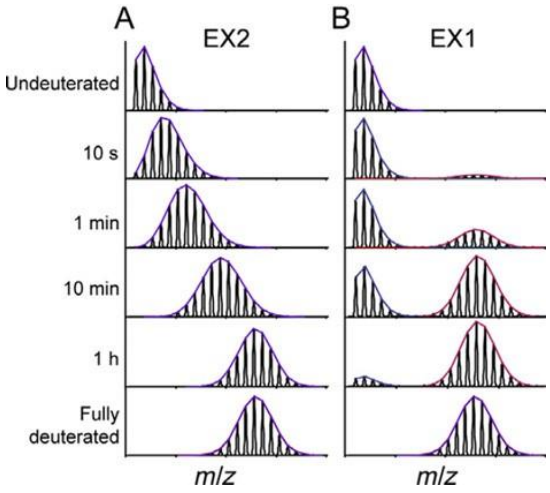

Figure 3. MS spectra of (A) EX2 and (B) EX1 kinetics during HDX-MS. Adapted from Guttman and Lee [54].

1.1.2.2. Common HDX-MS Workflow

The workflow of HDX-MS experiments can vary substantially depending on the information that a researcher wants to obtain, as well as, the type of instrumentation that is accessible. However, there is a common configuration of steps in HDX-MS, outlined in Figure 4, that gives a general overview of the most familiar type of HDX-MS experiment – "bottom up" HDX-MS. The workflow starts with sample preparation – the protein can be obtained through various means of expression and/or purifications and subsequently exchanged into a MS compatible buffer [12,51]. Second step is HDX labelling – the protein sample is diluted into deuterated buffer, often a 10 to

20-fold dilution, in order to initiate isotopic exchange on the dynamic portions of the protein (Figure 4) [12,51].

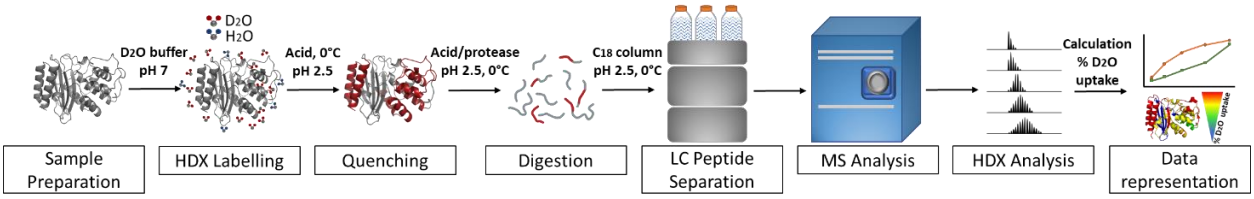

Figure 4. The outline of a general HDX-MS bottom-up workflow. It starts with sample preparation followed by HDX labelling and, after some chosen time, quenching with acid at 0°C and pH 2.5. Next, protein is digested into peptides which get desalted and separated thought C_{18} column attached to an LC. Finally, the percentage of deuterium uptake of each peptide is calculated, and results can be presented in the form kinetic plots or mapped onto a 3D protein structure.

Next, quenching of the HDX reaction is achieved by adding a pre-chilled (0°C) solution at pH ~2.5 using either trifluoroacetic acid (TFA) or formic acid (FA) (Figure 4) [12,51]. Quenching is followed by digestion of the protein which is usually implemented as part of the LC workflow (online digestion). Here, labelled protein sample first gets digested online using a LC pepsin column, and resulting peptides are subsequently desalted and concentrated in a trap column by washing with a low percentage of acetonitrile [12,51]. This step is undertaken in a protic solvent resulting in the potential back-exchange of the labeled backbone amides, the first two amides undergo a rapid HD exchange and, therefore, omitted in analysis [12,51]. Finally, peptides are released from the trap column to an analytical C_{18} column where they are separated via hydrophobic interactions with C_{18} stationary phase and eluted with a gradient of organic solvent in a 'reversed-phase' fashion [12,51]. Eluted peptides are then ionized by electrospray and usually analysed by two main types of mass analyzers – time-of-flight (TOF) and orbitrap [55,56]. Last but not least, the percentage of deuterium uptake of each peptide is calculated based on the isotopic distribution and results can be displayed in many forms, most commonly via kinetic plots and

heat-mapped 3D protein structures (Figure 4). To achieve multi-dimensional separation of labelled peptides, IMS can be coupled to MS measurements. The ion mobility cell can be thought of as a gas-phase analogue of gel electrophoresis, as it separates ions based on their size [57]. IMS separation of peptides was used in this research to increase spatial resolution.

1.1.3. Time-Resolved Hydrogen-Deuterium Exchange Mass Spectrometry (TR-HDX)

Conventional HDX-MS discussed in section 1.1.2 is a powerful method to study protein conformational dynamics on a second to minute time scale, as it can go no lower than 10 s for the HDX reaction to occur before quenching. However, many of the folding intermediates during a folding pathway of a protein assemble on a millisecond to second scale which stroke a need for millisecond HDX-MS methodology. As with other HDX applications mentioned earlier, the first millisecond HDX studies were done using NMR in late the 1980s by Udgaonkar and Baldwin [58], and Roder *et al.* [59] where the early folding intermediates of ribonuclease A (RNaseA) and cytochrome c (cyt c) were described. Dharmasiri and Smith were the first to couple millisecond HDX to MS in their 1996 report studying the folding pathway of cyt c [60]. Short mixing times were accomplished using a flow-quench protein fragmentation/MS method which allowed for measuring isotopic exchange rates of the most rapidly exchanging amide hydrogens [60]. Further development in this field occurred in the Konermann Lab in 2003, when Simmons *et al.* introduced a continuous flow millisecond HDX-MS device to study the conformational dynamics of myoglobin (Mb) under mildly denaturing conditions (27% acetonitrile, pH 9.3) with development of a detailed kinetic model [61]. In order to provide spatial information after labeling, the Wilson Lab coupled this continuous flow millisecond HDX-MS device onto a microfluidic

platform accommodating online proteolytic digestion [62–64]. This time-resolved electrospray ionization HDX-MS (TRESI-HDX) method from the Wilson Lab has been used in current research (with some further modifications, see section 2.8) and the general setup is depicted in Figure 5. The millisecond HDX reaction time is possible due to a rapid kinetic mixer where protein, flowing from the inner yellow channel with a sealed end and 2mm notch, mixes with deuterium flowing from the outer channel (Figure 5) [62–65]. Depending on how far the protein channel is pulled back, protein and deuterium react at different time points before being quenched by acid (Figure 5) [62–65]. The deuterated quenched protein sample is then digested in a downstream reaction chamber by acid resistant proteases (pepsin, protease XII, etc.) linked to agarose beads, and, resulting peptides are introduced to MS through ESI (Figure 5) [62–65].

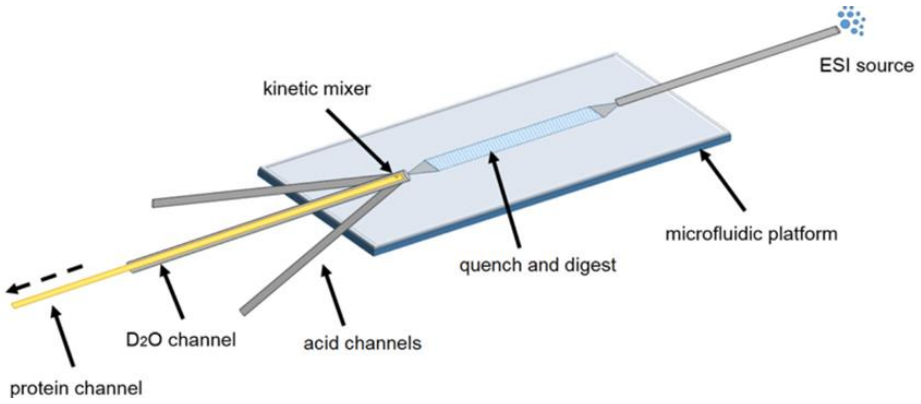

Figure 5. A schematic representation of a continuous flow TRESI-HDX-MS setup on a microfluidic chip. From left to right, protein sample is introduced in the inner (yellow) capillary and exits through the kinetic mixer to meet with deuterium flowing through the outer channel. The protein line can be pulled back (dotted black arrow) allowing for various HDX reaction times. Acid channels quench HDX and the protein is digested in a downstream reaction chamber. Peptides are ionized by ESI and introduced into the MS. Adapted from Lento *et al*. 2016 [65].

TRESI-HDX-MS has proved its various applications with numerous research publications depicting millisecond conformational changes in protein-RNA/DNA interaction, enzymatic transition states, intrinsically disordered protein folding/misfolding intermediates, and antibody-

antigen interactions [37,38,66–68] . For example, Brown and colleagues were able to characterize the changes in dynamics at a 2 s time scale during RNA binding to RRM2 motif of human La protein, and found some key differences in conformational dynamics of La protein when it binds to single-stranded versus double-stranded RNA [38]. In another study by Zhu *et al.* in 2015, TRESI-HDX-MS was used to elucidate the shifts in conformational dynamics of intrinsically disordered protein (IDP), tau, when it is hyperphosphorylated [69]. The HDX measurements were taken from 42 ms to 12 s showing some increases in deuterium uptake in a few hexapeptide regions of hyper-phosphorylated tau (compared to native), suggesting a more open and extended confirmation which can easily be rationalized as enhancing amyloidogenic propensity [69]. Here, Zhu and colleagues have shown that TRESI-HDX-MS is a powerful approach for probing the structural dynamics of non- to weakly structured regions of proteins on a millisecond to second scale and ideal for studying IDPs.

1.1.3.1. Application: Intrinsically Disordered Protein Domains/Proteins

IDPs are a class of proteins lacking a fixed or ordered three-dimensional structure, meaning that they can obtain a variety of conformational ensembles with no prevalence to any particular 3D structure [70,71]. IDPs have become an important target for structural dynamics research – only recently it was noticed how crucial they are in transcriptional regulation, translation and cellular signal transduction [71–75]. Even though many IDPs have been discovered in last few decades, not many experimental analytical tools are available for characterization of their behaviour [70,71]. X-ray crystallography cannot provide information on unstructured states, but can only indicate if there is an unstructured region by showing the presence/absence of electron density in these

areas [70,71,76]. NMR is by far the key experimental method for obtaining systematic site-specific information on IDPs, but, again, limitations of the NMR technique like molecular size restrictions and the large amount of sample required make it difficult to study different variations of IDPs, especially their transient interactions with protein complexes [27,33,34]. Alternatively, TRESI-HDX-MS has no size limitations, works with even nanomolar concentrations of protein, and is able to provide good spatial resolution (peptide level to even amino acid resolution if using an electron capture dissociation, ECD, cell in MS) [69,77,78]. Last but not least, TRESI-HDX-MS provides conformational dynamics information on a millisecond scale for studying the transition state species of IDPs and the most favourable conformational ensembles if they exist [69,77,78]. TRESI-HDX-MS provides a great alternative to NMR and other conventional bioanalytical techniques (circular dichroism (CD), hydrodynamic measurements, fluorescence spectroscopy, vibrational CD spectroscopy and RAMAN spectroscopy) making it a powerful tool to characterize the disordered structural behaviour of IDPs.

1.2. Nanodisc Technology – Soluble Lipid Bilayer Systems for Structural and Functional Studies of Membrane Proteins

1.2.1. Major Complication in Membrane Protein Structural Biology Research

The importance of membrane proteins (MPs) in biological processes is huge. Around 30% of all proteins in eukaryotic cells are MPs, and almost 50% of all known small molecule drugs target this class of proteins [79–81]. MPs are responsible for many vital functions in a cell; they are receptors that relay signals between the cell's internal and external environments, they are transporters that move molecules and ions across the membrane, many are enzymes with various catalytic functions, while others play a role in cell adhesion and other processes crucial

for cell's survival [81–87] . However, little is known about this class of protein, as they present a great challenge in structural biology research. The difficulties in studying MPs arise due to many reasons. Since MPs are present at very low concentrations, it is quite rare that a single protein dominates the constituent of a membrane, therefore, the MPs' yield from extraction and purification processes is quite low [88,89]. Although genes for MPs can be cloned into bacterial plasmids for further recombinant expression, post-translational modifications (PTMs) required for some MPs are not attainable in these expression systems [88–90]. The other problem with MPs is that they are a part of a very complex and unique matrix – the mosaic bilayer of a membrane, which prevents standard biophysical techniques like NMR, CD, X-ray from obtaining high resolution results [88,89]. In many cases, MPs must be taken out from it's native mosaic bilayer which can lead to a change in their structural properties [88,89]. Also, purification protocols for the extraction of MPs can be very challenging and time consuming [88,89]. Last but not least, the hydrophobic character of MPs prevents their solubilization in aqueous solutions leading to aggregation issues starting from the purification process up until the final steps of analytical experiments that are mostly solution-based [88,89]. Despite all the difficulties with studying MPs, they still remain an active target of research which has been rapidly developing over the last few decades.

1.2.2. "Old Generation" Artificial Membrane Systems

Since no conventional biophysical technique is sufficient enough to deal with complex mosaic bilayers, MPs must be transferred to a more tractable environment for experimental study. The first of these type of environments were detergents – amphipathic molecules consisting of polar

head groups and hydrophobic chains which can spontaneously form spherical micellar structures in aqueous solutions. There are many types of detergents that have been developed over the years which are now classified into four modules based on their charge state: 1) anionic (for example sodium dodecyl sulphate (SDS) and the bile salts such as cholate and deoxycholate), 2) cationic (cetyltrimethylammonium bromide or CTAB), 3) zwitterionic (3-[(3-cholamidopropyl)-dimethylammonio]-1-propanesulfonate or just CHAPSO), and 4) nonionic (like the polyoxyethylene series of detergents such as Triton X-100) [88,89,91,92]. Without going into the details about each module, it is worth noting that nonionic and zwitterionic detergents have become very popular in MP research as proteins retain their function after solubilization [88,89,91,92]. The basic principle of MP extraction by detergents is represented in Figure 6.

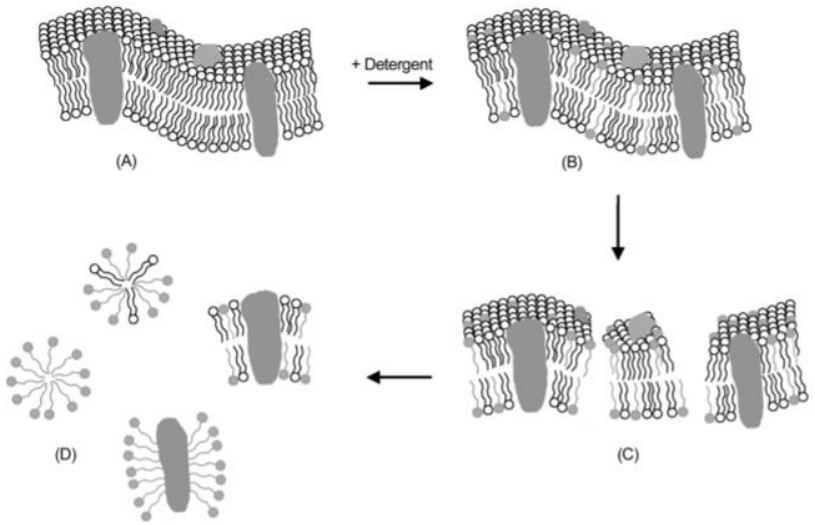

Figure 6. A schematic representation of various stages of solubilization of biological membranes by detergents. Biological membrane (A) is mixed with detergent starting the process of perturbation of lipid bilayer with detergent molecules followed by penetration into the membrane (B). More and more detergent molecules penetrate the membrane resulting the in membrane bilayer being disrupted (C). Finally, high detergent concentration forms heterogeneous complexes of detergent, lipid and protein - mixed micelles of lipid and detergent and protein and detergent (D). Adapted from Kalipatnapu and Chattopadhyay [91].

Assuming detergent concentration is equal or above the critical micelle concentration (CMC), detergent molecules first saturate the lipid bilayer (Figure 6B), then solubilize both the hydrophobic and amphipathic molecules in the solution (Figure 6A) resulting in the formation of water-soluble protein-detergent complexes, detergent and detergent-lipid micelles (Figure 6C) [91,92]. Despite having many advantages like great variability of detergents and relatively low cost, detergent systems are a poor mimic of the native membrane environment and frequently destabilize and inactivate protein over time [91]. In addition, many detergents can complicate spectra or exhibit incompatibility with MS, NMR or X-ray and other techniques. Especially in the case of MS, most detergents cause signal suppression of a MP sample – detergents compete for maximum ionization potential in ESI and detection capability of a protein lowers [93,94]. In order to resemble a native-like environment for MPs, the field moved towards mixed lipid – detergent systems like bicelles and liposomes (Figure 7).

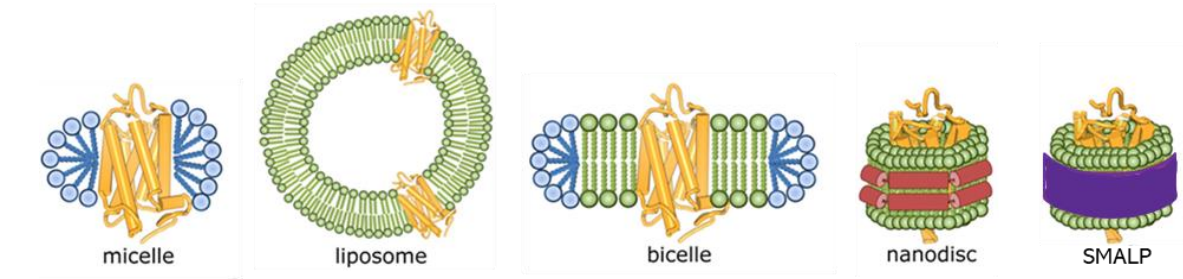

Figure 7. A cartoon representation of some key lipid membrane mimetics. From left to right: detergent micelle, liposome, lipid – detergent bicelle, non-covalent structure of lipid and membrane scaffold protein - nanodisc, and styrene maleic acid co-polymer lipid particle (SMALP). Detergent is represented by blue color ball pins, lipid by green ball pins, and organic polymers by dark blue bands. Cylinders represent α-helices of proteins. Adapted from Milić and Veprintsev [95].

Bicelles can be described as microscopic disks where a bilayer patch of lipid is encircled by a "rim" of detergent molecules (Figure 7) [89,96]. Bicelles are prepared by mixing long-chain lipids

such as dimyristoylphosphatidylcholine (DMPC) with shorter chain (tail) edge-stabilizing detergents like CHAPSO in 4:1 to 1.5:1 lipid:detergent molar ratios [89,96]. Detergents can be completely eliminated from bicelles if short chain lipids such as dihexanoylphosphatidylcholine (DHPC) is used as a "rim" making this membrane mimetics even more native-like [89,96]. Bicelles provide several advantages over detergent micelles. They represent a lipid bilayer which is a more native-like environment for structural studies of MPs, and they are much easier to work with using NMR and X-ray techniques since less detergent is present and bicelle aggregate sizes are sufficiently small to be aligned in a magnetic field [89,96]. However, bicelles exhibit many disadvantages especially for MS research: 1) even smaller amount of detergent will cause signal suppression, 2) the lipid-detergent or lipid-lipid ratios must be strictly preserved during the experiment to prevent bicelle disassembly and avoid any phase transitions, 3) the current lipid compositions of bicelles is very limited, as only DMPC-CHAPSO and DMPC-DHPC works [97,98].

Another popular lipid membrane mimetic are liposomes (Figure 7) – small artificial vesicles of spherical shape that can be created from natural phospholipids with the help of detergents [89,99]. Just like bicelles, liposomes create much more of a native-like environment for MPs (lipid bilayer), but they are more stable, and they exhibit more variation in lipid composition [89,99]. But then again, the reconstitution of MPs in liposomes is though a detergent-mediated pathway leaving detergents to interfere with downstream MS or NMR analysis [89]. Also, there is always a concern of how evenly the MPs are distributed in liposomes and in what exact direction and topology – all of these factors affect MPs function. For example, membrane transporters must be inserted in a single transmembrane orientation to ensure that pumping of substrates occurs in the correct direction: inside-out or outside-in [100]. Detergent micelles and lipid–detergent systems like

bicelles and liposomes are good tools for solubilizing MPs for further structural and functional studies, but as discussed, they also have many disadvantages. The most critical disadvantage is that these artificial membranes disassemble at lower concentrations [101]. This problem is most notable in MS studies as better signal-to-noise ratio in modern mass spectrometers is obtained on lower a concentration (nM to μM) scale. Therefore, the search for more advanced artificial membranes became even more important in recent years leading to the development of "new generation" membrane mimetics.

1.2.3. Nanodiscs – "New Generation" Artificial Membrane Systems

Nanodiscs are small nanoscale lipid bilayers wrapped around by a belt of one or two α-helical proteins (Figure 7) [102–106]. This technology was developed by Sligar and coworkers at the University of Illinois in 2007 [105]. Seeking for more "natural" membrane mimetics, the concept of nanodiscs originated from the architecture of high density lipoproteins (HDL) in human cells [104]. These particles are key transporters of fat molecules around the body and resemble a ball shape of various sizes containing cholesterol esters, lipids and proteins [104]. However, the transient form of HDLs is roughly discoidal and stabilized by the amphipathic apolipoprotein A-I (Apo-AI) [104]. The Sligar lab genetically engineered the Apo-AI sequence to produce a set of different sized amphipathic helical proteins, termed membrane scaffold proteins (MSPs), which were capable of self-assembly into discoidal phospholipid bilayers or nanodiscs [104,107]. Right away, nanodiscs displayed distinct advantages over the "old generation" model membranes such as liposomes and detergent-stabilized micelles [105]. First of all, there is a vast variety of nanodisc sizes (from 4 to 12 nm) since MSP can be truncated to a variety of lengths – this maximizes the pool of MPs

(large or small) available for study [108]. Second, nanodisc particle size distribution is quite monodisperse (nanodisc size within single preparation is very similar) and consistent (nanodisc size are the same between different preparations) as the protein belt set boundaries for the dimensions of the bilayer [104,107]. Third, the protein belt also assists in long-term stability of a nanodisc – an empty nanodisc can be stable for up to 2 years at -80°C. Fourth, the lipid content of a nanodisc can come from various sources – synthetic or natural lipids [109]. The most popular synthetic lipids for nanodisc assembly are phosphatidylcholines (PC-lipids) like DMPC (14:0), DPPC (16:0) and POPC (16:0-18:1), as well as mixtures of PCs with charged phospholipids such as phosphatidylserines (PSs), phosphatidylglycerols (PGs), phosphatidylethanolamines (PEs), and phosphatidylinositols (PIPs) [109]. Cholesterol has also been reported to be included into the nanodisc lipid bilayer for research on MPs interaction and fusion with membranes [110,111]. Fifth, nanodisc stability is independent of the critical micelle concentration and does not disassemble upon dilution. On the contrary, Hu and colleagues have found that dilution of nanodiscs induce disk coalescence meaning two or more nanodiscs fuse into one bigger disc [112]. This is not ideal if the monomeric state of an MP is researched, but the bigger disc still helps all MPs to stay soluble and prevent their aggregation. Sixth, a few research papers show evidence that nanodiscs better reflect the complex phase transition behavior of biological membranes than conventional model membranes [113,114]. Last but not least, MSP purification, as well as, nanodisc assembly is a relatively easy and straightforward procedure.

The nanodisc assembly protocol will be discussed in more detail in sections 2.2 and 2.5, however the basic outline of two possible routes for MP extraction into nanodiscs are shown in Figure 8 [115]. Here, route 1 is the standard method for self-assembly of an MP into a nanodisc,

where, first, the biological membrane gets solubilized by detergent and MPs are purified (Figure 8) [115]. Then, the target MP (green) is mixed with the MSP (violet) and lipids at the correct stoichiometry (Figure 8) [115]. Right after, detergent is removed by hydrophobic beads and nanodiscs are assembled with the MP inside, ready for future analysis (Figure 8) [115]. Route 2 is an alternative way for MP extraction, where the membrane tissue gets solubilized by excess lipid and scaffold protein, followed by rapid detergent removal (Figure 8) [115]. This results in placement of the target MP (green), together with other MPs (gray) from the membrane into the nanodiscs (Figure 8) [115]. Nanodiscs with target MPs (green) are purified from nanodiscs with unwanted MPs (grey) often by means of affinity chromatography (Figure 8) [115].

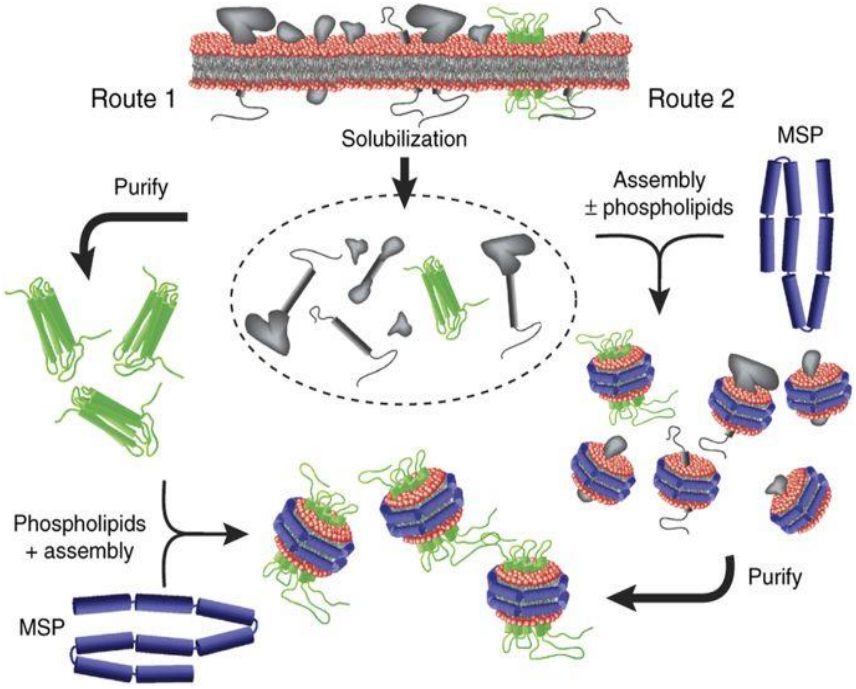

Figure 8. A diagram depicting the process of membrane protein extraction by nanodiscs. Route 1 (left side) is a standard protocol where membrane tissue is solubilized and target MP (green) is purified. Later, this MP is mixed with correct stoichiometry of lipid and MSP (violet) inducing nanodisc assembly around the MP though detergent removal. Alternative route 2 (right side) starts with mixing up biological membrane with excess lipid and scaffold protein which stimulates membrane solubilization. Right after, detergent is removed from solution facilitating nanodisc

formation around all MPs (target or not). Nanodiscs with target MPs are purified from nanodiscs with unwanted MPs. Adapted from Denisov and Sligar [115].

Over the last 10 years, nanodiscs became a very popular membrane mimetic for different biophysical analytical techniques – fluorescence spectroscopy, NMR, surface plasmon resonance (SPR), electron microscopy, X-ray crystallography and, of course, MS [106]. It is no wonder that nanodisc technology quickly found a great application in HDX-MS. However, the general HDX-MS bottom-up workflow shown in Figure 4 was slightly modified – right after the quenching step the nanodisc is disassembled by addition of cholate followed by protein digestion and adsorption of lipid-detergent mix onto ZrO_2 resin [116,117]. One of the examples of where nanodisc HDX-MS technology has proved to be very useful was the study conducted by Parker and colleagues on conformational dynamics of gamma (γ)-glutamyl carboxylase (GGCX) during binding to high-affinity consensus propeptide (pCon) belonging to the Vitamin K Dependent (VKD) class of proteins [118]. The previously used sample preparation methods for GGCX had failed due to aggregation, oligomerization, and precipitation, but nanodisc technology have resolved these issues and have helped to obtained interesting HDX results [118]. The binding event of nanodisc-bound GGCX to pCon has shown multiple decreases in deuterium uptake throughout many regions of GGCX , as well as, regions known to bind pCon [118]. The HDX profile proved the ligand binding event and indicated a more compact structure (less conformationally dynamic) for GGCX when in complex with pCon [118]. This study has shown how nanodiscs were able to provide a stable, native-like environment for MP conformational studies using MS demonstrating again the advantages of “new generation” membrane mimetics.

In addition to nanodiscs, another representative of “new generation” artificial membrane systems are SMALPs. SMALPs exhibit the same discoidal shape as nanodiscs (Figure 7), but the

protein belt is replaced by styrene maleic acid co-polymer (SMA) [119]. There are few advantages of SMALPs over nanodiscs – one of which is that no detergents are used in solubilization of the biological membrane, as SMA inserts into the membrane itself and forms small, soluble nanoparticles containing proteins and lipid bilayer [120]. Also, no synthetic lipids are needed, as SMALPs cut off patches of the biological membrane preserving the complexity of the mosaic bilayer and achieving an even greater "nature-like" environment for MP studies [120]. In this research, however, only nanodiscs were used.

To conclude, "new generation" lipid mimetics more closely resemble the complex mosaic bilayer of biological membranes than the "old generation" allowing for a smoother transition of MPs from their native environment without any functional perturbations.

1.3. Intrinsically Disordered Proteins in Human Diseases

1.3.1. Overview

The structure - function paradigm which implies that a protein with a unique function is defined by its 3D structure has been a strong belief for over a century in the field of biochemistry [121]. Nonetheless, intense research of the human proteome and biology of many human disorders in the last 20 years have clearly shown that the lack of stable tertiary and/or secondary structure does not prevent proteins from being biologically active [70,72,75,121–123]. More notably, IDPs and intrinsically disordered protein regions (IDPRs) are quite abundant in nature and many crucial cellular functions such as signalling, regulation, and transportation processes would not be possible without them [121,124–126]. The functional advantage of IDPs and IDPRs from functional folded proteins is in their structural plasticity and conformational adaptability [121]. Their ability to

rapidly change conformations in response to different environments permits them to fold differently and interact with different binding partners allowing for a wide set of functions for different cellular contexts [70,72,75,121–123]. Since IDPs/IDPRs are usually fluctuating between two major protein forms, functional - folded and functional - intrinsically disordered, misfolding (the failure of a peptide/protein to adopt its functional conformational state) can lead to a broad range of human diseases known as protein conformation or protein-misfolding diseases [121,124]. Certain forms of cancer, Parkinson's disease (PD), dementia, Alzheimer's disease (AD), Down's syndrome, multiple system atrophy (MSA), prion and cardiovascular disease, as well as, Type II diabetes are the most common protein-misfolding diseases caused by various IDPs/IDPRs conformational misfoldings [121,124]. The hallmarks of protein-misfolding diseases are usually aggregation and/or fibril formation, loss of normal function by a protein and gain of a toxic one. For example, the partially folded state of amyloid β-protein (Aβ) promotes protein fibrillation generating the cascade of neuropathogenetic events that results in AD [127]. Another example is loss of function of a very important IDP in cancer prevention, p53, where the interaction with Mdm2/Hdm2 averts it from binding to various transcription factors, and begins the process of p53 degradation in the nucleus and cytoplasm [124,128]. When p53 function is lost and no signal transduction occurs, a cell often undergoes cancerous transformation [124,128]. The high abundance of intrinsic disorder in proteins involved in various diseases gives the wrong impression of IDPs/IDPRs being very unstable and unpredictable proteins incapable of proper folding mechanisms to carry their functions. Actually, functions of IDPs/IDPRs are tightly controlled by various cellular processes like induced folding upon interaction with the corresponding binding partners, alternative splicing (AS), and various PTMs [121,124–126]. When the proper line of control is

failing and/or the cell environment undergoes perturbations, IDPs/IDPRs are structurally "confused" and the capability of recognizing proper binding partners is decreased, forcing them to stay in partially-folded conformations (misfolded) longer and from non-functional and deadly aggregates [121]. Therefore, IDPs/IDPRs are very important and reliable proteins in many biological processes that pose no harm to the healthy state of a cell, unless poorly controlled or environmental conditions have been changed.

The ultimate goal is to understand what causes the loss of IDP/IDPR regulation - the root cause of misfolding, as well as, to validate the most toxic "misfoldants" in order to create specific drugs against them. Fortunately, IDP/IDPR studies are getting more and more attention from the scientific community resulting in the fast development of techniques that will help us know more about this class of proteins and their roles in human diseases.

1.3.2. Parkinson's Disease (PD)

One of the largest groups of misfolding diseases is neurodegenerative disorders which are defined by the loss of neurons within the brain and/or spinal cord [124,129]. The two most common neurodegenerative disorders are Alzheimer's and Parkinson's diseases [129]. The latter one is a motor-impairment disorder with a prevalence close to 2-4% after the age of 60 [130,131]. The main symptoms of PD (can occur separately or together) are tremor at rest, rigidity, akinesia or bradykinesia, and postural/gait instability [130,132]. Sometimes patients may develop depression and non-motor symptoms like anxiety, fatigue and sleep disturbance [133]. This disorder can be either genetically inherited as an autosomal dominant/autosomal recessive trait or gained over

time by means of mutated genes encoding α-synuclein (αSN), parkin and ubiquitin carboxy-terminal hydrolase L1, and/or any perturbations in αSN's concentration or its conformational dynamics in the cell [125,130,134]. The involvement of αSN, an IDP, has a major influence on the development of PD and will be discussed in detail in section 1.3.3.

PD's main pathological hallmarks are the formation of substantial protein aggregates like Lewy bodies (LB) and Lewy neurites (LN), and massive death of dopaminergic neurons in pars compacta of the *substantia nigra* (*substantia nigra* is marked by a red circle in Figure 9) [130,134,135]. The consequence of dopaminergic neurons' death causes major implications to basal ganglia striatonigral direct pathway which is employed for initiation of movement (Figure 9) [136,137].

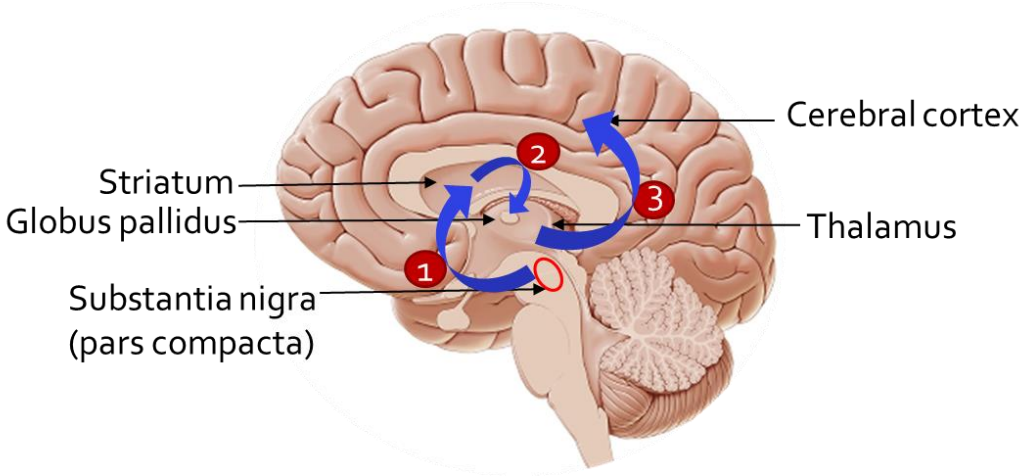

Figure 9. A cartoon representation of the simplified basal ganglia striatonigral direct pathway in a human brain (midsagittal plane cut). (1) The pathway starts with dopaminergic neurons sending dopamine to the striatum. (2) The striatum gets activated and releases GABA to globus pallidus in the basal ganglia. (3) Activated thalamocortical pathway (in thalamus) transmits signal to cortex for initiation of movement [136,137].

In a healthy brain, pars compacta is formed by dopaminergic neurons which send excitatory input to the striatum (Figure 9) [136,137] . The striatum is a connector between *substantia nigra* and the rest of the basal ganglia nuclei (Figure 9) [136]. It receives dopamine, gets activated, and releases gamma-aminobutyric acid (GABA) neurotransmitters into the globus pallidus (Figure 9)

[136,137]. As a result, the thalamocortical pathways (in the thalamus) get activated and transmits motor neuron signals to the cerebral cortex to allow the initiation of movement (Figure 9) [136,137]. In a Parkinson's brain, dopaminergic neurons in pars compacta die and there is less and less dopamine transmission to the striatum which causes motor impairment (Figure 9) [136,137]. Note that this is a very simplistic explanation of basal ganglia circuit only shown here for understanding the overall significance of dopaminergic neurons in healthy motor functions.

Despite great strides made in understanding PD in recent years, diagnostics and treatment of this disorder remains very challenging [132]. With the recognition of several premotor features and potential biomarkers, Parkinson's diagnosis is still primarily based on clinical motor findings which is already in a progressive state of the disease [132]. The most effective treatment is carbidopa-levodopa combination therapy which does not provide a cure but only acts to mask the symptoms, and most patients develop dyskinesia after 5 to 10 years of this treatment [132]. It is important to continue research on the causes and roots of Parkinson's disease, as well as, the possible ways of treating this incurable neurodegenerative disorder.

1.3.3. α-Synuclein and Its Role in PD

Substantial evidence links αSN, a small highly conserved presynaptic protein with unknown function, to both familial and sporadic PD [125,138–146]. αSN in not only the major component of LB/LN, but mutations in the *SNCA* gene encoding for αSN can cause an inherited form of PD, as well as, overexpression of normal (non-mutated) αSN can increase the risk of developing this disorder in sporadic, or non-familial, cases [125,135,138–146]. Being a typical IDP, αSN is capable of

adopting a number of different conformational states depending on cellular conditions and presence of cofactors – it has over 50 ligands where 30 of them are proteins [147–149]. The role of this protein in neurons is vaguely known but recent studies suggest that αSN is very important in cell signalling processes and works as a molecular chaperone for the SNARE complex which plays a key role in compartmentalization, storage, and recycling of neurotransmitters [139,143,147–149]. This protein is abundantly expressed in the nervous system, comprising 1% of total cytosolic protein suggesting an importance in day-to-day functions of neurons, presumably as a modulator of synaptic transmission [125,140].

Unfortunately, as many other IDPs, misfolding of αSN into aggregation-prone intermediates, gain of toxic function and toxic loss of function cause neurotoxicity in dopaminergic neurons and consequent pathogenic effects leading to PD development [146]. There are many ways in which αSN's misfolding and toxic function can affect neurons. It can behave as a prion by being exported from a cell to start the aggregation process in other cells [150]. It can polymerize in protofibrils that form elliptical or circular amyloid pores which are capable of puncturing cell membranes, resulting in the release of cellular contents and cell death [151,152]. Most relevant to this research, is αSN's role in vesicle storage and transportation of dopamine and how misfolding of this IDP results in oxidative stress leading to neuronal cell death [130,153,154]. In dopaminergic neurons of *substantia nigra pars compacta* dopamine is the main neurotransmitter, and, as soon as, dopamine is synthesized it gets packed into small membrane vesicles either for storage or exocytosis (Figure 10) [125,130,146,153,154]. The formation of these synaptic vesicles from early endosomes is regulated by αSN through interaction with phospholipase D2 (Figure 10) [130]. For

proper vesicle construction and transportation, the formation of secondary α-helical structure by αSN on the surface of the lipid bilayer is crucial (Figure 10) [125,138,146,153,154].

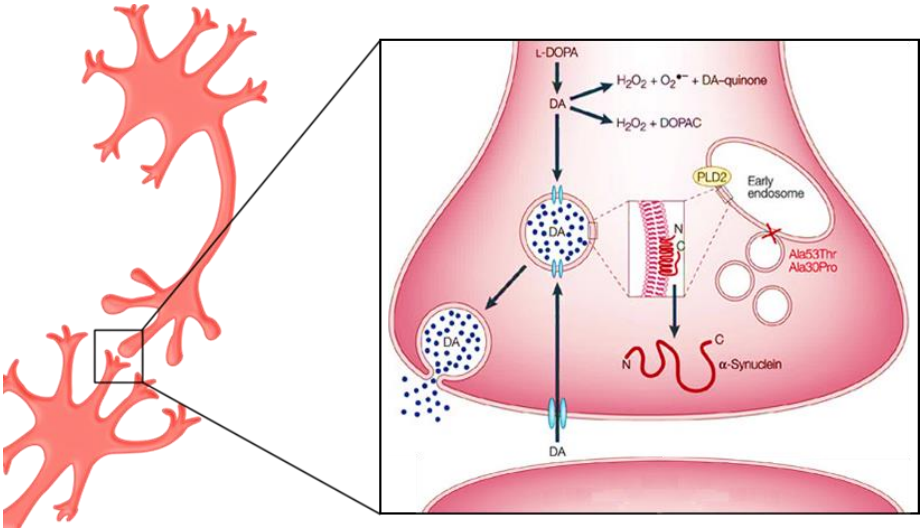

Figure 10. Proposed mechanism of dopamine storage and transportation in presynaptic dopaminergic neurons. Newly synthesized dopamine is packed into small membrane vesicles with the help of α-helically folded αSN and its interaction with phospholipase D2 (PLD2) [155]. Dopamine is then released into the synaptic cleft also with the help of αSN. If αSN is misfolded, less or no vesicle formation occurs leading to self-prone oxidation of dopamine in the cytoplasm. Free radical and oxidative species like H_2O_2, $O_2^{\bullet-}$, and dopamine–quinone by-products (DOPAC) cause oxidative stress and subsequent cell death. Adapted from Lotharius *et al* [138].

Any perturbation of αSN folding will expose hydrophobic regions that are prone to stack into hydrophobic β-sheets, which later lead to the formation of fibrils and Lewy bodies [125,130,146,153,154]. Aggregated αSN can no longer assist in vesicle formation and transportation which results in accumulation of dopamine in the cytoplasm [125,130,146,153,154]. Dopamine in the cytoplasm is predisposed to auto-oxidation creating toxic hydrogen peroxide (H_2O_2), superoxide radicals ($O_2^{\bullet-}$), and dopamine–quinone by-products or 3,4-dihydroxyphenylacetic acid (DOPAC) (Figure 10) [138]. Oxidative stress caused by these radicals and by-products trigger neuronal death [138]. Many models were proposed on the mechanism of αSN's misfolding, which will be discussed later in section 1.3.3.2, but no particular conformational intermediate has yet to be analyzed. Even

though improper folding of αSN is a primary biomarker of PD, little is known about this IDP and the research that started almost 20 years ago continues.

1.3.3.1. Structural properties of αSN

αSN is a relatively small protein composed of 140 amino acids. Its amino acid sequence can be divided into three distinct regions. First is the N-terminus amphipathic region (residues 1 to 60) which contains four 11-amino acid imperfect repeats with conserved motif KTKEGV (Figure 11) [125,146]. This region has a high propensity of forming amphipathic helices, especially in the presence of lipid membranes. Second is a hydrophobic region (residues 61-95) or so-called non-amyloid-beta component (NAC) (Figure 11) [125,146]. The NAC region is highly involved in αSN's aggregation when acquiring beta-sheet structure [125,146,156]. Third is the C-terminal acidic tail (residues 96-140) which is enriched in negatively charged and proline amino acids helping this region to remain unfolded (Figure 11) [125,146,156].

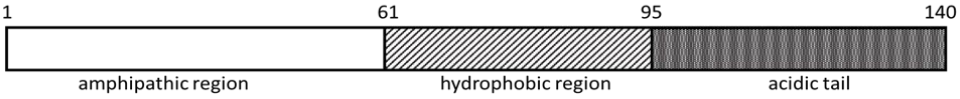

Figure 11. Three distinct regions of αSN's amino acid sequence. The N-terminal region consisting of the first 60 residues is amphipathic and accounts for binding phospholipids, the hydrophobic region between amino acids 61 and 95 is also called the non-amyloid-beta component (NAC), and the C-terminal region (residues 96 to 140) is negatively charged and usually remains unstructured.

In the native form, the NAC domain appears to be partially protected by the long-range interactions (hydrophobic and electrostatic contacts) between the N- and C-terminus, as well as contacts between the C-terminus and NAC [156,157]. These interactions provide a substantial degree of compactness to αSN preventing hydrophobic regions of NAC to be exposed for aggregation

[156,157]. Of course, mutations in αSN, changes in environmental conditions, and PTMs may disrupt this native compactness inducing misfolding and aggregation [156].

αSN falls into a specialized class of IDPs – natively unfolded proteins, as this protein is extremely flexible, relatively noncompact, and its structure is shown to be devoid of significant amounts of secondary order under physiological conditions [125,158]. For its ability to adopt a series of different conformations depending on the environment (temperature, salt, pH etc.), it was called protein-chameleon [159]. Figure 12 represents the series of different conformations that αSN is capable to adopt [159].

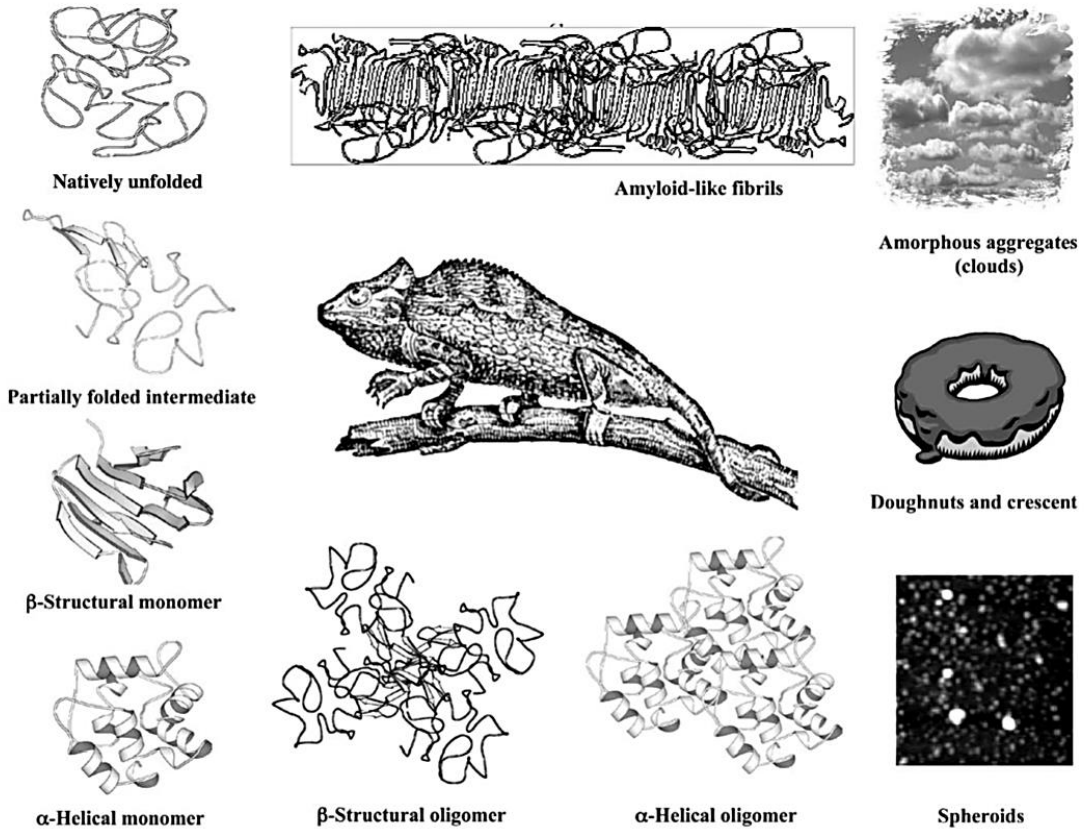

Figure 12. Series of different conformations that αSN, protein-chameleon, is able to adopt in a template-dependent manner. αSN's phenomenal plasticity in response to different environments give rise to many conformational states of this small IDP: (from top left clockwise) natively unfolded monomer, partially folded intermediate, β-structured monomer, α-helical monomer, β-structured oligomer, α-helical oligomer, spheroids, doughnuts and crescents, amorphous aggregates, and amyloid-like fibrils. Adapted from Uversky, 2003 [159].

1.3.3.2. αSN's Conformational Behaviour in The Presence of Lipid Membranes

The membrane-assisted folding of αSN is not only important for the formation of presynaptic membrane vesicles, but also for prevention of its aggregation into LBs [78]. In the presence of a lipid bilayer, αSN acquires its α-helical structure in two main steps: step 1 – the first 20 amino acids on the N-terminus insert themselves as a helix into the phospholipid bilayer, step 2 – the rest of the amphipathic region of αSN and NAC region undergoes a coil/helix transition [78]. While the first two regions of αSN bind lipids through the four 11-amino acid imperfect repeats with a conserved motif KTKEGV, the C-terminal tail remains unstructured and is thought to be a protein-protein interaction motif [125]. Figure 13 represents an axial view of the first 102 amino acids of αSN that form a helix upon interaction with the membrane. αSN resides on the lipid bilayer in a way that hydrophobic residues like Gly, Ala, Val, Leu, Ile, Phe, and Met are embedded into the hydrophobic region of the bilayer, positively charged Lys and His are on the border of the hydrophobic and polar environments and stabilize the helix through electrostatic interactions, and the remaining polar amino acids are on the outside of the lipid bilayer (Figure 13) [160].

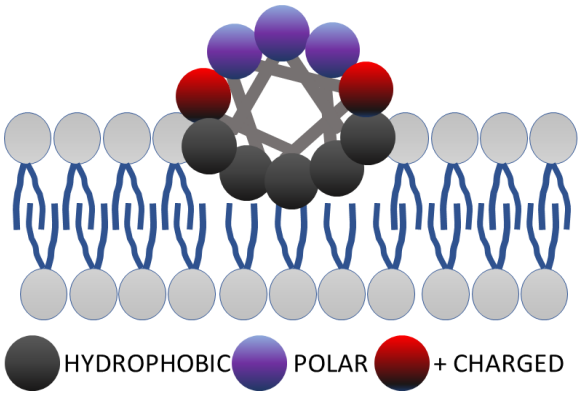

Figure 13. An axial view of the first 102 αSN residues when bound to a phospholipid bilayer. Hydrophobic residues of αSN are embedded into the hydrophobic part of a bilayer, charged amino acids stabilize the helix just outside of lipid bilayer via electrostatic interactions, and polar residues do not interact with lipids at all. Adapted from Auluck et al.[160]

Over the years, some models have been proposed trying to explain the structural behaviour of αSN when interacting with synaptic vesicles. Some of the principal models were made by Igor Dikiy and David Eliezer [141]. From CD and NMR studies, this IDP in the presence of SDS micelles exhibited a helical structure made up of two curved antiparallel helices connected by an extended linker of residues 38 to 44 – this broken-helix state is visualized in Figure 14 [141,161–163]. However, using bigger membrane mimetics like bicelles showed that the lipid-binding domain of this protein was found to adopt a single extended helix (also shown in Figure 14) suggesting a great structural dependence on the size of the membrane system [141,164,165] . Based on these two states and many literature references, the model depicted in Figure 14 was proposed.

In the cell, αSN is in equilibrium between two sates – intrinsically disordered (free protein) and membrane bound (helix state) (Figure 14) [141]. αSN in an intrinsically disordered state can obtain many conformations, more or less extended, as any other IDP [141]. However, when αSN folds onto the vesicle's membrane it obtains an extended-helix, which can then interconvert into the broken-helix state upon approach of the synaptic vesicle to the plasma membrane (Figure 14) [141]. Therefore, the broken-helix state works as a sensor for docked vesicles playing an active role in vesicle fusion either by regulating the activities of other proteins or by membrane remolding required for the fusion process [141]. All of these three conformational states – broken-helix, extended-helix and free protein do not pose any pathological behaviour and are healthy for cells [141]. The conformations that are dangerous and more prone to aggregation are folding intermediates as αSN transitions from one state to another (Figure 14) [141]. In these intermediate states, the N-terminal region remains bound and helical, while the C-terminal region of the lipid-binding domain is unstructured. This opens up the NAC and C-terminal regions for intermolecular

interactions facilitating formation of the beta-sheet rich aggregates – hallmarks of PD (Figure 14) [141]. Dikiy and Eliezer suggest that all aspects of this model must undergo extensive testing before it can be considered to reflect the actual behavior of αSN *in vivo*, but the model is very consistent with many existing observations regarding the properties and potential functions of aSN [141].

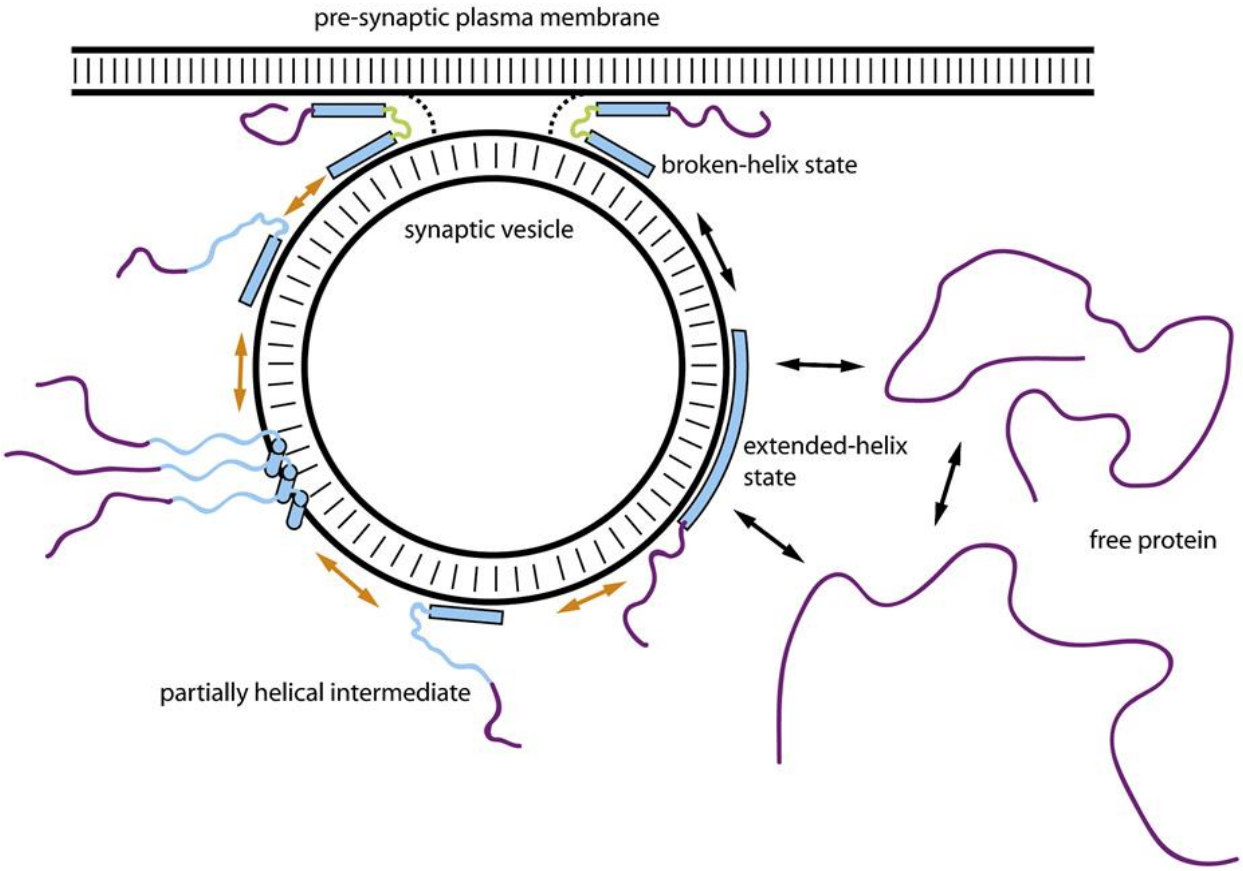

Figure 14. Model for the correlation of different conformational states of αSN when interacting with synaptic membrane vesicles in dopaminergic neurons. Poorly structured protein regions are depicted as solid lines, while helical regions are filled cylinders. Membrane bilayers are indicated as double black lines with dashes. The intrinsically disordered states of αSN are in equilibrium with the vesicle-bound extended-helix state. The latter can convert to the broken-helix state upon approach to the pre-synaptic plasma membrane. Transitions that are a part of a healthy state are indicated by black double arrows, and those that are part of pathological behavior are indicated by orange double arrows. Adapted from Dikiy and Eliezer [141].

1.4 Research Objectives

To better understand Parkinson's disease, the conformational dynamics of αSN's folding and misfolding pathways in the presence or absence of phospholipid membrane must be accurately determined. Structural analysis of αSN using high-resolution biophysical techniques such as X-ray crystallography and NMR possess a lot of challenges and usually are not very informative about the native state of IDPs.

This project covers thorough studies of αSN's structural and conformational dynamics in the presence of a phospholipid bilayer nanodisc using TRESI-HDX-MS. This powerful technique has the capabilities to probe the dynamics of non- to weakly structured regions of the protein on the millisecond to seconds time scale which will help to elucidate key transition intermediates in the folding/misfolding pathway of αSN during the interaction with lipid bilayer. Nanodisc technology will allow for "nature-like" environment during αSN - lipid interaction and, therefore, give more insights in possible αSN's *in vivo* behavior.

We are certain that accurate determination and understanding of αSN's structural dynamics in the presence of nanodisc phospholipid bilayer is a key step in designing a drug that can stabilize the native folded state of αSN and reduce its accumulation in the neuron's cytosol.

Chapter 2: Experimental Methods

2.1. Chemicals and Supplies

The chemicals used in this project were purchased from Sigma-Aldrich, Thermo-Fisher Scientific, BioBasic, and Avanti Lipids unless otherwise specified and were of ACS grade or higher. Ultrapure water was generated in-house by a Millipore Milli-Q Advantage A10 system. The *E.coli* BL21-CodonPlus(DE3)-RIPL competent cells were purchased from Agilent Technologies. Plasmids pET28a-MSP1D1, pET28a-MSP1D1ΔH5, and pET28a-MSP1D1ΔH4H5 were obtained through the collaboration with Audette Lab at York University. *E.coli* BL21 (DE3) containing SNCA in pet23a was kindly provided by Dr. Anurag Tandon's lab at the Tanz Centre for Research in Neurodegenerative Diseases. Ni Sepharose 6 Fast Flow and Q-Sepharose Fast-Flow resin were bought from GE Healthcare. Bio-Beads SM-2 were purchased from Bio-Rad Laboratories. Spectra/Por dialysis membrane RC tubing with 6-8 MWCO was obtained from Spectrum Labs. 1D ^{31}P NMR was performed on a Bruker DRX 600 spectrometer with the XWIN-NMR software package. Size exclusion liquid chromatography (SEC) was carried out on the AKTA Purifier 10 (GE Helthcare) using a Tosoh Bioscience TSKgel column BioAssist G3SWXL (30cm x 7.8 mm ID, 5um) under the control of Unicorn 5.31 software package. The microfluidic channel design was generated using CorelDraw X3 (Corel, Ottawa, ON) and imprinted on VersaLaser^{TM} engraver (Universal Laser, Scottsdale, AZ) Mass spectra were acquired on Synapt G1 and G2S high definition mass spectrometers from Waters under the control of MassLynx V 4.1 software package.

2.2. Expression and Protein Purification

2.2.1. *E.coli* DH5α containing Membrane Scaffold Protein (MSP) Variants

2.2.1.1 Transformation into E.coli BL21, Cell Growth and Expression of MSPs

E. coli (DE3) cells containing MSP1D1, MSP1D1 ΔH5, or MSP1D1 ΔH4H5 in pET28a were separately cultured overnight in 20 mL of Luria-Bertani (LB) medium containing 20 µM kanamycin (Kan) (50 mg /ml stock) and 200 µM of 1M glucose by shaking at 200 rpm at 37˚C. Cells were harvested for plasmid miniprep using Thermo Scientific GeneJET Plasmid Miniprep Kit. Transformation of the obtained plasmids was performed by mixing 200 ng of each plasmid with 100 µL of ice-thawed *E.coli* BL21-CodonPlus(DE3)-RIPL competent cells and incubation of this mixture for 25 min on ice. Consequent heat shock at 42°C was applied for 90 sec, followed by incubation on ice for 5 minutes. Then 900 µL of LB broth was added to each mixture and incubation for 1 hour at 37°C and 125 rpm took place. 100 µL of each plasmid mixture was streaked on Kan LB plates. Plates were incubated at 37°C overnight. One cell colony was picked from each plate and introduced into 20 mL of LB with 20 µM Kan (50 mg/ml stock) and 200 µM of 1M glucose – these mixtures were incubated overnight at 37°C and 200 rpm. Glycerol stocks were made by mixing 500 µL of the overnight cultures with 500 µL 50% glycerol and stored at -80°C. These transformed *E. coli* BL21-CodonPlus (DE3) cells containing pET28a-MSP1D1, pET28a-MSP1D1ΔH5, and pET28a-MSP1D1ΔH4H5 plasmids were cultured overnight in 50 mL of LB containing 50 µM Kan (50 mg/ml stock) and 500 µM of 1M glucose overnight at 37°C and 200 rpm. The overnight cultures were transferred into 500 mL LB-kanamycin medium (same concentrations as overnight medium) and grown to mid-log phase (OD_{600} 0.6-0.8). The translation of these proteins was induced by adding 1mM final concentration of isopropyl β-D-1-

thiogalactopyranoside (IPTG). After three hours of induction, the cells were harvested by centrifugation at 10,000 x g for 30 minutes at 4˚C. Cell pellets that were not used right away were stored at -20˚C for future use.

2.2.1.2. Ni^{2+} Affinity Purification of MSPs

Cell pellets were resuspended in 40 mL of 20 mM phosphate buffer pH 7.4, followed by adding a final concentration 1mM phenylmethylsulfonyl fluoride (PMSF), a final concentration of 1% Triton X-100, 2 mg of deoxyribonuclease I, and 0.8 mL of protease inhibitor cocktail (0.1M benzamide and 0.05M PMSF in 99% ethanol). Proteins were released from the cells by ultrasonic lysis with a sequence set to 6 minutes (15 seconds off, 15 seconds on) at 30% amplitude. The post-sonication solutions containing MSP1D1, MSP1D1 ΔH5 or MSP1D1 ΔH4H5 proteins were centrifuged at 30,000 × g for 30 min at 4°C. The resultant supernatants were collected and loaded on preequilibrated with Wash buffer 1 (40 mM Tris/HCl, 0.3 M NaCl, 1% Triton X-100, pH 8.0) immobilized Ni^{2+}-affinity gravity chromatography columns. Subsequently, each column was washed with 250 mL of Wash buffer 1, 250 mL of Wash buffer 2 (40 mM Tris/HCl, 0.3 M NaCl, 50 mM Na-cholate, 20 mM imidazole, pH 8.0), and 250 mL of Wash buffer 3 (40 mM Tris/HCl, 0.3 M NaCl, 50 mM imidazole, pH 8.0). Elution of each MSP protein was performed by washing the column with 150 mL of Elution buffer (40 mM Tris/HCl, 0.3 M NaCl, 0.4 M imidazole, pH 7). The first 10 fractions (approximately 5 mL each) of each purification were collected and visualized using sodium dodecyl sulfate polyacrylamide gel electrophoresis (SDS-PAGE). Elutions containing MSP1D1, MSP1D1 ΔH5 or MSP1D1 ΔH4H5 proteins were collected and dialyzed into 20 mM

Tris/HCL, 0.1 M NaCl, 0.5 mM EDTA, pH 7.4. Dialysis experiments were performed by using 12-14 kDa MWCO dialysis tubing membrane.

2.2.1.3 Protein Concentration and Storage

Concentration was verified by NanoDrop 2000 UV-Vis Spectrometer and Bradford Assay. Samples were concentrated using 10 kDa Vivaspin column if needed and stored in 20% glycerol at -80˚C.

2.2.2. *E.coli* BL21 containing *SNCA* in pet23a

2.2.2.1. Cell Growth and Expression of αSN

E. coli BL21 cells containing pET-23a vector encoding *SNCA* were cultured in 50 mL of LB medium containing 50 µM Kan (50 mg/ml stock) and 500 µM of 1M glucose overnight at 37°C and 200 rpm. The overnight culture was transferred into 500 mL LB-kanamycin medium (same concentrations as overnight medium) and left growing overnight at 37°C and 200 rpm until mid-log phase was reached (OD_{600} 0.6-0.8). The translation of the protein was induced by adding 1mM final concentration of IPTG. After three hours of induction, the cells were harvested by centrifugation at 10,000 x g for 30 minutes at 4˚C. Cell pellets that were not used right away were stored at -20˚C for future use.

2.2.2.2. Protein Release by Cell Sonication and Boiling

For protein purification, cell pellets were resuspended in 25 mL of Suspension buffer (Phosphate Buffered Saline pH 7.2 (1xPBS) and 1mM PMSF.) αSN was released from the cells by ultrasonic lysis with a sequence set to 6 minutes (25 seconds off, 25 seconds on) at 18%

amplitude. Sonicated cells were transferred to a heat-resistant tube and boiled in a 100˚C water bath for 15 minutes. The sample was centrifuged at 10,000 x g for 15 minutes and the supernatant was collected. The resulting supernatant was spun again at 35,000 x g for 35 minutes and the final supernatant was collected for dialysis into 50mM Tris, pH 8.3. Protein purification must be performed on the day the last dialysis exchange is completed.

2.2.2.3. Protein Purification by Anion Exchange Chromatography

Purification of αSN was continued by performing anion-exchange chromatography using a Q-Sepharose gravity column. The column was washed with 3 column volumes (CV) of 20% ethanol and 5 CV of 50mM Tris, pH 8.3 before loading dialyzed solution containing αSN. Elution of the protein was obtained by loading a step NaCl gradient – 100 mM, 150 mM, 200 mM, 250 mM, 300 mM and 500mM at 50 mL each. All fractions were collected and visualized using SDS-PAGE. Elutions containing αSN were collected and dialyzed into 20mM Tris-Cl, pH 7.4. All dialysis experiments were performed using 6-8 kDa MWCO dialysis tubing membrane.

2.2.2.4 Protein Concentration and Storage

Concentration was verified using the Bovine Serum Albumin (BSA) assay. Samples were concentrated using a 3kDa Vivaspin column if needed and stored in 20% glycerol at -80˚C.

2.3. Protein Visualization

As previously mentioned in sections 2.2.1.2 and 2.2.2.3, elutions from Ni^{2+}-affinity and anion-exchange gravity columns were collected and run in the 12.5% SDS-PAGE. 12.5% polyacrylamide

gels were made by first preparing separation gel where 6.93 mL ddH_2O, 5.2 mL 40% acrylamide, 4.2 mL 1.5M Tris pH 8.8, 166.5 µL 10% SDS, 166.5 µL 10% ammonium persulfate (APS), 16.5 µL tetramethyl ethylenediamine (TEMED) were mixed and loaded into four gel-casting chambers. After the waiting period of 20 min, stacking gel was made by mixing 3.16mL ddH_2O, 0.5 mL 40% acrylamide, 1.265 mL 1 M Tris pH 6.8, 50 µL 10% SDS, 50µL 10% APS, 5 µL TEMED which was then loaded on top of separation gels. Gel electrophoresis was performed at 220V for 43 min on Bio-Rad PowerPac basic power supply. Running buffer for gel electrophoresis was 1xTris-Glycine (25 mM Tris-Cl, 250 mM glycine, 0.1% SDS). Afterwards, gels were stained for 20 min using 0.1% Coomassie Brilliant Blue R-250, 50% methanol and 10% glacial acetic acid buffer while gently shaking the gel's container. Distaining was done by gently rocking the gel with 40% methanol and 10% glacial acetic acid.

2.4. Protein Desalting and Electrospray Ionization Mass Spectrometry (ESI-MS)

All proteins (αSN, MSP1D1, MSP1D1 ΔH5, and MSP1D1 ΔH4H5) were desalted and dialyzed against 50mM ammonium acetate pH 7.4 by Zeba Spin desalting columns (7K MWCO). The native spectra of αSN, MSP1D1, MSP1D1 ΔH5, and MSP1D1 ΔH4H5 proteins were obtained using a Waters Synapt G2-S Mass Spectrometer set to the positive mode. αSN was diluted to 2.5 µM in 50mM ammonium acetate pH 7.4 and infused into the mass spectrometer at a flow rate of 5 µL/min at 2.4 kV. Sampling cone was set to 50V, source temperature to 60˚C, desolvation temperature to 150˚C, trap collision energy to 4.0, transfer collision energy to 10.0, and trap gas flow to 2.00 mL/min. All MSPs were diluted to 1.5 µM in 50mM ammonium acetate pH 7.4 and infused into the MS at a flow rate of 5 µL/min at 2.0 kV. Sampling cone was set to 70V, source

temperature to 100˚C, desolvation temperature to 150˚C, trap collision energy to 15.0, transfer collision energy to 10.0, and trap gas flow to 2.00 mL/min.

2.5. Nanodisc Assembly

The working lipid stock mixture was prepared by resuspending lyophilized 14:0 PC, also known as DMPC, with HPLC grade water for a final concentration of 50 mM producing the "lipid stock". Equal amounts of lipid stock solution and 100mM Na-cholate (1:1 ratio) were mixed, then heated under ~50° tap water for 2-3 minutes and sonicated in an ultrasonic bath until the solution is clear and no lipid remains on the walls of the tube. This is the "working lipid stock" where the final concentration of Na-cholate is double that of DMPC. The optimum ratios for different sizes of nanodisc were taken from Table 1 which was adopted from Bayburt *et al* [103].

Table 1. Optimum protein-lipid ratios for nanodisc formation for three different phosphatidyl-cholines (PCs) and three different MSPs.[1]

Lipid	Optimum ratios for MSP1	MSP1ΔH5	MSP1ΔH4H5	Incubation temperature
DPPC	**90:1**	**56.3:1**	**22.5:1**	**37 ºC**
DMPC	**80:1**	**50:1**	**20:1**	**25 ºC**
POPC	**65:1**	**40.6:1**	**16.25:1**	**4 ºC**

[1] Adapted from Bayburt *et al*, 2002 [103].

Upon mixing the recommended ratios of DMPC lipids with MSPs, these nanodisc reconstruction mixtures were incubated for 15 minutes at 25˚C, then 1 hour at 4˚C. Next, BioBeads SM-2 in the amount of 0.6 g per 1 mL were added to the reconstruction mixture. These suspensions were then placed on an orbital shaker and incubated for at least 2 hours at 4°C. Formed nanodiscs were then removed from the beads with storage at 4°C for future use and

confirmed using NMR spectroscopy. The nanodiscs were further purified by SEC using 0.1M NH4OAc, pH 7 as elution buffer for future MS use. A different lipid constitution was also tried out – 80% DMPC and 20% 16:0-18:1 PS (POPS). All the steps in the formation of nanodiscs were the same. The general outline of the key steps in formation of nanodiscs is illustrated in Figure 15.

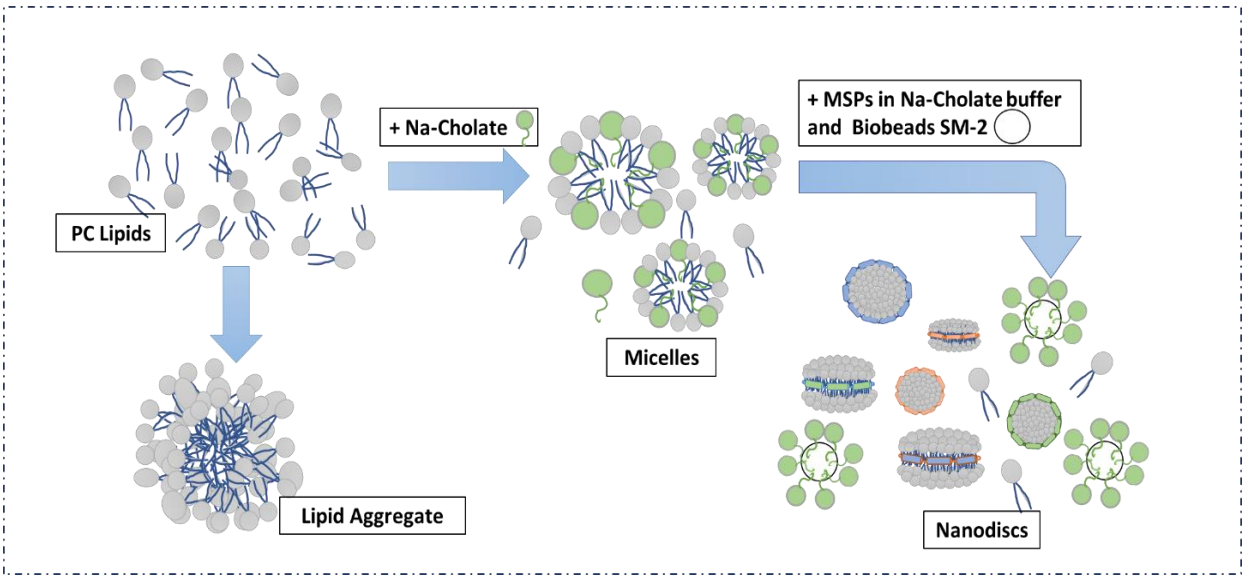

Figure 15. Key steps in the formation of phospholipid nanodiscs. Starting from the top left, phospholipids are resuspended in aqueous solution by sonication and warm water. Then, detergent in the form of sodium cholate is added to the lipids. This stabilizes the lipids to form cholate-lipid micelles. If the lipid-detergent solution is not clear, lipids have precipitated into bulky lipid aggregates. Next, MSPs in cholate buffer and BioBeads SM-2 are added to the micelles. During incubation of this mixture, lipids start to replace the detergent that was bound to the protein, the detergent is adsorbed by the beads, and the nanodisc is formed.

2.6. Verification of Nanodisc Formation by 1D ^{31}P Nuclear Magnetic Resonance (NMR) and Size Exclusion Chromatography (SEC)

Formed nanodiscs were spiked with 10% D_2O and placed in a 5mm broad band NMR probe. 1D ^{31}P NMR experiments were recorded at 298K on a Bruker DRX 600 spectrometer. Each spectrum was recorded in 40,960 scans with a relaxation delay of 0.77 seconds at a frequency of 242.9 MHz and 30˚ pulse angle. Spectra were processed with the XWIN-NMR software package.

Formed nanodiscs were also verified by SEC on the AKTA Purifier 10 (GE Healthcare) using Tosoh Bioscience TSKgel column BioAssist G3SWXL (30cm x 7.8 mm ID, 5µm,) with the separation range of 10 to 500 kDa under the control of Unicorn 5.31 software package. Nanodisc sample in the amount of 500 µL was first introduced in a pre-equilibrated 500 µL injection loop. Second, the column was equilibrated with 0.1 CV of 0.1 M ammonium acetate pH 7, followed by injection of the nanodisc sample into the column. This was followed by 1.5 CV elution at a flow rate of 0.5 mL/min using 0.1 M ammonium acetate pH 7 and collection of samples at 0.5 mL each. The chromatogram was generated in Unicorn 5.31 software package with UV absorption readings at 280 nm and 215 nm.

2.7. Electrospray Ionization Mass Spectrometry (ESI-MS) of 6nm Nanodisc

The native MS spectra of MSP1D1 ΔH5 nanodisc (6 nm nanodisc) was obtained using a Waters Synapt G1 mass spectrometer set to the positive mode. After SEC purification, samples were dialyzed into 0.2 M ammonium acetate pH 7.4 and infused into the mass spectrometer at a flow rate of 15 µL/min and 2.5 kV. Sampling cone was set to 200 V, source temperature to 100˚C, desolvation temperature to 150˚C, trap collision energy to 30, transfer collision energy to 4, and trap gas flow to 2.50 mL/min. Backing pressure was set to 5.32 bar.

2.8. Time-Resolved-Electrospray Ionization Mass Spectrometry (TRESI-MS)

The TRESI-HDX experiment begins with packing the proteolytic reaction chamber (Figure 16) with protease XIII agarose beads which were obtained by functionalizing protease XIII on agarose beads in 10% acetic acid (pH 2.3) overnight at 4˚C. Next, the TRESI apparatus was assembled

(highlighted in light-pink in Figure 16). The notch was cut 4 mm from the sealed end of glass capillary by VersaLaser™ laser engraver. Then, the TRESI apparatus and acetic acid line were connected to the mixing tee (grey circle in Figure 16) and, subsequently, connected to the microfluidic chip. All acid, protein, and deuterium syringes were attached to the corresponding capillary lines and placed on Harvard 11+ infusion syringe pumps (Holliston, MA). The principal of time-resolved HDX is shown in Figure 16 (enlarged pink portion of Figure 16), where protein flowing through the glass capillary exits into the outer metal capillary through a notch. Deuterium flowing in the outer metal capillary mixes with protein at the notch region which allows for millisecond to second deuterium exchange as the HDX reaction will be quenched by acid in the mixing tee. Quenched protein is then digested in the protease/pepsin reaction chamber and resulting peptides enter the mass spectrometer via ESI (Figure 16).

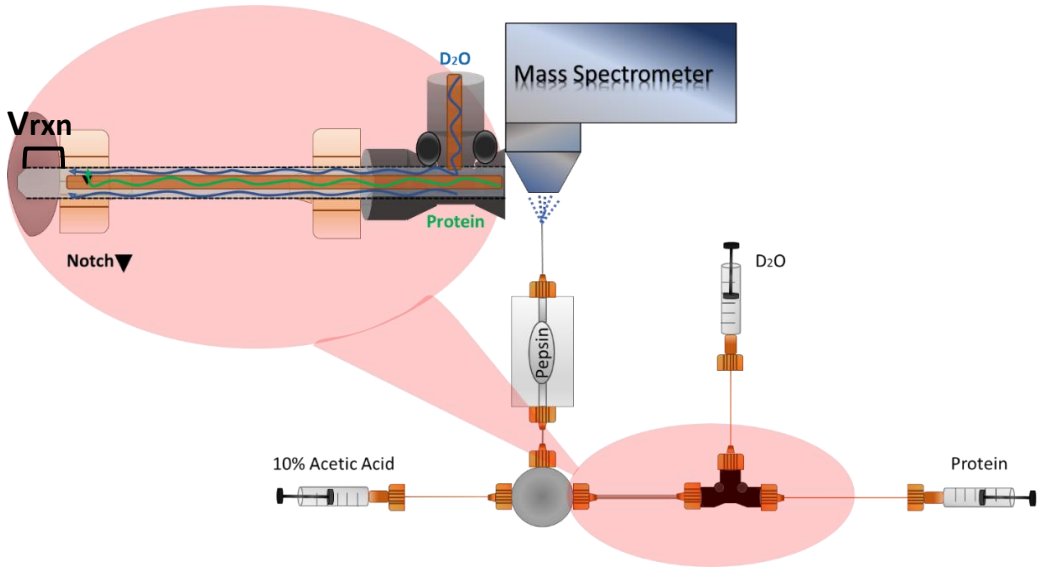

Figure 16. Illustration of the experimental setup for a typical TRESI-HDX experiment. Starting from the pink inset, two syringes filled with D_2O and protein are hooked up to a T-connector by glass capillaries. The third end of the T-connector is attached to a metal capillary (bigger in diameter than the glass one). The protein's glass capillary is threaded trough the metal capillary, D_2O directly flows inside the metal capillary. Protein and D_2O meet and mix at the notch, which can be pulled back for varying volumes of the HDX reaction. This time-resolved mixer is then connected to a mixing tee (grey circle). The acid line is also attached to the tee where quenching of HDX occurs. The mixing tee is connected to the microfluidic chip filled with protease XIII.

2.9. Microfluidic Device Fabrication

The microfluidic chip was made, first, by cutting a blank poly-methyl methacrylate (PMMA) block purchased from Professional Plastics (Fullerton, CA) into two rectangles (5 cm x 2 cm). Then, the pepsin/protease reaction chamber as well as "in" and "out" channels were engraved on one of the PMMA rectangles using a VersaLaser™ engraver (Universal Laser, Scottsdale, AZ). The microfluidic channel design was generated using CorelDraw X3 (Corel, Ottawa, ON). Back to the chip assembly, the engraved block was sandwiched with the blank PMMA and fused together using Weld-On 4 acrylic adhesive. The microfluidic chip was left to dry overnight. Treads for the wing nuts were made for the "in" and "out" channels using a 10/32 NF drill bit on the drill press station. The final product of the microfluidic chip device is shown in Figure 17.

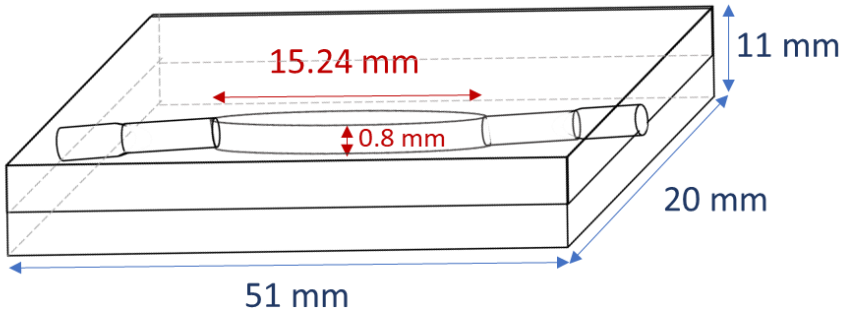

Figure 17. Microfluidic chip designed and produced by the Wilson Lab with its dimensions.

2.10. Hydrogen/Deuterium Exchange of αSN and αSN-DMPC nanodisc (6nm) complex; Equilibrium Studies

TRESI-HDX-MS equilibrium experiments included 6 time-points for two different protein states: αSN alone and αSN in complex with the 6nm DMPC nanodisc. Starting with sample preparation, the complex of αSN with the MSP1D1 ΔH5 DMPC nanodisc (6nm) was formed by mixing them

together at a 1:1 ratio. Both αSN and the MSP1D1 ΔH5 DMPC nanodisc were in their storage buffers prior to mixing (see sections 2.2.1.2 and 2.2.2.3). The mixture was incubated at 37°C for 1 hour at 100rpm. Formed complex was verified and purified from unbound lipids and proteins by SEC using the same LC method and parameters from section 2.6. SEC fractions under UV_{280} chromatographic peaks were also visualized using SDS-PAGE for confirmation of complex formation. SEC also served to desalt and buffer exchange the αSN - DMPC 6nm nanodisc complex into 0.1 M ammonium acetate pH 7. For αSN alone, desalting and buffer exchange into 0.1 M ammonium acetate pH 7 was performed using Zeba Spin desalting columns (7K MWCO). For both protein states, the TRESI-HDX-MS experimental set-up was the same. Flow rates were 5 µL/min for 10 µM αSN alone or 10 µM complex, 5 µL/min for D_2O, and 20 µL/min for 10% acetic acid. Quenched samples were digested by protease XIII, and the resulting peptides were ionized by electrospray into the mass spectrometer. IMS was employed in the TriWave cell of the Synapt G2S to improve spatial resolution of peptides in the digested sample. Six time points (0.12 sec, 0.34 sec, 0.66 sec, 1.32 sec, 2.2 sec and 3.3 sec) were obtained for each protein state. For each time point three technical replicates were acquired. Mass spectra of protease XIII equilibrated with 0.1 M ammonium acetate pH 7, HPLC water and 10% acetic acid was acquired (flow rates were 5 µL/min for buffer, 5 µL/min for water, and 20 µL/min for acid). In addition, a peptide digest acquisition of the 6nm DMPC nanodisc sample was obtained to exclude all the peptides coming from MSP1D1 ΔH5 (same flow rates as protease XIII control). Nanodiscs for this control were buffer exchanged into 0.1 M ammonium acetate pH 7 using SEC (see section 2.6). Both protein states were analyzed on the same day to exclude for possible day-to-day variability.

2.11. Hydrogen/Deuterium Exchange of αSN and αSN-DMPC nanodisc (6nm) complex; Kinetic Studies

TRESI-HDX-MS kinetic experiments also included 6 time-point runs for two different protein states - αSN alone and αSN complexed with the MSP1D1 ΔH5 DMPC nanodisc. Starting with sample preparation, for αSN alone and αSN that will be mixed with nanodiscs, desalting and buffer exchange into 0.1 M ammonium acetate pH 7 using Zeba Spin desalting columns (7K MWCO) was performed. Nanodiscs were desalted and buffer exchanged into 0.1 M ammonium acetate pH 7 using SEC (see section 2.6). For both protein states, the experimental set-up was the same. For αSN alone, 5 µL/min of 10 µM αSN was flowing in the protein line, 5 µL/min D_2O was flowing in the deuterium line, and 20 µL/min of 10% acetic acid in the acid line. For αSN mixing with the nanodisc state, 5 µL/min of 10 µM αSN was flowing in the protein line, 5 µL/min of D_2O mixed with 10 µM 6nm DMPC nanodisc was flowing in the deuterium line, and 20 µL/min of 10% acetic acid in the acid line. Quenched samples were digested by protease XIII and resulting peptides were ionized by electrospray into the mass spectrometer. IMS was employed in the TriWave cell of the Synapt G2S to improve spatial resolution of peptides in the digested sample. Four or six time points (0.12 sec, 0.34 sec, 0.66 sec, 1.32 sec, 2.2 sec and 3.3 sec) were obtained for each protein state. For each time point three technical replicates were acquired. Mass spectra of protease XIII equilibrated with 0.1 M ammonium acetate pH 7, HPLC water and 10% acetic acid was acquired as a control (flow rates were 5 µL/min for buffer, 5 µL/min for water, and 20 µL/min for acid). Both protein states were analyzed on the same day to exclude for possible day-to-day variability.

2.12. Data Acquisition

TRESI-HDX-MS was performed on a Synapt G2S which consists of a StepWave ion guide, quadrupole, TriWave cell containing Trap, IMS and Transfer cells, and a TOF analyzer (Figure 18). For TRESI-HDX-MS experiments the following parameters were used: 2.5 kV capillary voltage, 120°C source temperature, 25.0 sampling cone, 250 °C desolvation temperature, 50 L/hr cone gas flow, 6.0 Trap collision energy (CE), 6.0 Transfer CE and 90 mL/min IMS gas flow. Acquisition range was m/z 400 to 1500. TOF analyzer was in sensitivity mode. Ionization mode was ES+. Optimal positioning of the electrospray tip was achieved using an adjustable stage.

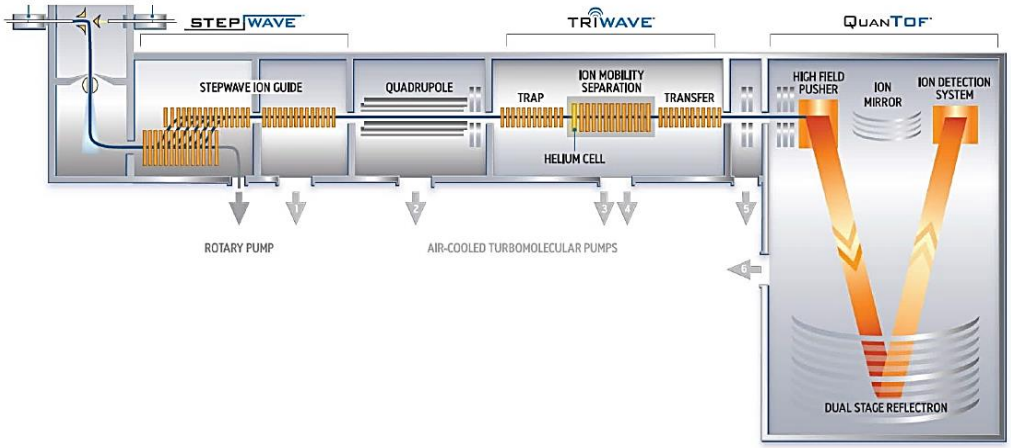

Figure 18. Instrument schematic of a Synapt G2S (Waters, MA). Ions are introduced into the mass spectrometer through an ESI sources and selected through a StepWave ion guide and subsequent quadrupole.

2.13. Data Analysis and Representation

The peptic digest of αSN was analyzed using FindPept tool on the ExPASy Proteomics server [166]. This software assigns resulting masses to possible peptides based on the sequence of the protein. If more than one peptide was matched to the same mass, MSMS was performed for peptide identity. A 1-hour protease XIII digest of αSN was subjected to LC-MSMS on an EASY-

nLC™ nanoflow LC system (Thermo Fisher, MA) coupled with an LTQ Orbitrap Elite mass spectrometer (Thermo Scientific, MA). A 30 min gradient with 0.1% formic acid in water as the LC mobile phase A and 80% acetonitrile as the LC mobile phase B was implemented in this LC-MSMS workflow. Resulting MSMS spectra were analyzed with Proteome Discoverer 1.4 software package . Identified peptides were analyzed for deuterium uptake using Mass Spec Studio 1.0 - a free software developed in Dr. David Schriemer's research group [167]. Deuterium uptake difference and kinetic plots were made using Excel software. Mapping of the deuterium uptake onto crystal structures of α-syn was performed using PyMOL software [168].

Chapter 3: Results and Discussion

3.1. Purification of αSN and MSPs

3.1.1. SDS-PAGE of Samples Taken During Expression and Purification of MSP1D1, MSP1D1 ΔH5, and MSP1D1 ΔH4H5

All MSPs were expressed in *E.coli* BL21-CodonPlus(DE3)-RIPL competent cells for 3 hours at 37°C. The expression trial for MSP1D1 is shown in the first five lanes of Figure 19 (excluding the MWM lane). According to literature the molecular weight of the MSP1D1 protein is 24.6 kDa, the gel band for which should be located very close to the 25 kDa mark [108].

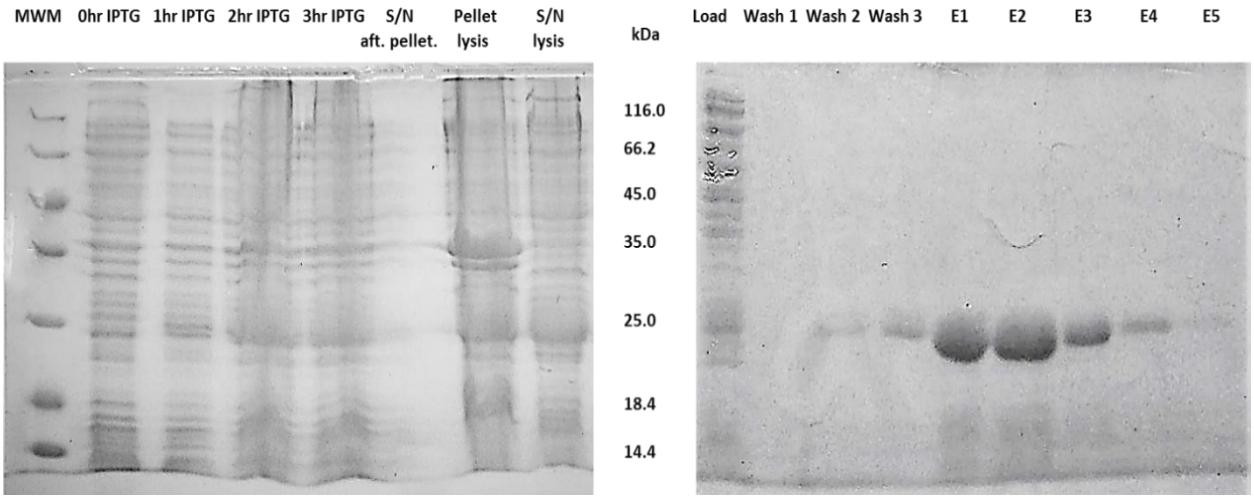

Figure 19. SDS-PAGE of expression and purification of MSP1D1. From left to right: molecular weight marker (ThermoFisher #PI-26616), MSP1D1 expression pellets from 0 to 3 hours at 37˚C, supernatant collected after pelleting the expressed cells, pellet and supernatant collected after lysis, fraction collected after supernatant was loaded on the column, fractions collected from subsequent wash of the beads with Wash buffer 1, 2 and 3, elutions 1 to 5 of MSP1D1 protein with Elution buffer. The thick bands in elution E1 to E4 at 25 kDa mark indicated the presence of purified MSP1D1 protein which has the theoretical mass of 24.6 kDa. These fractions were pooled and later used for 10 nm nanodisc formation.

During the expression there was an increase in thickness of the band corresponding to MSP1D1 at 2nd and 3rd hours of incubation. This result suggested the successful expression of the MSP1D1 protein. To ensure that *E.coli* cells stayed intact during the pelleting step, the sample

of supernatant (S/N aft. pellet. in Figure 19) was run on the gel as well. During the purification process of MSP1D1, pellet (Pellet lysis in Figure 19) and supernatant (S/N lysis lane in Figure 19) after the sonicated debris was spun down were run in order to show that MSP1D1 was successfully released from the cells into a soluble fraction. Both of the lanes corresponding to these samples showed two bands at the 25 kDa mark with a similar thickness, proposing that some of the protein got precipitated along with the cell debris (Figure 19). The precipitation of MSP1D1 can be explained by binding of this MP to the membrane of *E.coli* cells and precipitating along with it. The supernatant containing solubilized MSP1D1 was loaded on a Ni^{2+} affinity gravity column and subsequent washes and elutions are shown in the last nine lanes of Figure 19. "Load" lane represents the flow-through after MSP1D1 was loaded onto the column. This lane contained various bands embodying a range of different sized proteins which did not bind to Ni^{2+} beads and eluted (Figure 19). No significantly thick band was observed at 25 kDa due to successful binding of MSP1D1 to Ni^{2+} beads by its 6xHis tag (Figure 19). Samples from the three washes of the Ni^{2+} column had some MSP1D1 being eluted, especially after "Wash 3" (Figure 19). However, elutions 1 to 4 displayed the thickest bands at the 25 kDa mark, making the protein lost in "Wash 3" and "Load" insignificant. No other visible bands were presented in elutions 1 to 4 which indicated successful purification of MSP1D1 from other proteins (Figure 19).

MSP1D1 ΔH5 was also checked for successful expression and purification. According to literature the molecular weight of the MSP1D1 ΔH5 protein is 22.1 kDa [108]. Samples corresponding to the pellet (Pellet lysis in Figure 20) and supernatant (S/N lysis lane in Figure 20) after the sonicated debris was spun down were run in the first two lanes. No thick band at around 22.1 kDa was observed for the "Pellet lysis" lane suggesting that all of the MSP1D1 ΔH5 protein

is contained in the supernatant (Figure 20). Indeed, a very thick gel band in the "S/N lysis" lane supports this result.

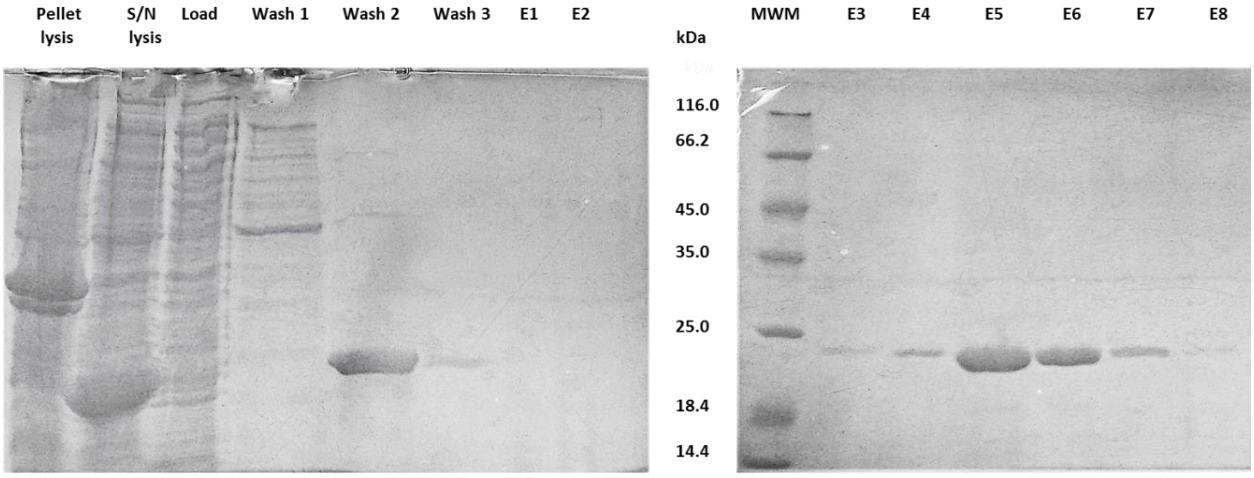

Figure 20. SDS-PAGE showing purification of MSP1D1 ΔH5. From left to right: pellet and supernatant collected after lysis, fraction collected after supernatant was loaded onto the column, fractions collected from subsequent wash of the beads with Wash buffer 1, 2 and 3, elutions 1 to 2 of MSP1D1 ΔH5 protein, molecular weight marker (ThermoFisher #PI-26616), elutions 3 to 8 of MSP1D1 ΔH5 protein with Elution buffer. The thick bands in elution E4 to E7 just below 25 kDa mark indicated the presence of purified MSP1D1 ΔH5 protein which has the theoretical mass of 22.1 kDa. These fractions were pooled and used to form 6 nm nanodisc.

Protein supernatant was loaded on the Ni^{2+} affinity gravity column. "Load" lane showed a range of different proteins suggesting that most did not bind to the Ni^{2+} beads and eluted from the column right away (Figure 20). No significant band for MSP1D1 ΔH5 was spotted suggesting the successful binding event of this protein to the column. Subsequent "Wash 1" displayed a range of proteins, but no substantial bands below 25 kDa (Figure 20). However, the "Wash 2" sample exhibited quite a thick band corresponding to MSP1D1 ΔH5 along with some faint bands above 45 kDa (Figure 20). A relatively small amount of MSP1D1 ΔH5 eluted in "Wash 3", but it could be neglected compared to the thickness of bands in elutions 5 and 6 (Figure 20). E4 to E7 also showed thick bands just below the 25 kDa mark and no other visible bands indicating a successful purification of MSP1D1 ΔH5 (Figure 20).

In the case of MSP1D1 ΔH4H5, the protein expression level was checked at a 3-hour time point after inducing with IPTG and compared with the 0-hour time point – first two gel lanes in Figure 21. According to literature the molecular weight of the MSP1D1 ΔH4H5 protein is 19.2 kDa [108]. The successful expression of MSP1D1 ΔH4H5 was confirmed by a much thicker band at 18.4 kDa at "3hr IPTG" lane than the same band at "0 hr IPTG" (Figure 21). As expected, the "Load" lane in Figure 21 showed a variety of unbound proteins to the column but did not indicate any significant amounts of unbound MSP1D1 ΔH4H5 as no thick band around the 18.4 kDa mark was detected. Only "Wash 1" was performed for the MSP1D1 ΔH4H5 purification and the corresponding gel lane exhibited just two bands above the 18.4 kDa mark meaning no MSP1D1 ΔH4H5 was eluted during this wash (Figure 21). Although elutions 2, 7, 8, and 9 had thick bands corresponding to MSP1D1 ΔH4H5, they also contained a range of fainter bands (Figure 21). While the protein was not purified to the same extent as the other MSPs, it was still used for 4 nm DMPC nanodisc formation (sections 2.5 and 2.6).

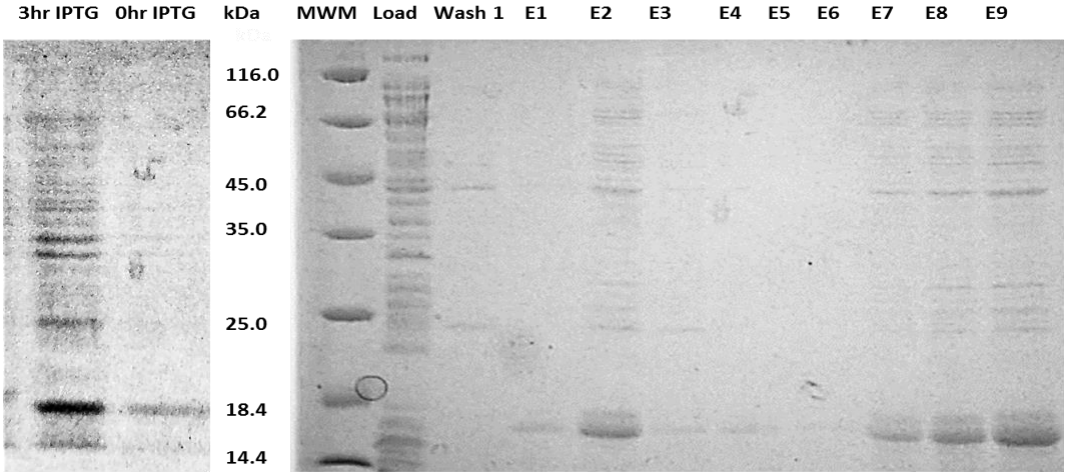

Figure 21. SDS-PAGE of expression and purification of MSP1D1 ΔH4H5. From left to right: MSP1D1 ΔH4H5 expression pellets at 3 and 0 hours at 37˚C, molecular weight marker (ThermoFisher #PI-26616), fraction collected after supernatant was loaded onto the column, fractions collected from elution with Wash buffer 1, elutions 1 to 9 of MSP1D1 ΔH4H5 protein with Elution buffer. The presence of relatively more thicker bands at 18.4 kDa mark in E7 to E9 indicated the presence of purified MSP1D1 ΔH4H5 protein with molecular mass of 19.2 kDa.

3.1.2. SDS-PAGE of Samples Taken During Expression and Purification of αSN

According to literature, the molecular weight of αSN is 14.6 kDa [169]. During the purification process of αSN, samples of supernatant (S/N lane in Figure 22) and pellet (Pellet in Figure 22) after the sonication of cells were run on the gel to confirm αSN's solubilization. There was no band corresponding to αSN in the "Pellet", and a very thick band between 14.4 and 18.4 kDa in the "S/N" – this was an indication of successful lysis and high-yield solubilisation of αSN. The "S/N" was very clean and only low intensity protein bands were observed (Figure 22). This purity can be explained by the boiling step that took place after lysis – most of the other proteins degraded and precipitated in the pellet.

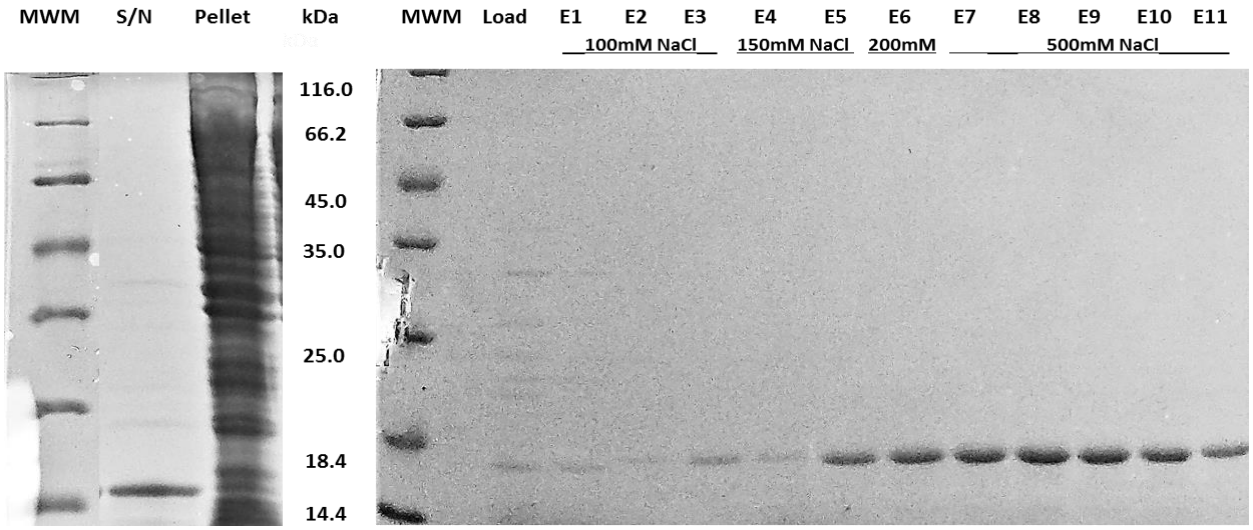

Figure 22. SDS-PAGE of expression and purification of αSN. 20µL of each sample was mixed with 10µL of 4XSDS loading dye and boiled for 5 minutes at 100˚C. 12µL of each mix was loaded onto a 12.5% SDS gel and run at 220V for 40 minutes. From left to right: molecular weight marker (ThermoFisher #PI-26616), supernatant collected after sonication, pellet collected after sonication, molecular weight marker (ThermoFisher #PI-26616), fraction collected after supernatant was loaded onto the column, fractions collected from elutions 1 to 11.

After the supernatant was loaded onto the anion-exchange gravity column, the subsequent fractions were taken – "Load" and E1 to E11 (Figure 22). The "Load" lane showed a range of

different proteins suggesting that most eluted right away, but no significant band for αSN was observed indicating a strong electrostatic interaction of αSN with anion resin (Figure 22). Elutions 1 to 3 were collected using 150 mM NaCl which contained low concentrations of αSN as well as other proteins (Figure 22). Starting from E4 up to E11, the only observable band presented corresponds to αSN (Figure 22). The thickest αSN's bands were obtained using 500 mM NaCl and were collected as the most concentrated samples for further dialysis and TRESI-HDX experiments (Figure 22).

3.2. Determination of Protein Molecular Mass by ESI-MS

3.2.1. Native MS of MSP1D1, MSP1D1 ΔH5, and MSP1D1 ΔH4H5

ESI-MS spectra of intact/undigested MSPs were obtained in order to confirm the protein identity by mass, as well as, check for any impurities or degradation products. Figure 23 displays three native MS spectra for these three proteins along with screenshots of ESIprot Online calculation results. For MSP1D1, two peak distributions are observed: 1) lower m/z range where peaks represent an unfolded protein state, and 2) higher m/z range where peaks represent a folded protein state (Figure 23). Using m/z values of five consecutive peaks corresponding to the unfolded state, the exact mass of MSP1D1 was calculated using ESIprot software (Figure 23). The calculated mass was 24,781.6208 ± 0.77801 Da which was quite consistent with the theoretical mass of MSP1D1 based on its sequence (24,661.9 Da). The discrepancy between these two masses might arise from the fact that theoretical mass is calculated based on monoisotopic peak value, but experimental mass is based on a peak's centroid.

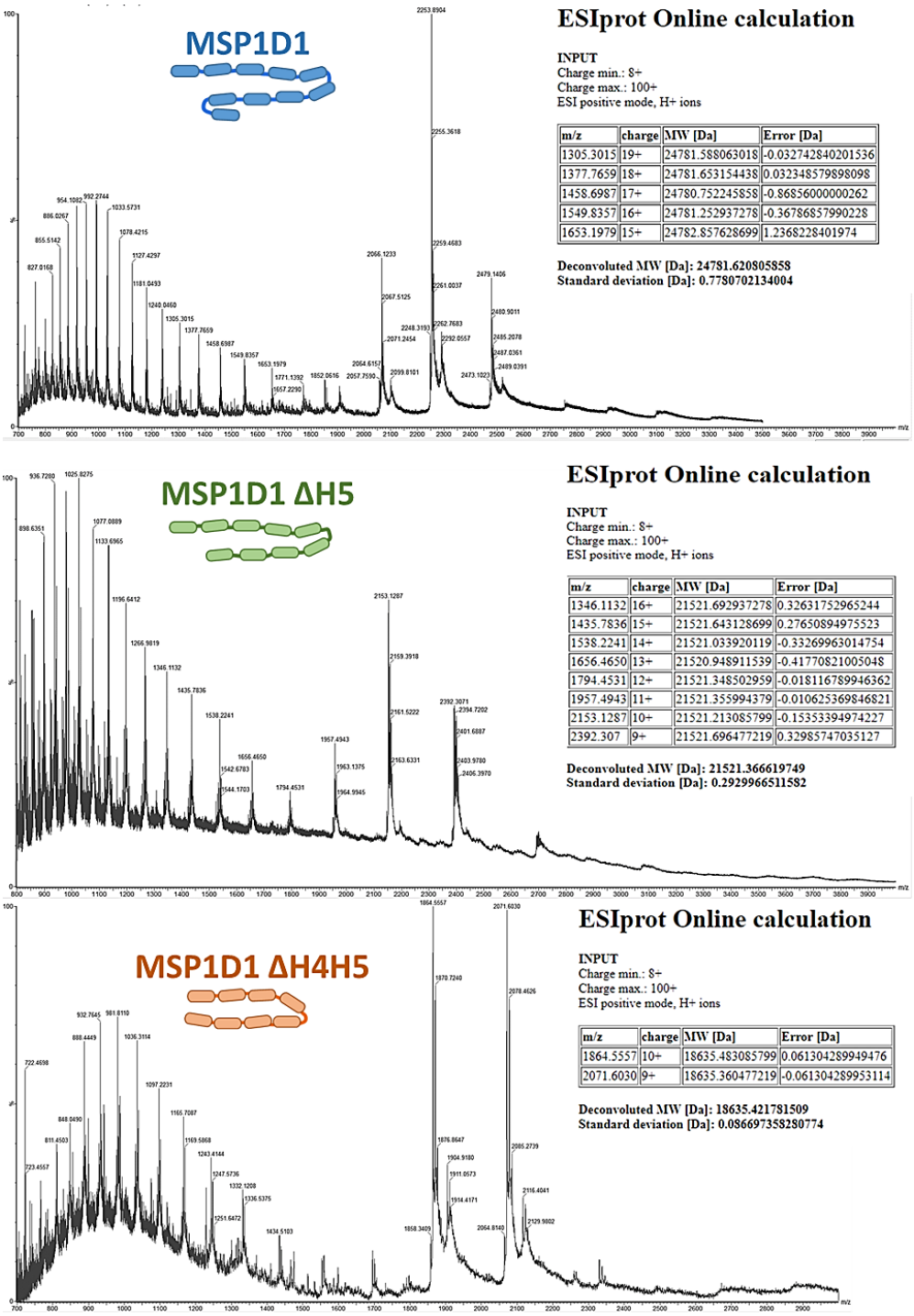

Figure 23. The native mass spectra of MSP1D1, MSP1D1 ΔH5, and MSP1D1 ΔH4H5 proteins. All MSPs were diluted to 1.5 µM in 50mM ammonium acetate pH 7.4 and infused into the mass spectrometer at a flow rate of 5 µL/min. A cartoon schematic of each MSP is shown alongside its respective mass spectrum, with cylinders representing α-helices.

Similarly, for MSP1D1 ΔH5 and MSP1D1 ΔH4H5, the native spectra exhibited two peak distribution patterns corresponding to folded and unfolded protein states (Figure 23). Calculated masses in ESIprot for MSP1D1 ΔH5 and MSP1D1 ΔH4H5 were 21521.3666 ± 0.2930 Da and 18635.4218 ± 0.0367 Da, respectively. Theoretical weights for MSP1D1 ΔH5 is 22,105.7 Da and for MSP1D1 ΔH4H5 is 19220.51 Da – these values did not deviate excessively from experimental mass values. The spectra also confirmed that each MSP was purified with no obvious degradation protein products or impurities.

3.2.2. Native MS of αSN

The native mass spectrum of intact αSN was obtained in order to confirm the presence of this exact protein in solution and identify any truncation or degradation products that might be present in the sample. The theoretical mass of αSN (based on its sequence) is 14,460 Da.

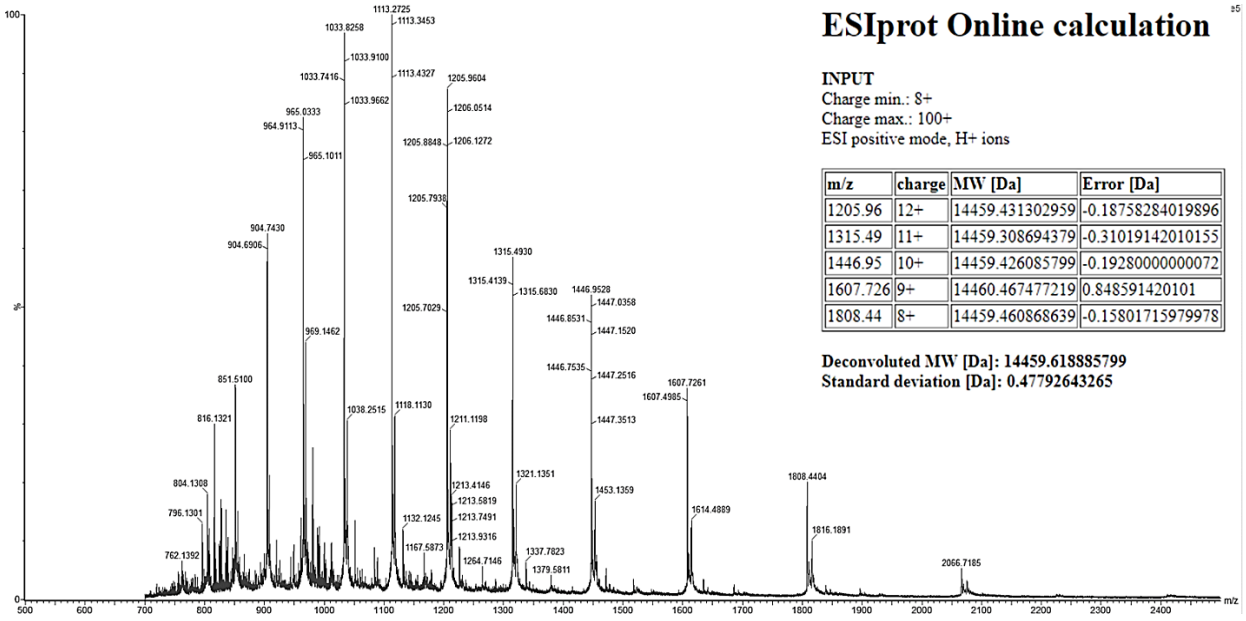

Figure 24. The native mass spectrum of αSN. αSN was diluted to 2.5 µM in 50mM ammonium acetate pH 7.4 and infused into the mass spectrometer at a flow rate of 5 µL/min.

Looking at the spectrum in Figure 24, only the unfolded protein peak distribution pattern was observed which was expected due to the disordered character of this protein (no folded secondary structure). Consecutive m/z values were entered into ESIprot which gave a deconvoluted mass value of 14,459.6189 ± 0.4778 Da. This value matched the theoretical mass perfectly. The spectrum also confirmed that αSN was purified with no degradation/truncation protein products or impurities.

3.3. Verification of Nanodisc Formation by NMR and SEC

3.3.1. 1D ^{31}P NMR of DMPC Nanodiscs – 10nm with MSP1D1 Belt, 6nm and 4nm with MSP1D1 ΔH5 and MSP1D1 ΔH4H5 Belts, Respectively

Since many studies have been done on nanodiscs with NMR in the last 10 years, this technique was chosen to verify the three differently sized nanodiscs – 10 nm with MSP1D1 belt, 6 nm and 4 nm with MSP1D1 ΔH5 and MSP1D1 ΔH4H5 belts, accordingly. ^{31}P is a hundred percent naturally abundant isotope which makes it much more sensitive than ^{13}C in NMR. Also, all lipids including DMPC have at least one phosphorous atom. Therefore, 1D ^{31}P NMR was chosen here as the best suited experiment. Figure 25 shows the NMR spectra for 10, 8 and 6 nm DMPC nanodiscs (from top to bottom), as well as a control sample of just DMPC lipid at the same concentration as in the nanodisc samples. The top three NMR spectra displayed a tall, sharp peak at around 0 ppm (Figure 25). In comparison, the bottom spectra of lipid control exhibited an almost unresolvable broad peak at around -15 ppm (Figure 25d). The sharpness of a peak in 1D NMR is reversely proportional to the transverse relaxation time (T2), and T2 is directly proportional to correlation time of the molecule (ϯc) which is simply how many revolutions a molecule undergoes in one second in solution. If the molecule is bulky then ϯc is small – not many revolutions occur in 1 s.

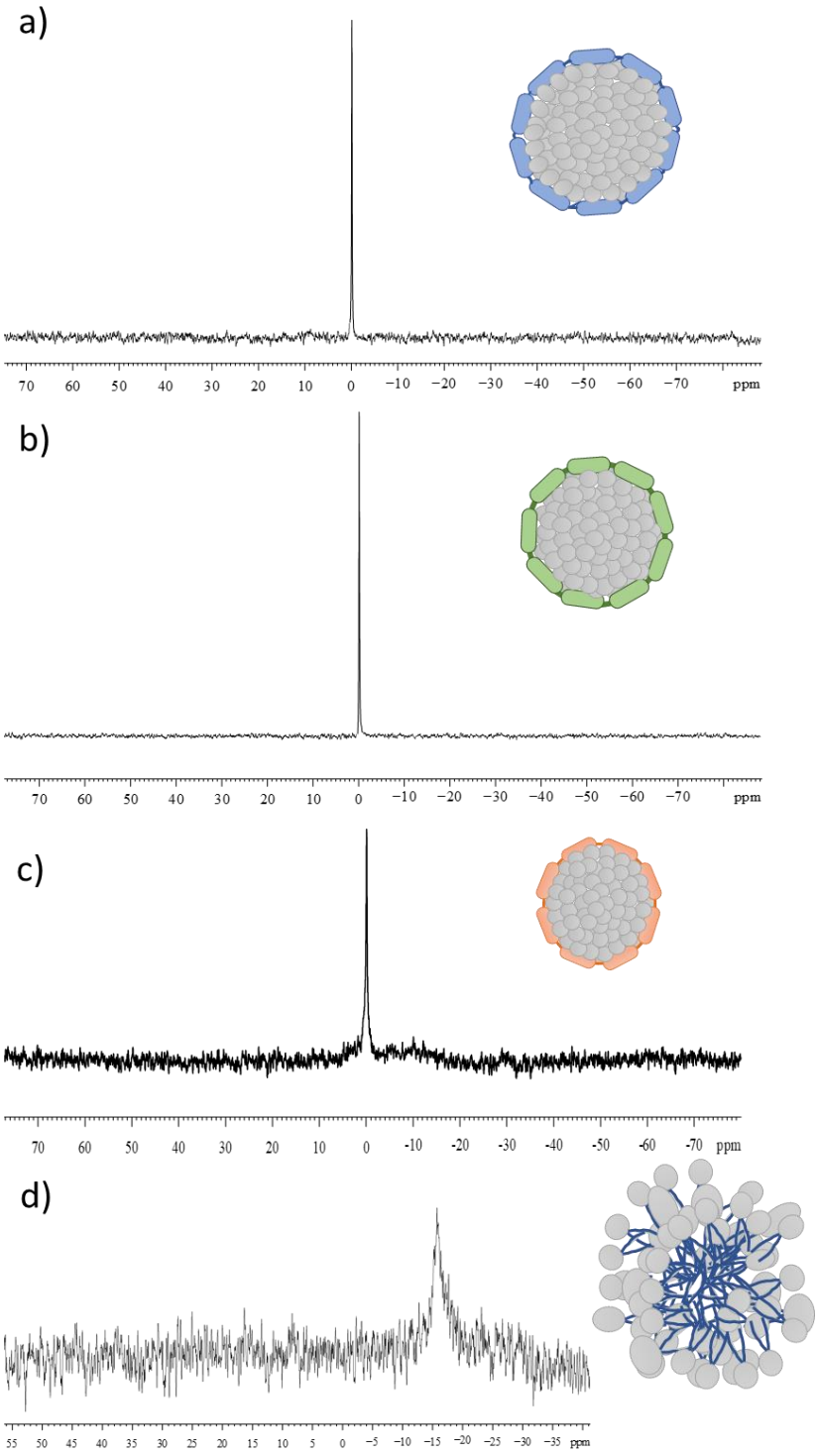

Figure 25. 1D ^{31}P NMR of DMPC nanodisc with a) MSP1D1 belt, b) MSP1D1 ΔH5 belt, and c) MSP1D1 ΔH4H5 belt, as well as, d) DMPC lipid aggregate. 1mM of DMPC diluted in 100 mM ammonium acetate with 10% D2O contained each sample of nanodiscs prior to 31P NMR experiments. These experiments were recorded at 298K on a Bruker DRX 600 spectrometer. Each spectrum was recorded in 40,960 scans with a relaxation delay of 0.77 seconds at a frequency of 242.9 MHz and 30˚ pulse angle. Spectra were processed with the XWIN-NMR software package.

In the bottom spectra, T2 is short which makes the peak broader. Therefore, broadening of the peak in the lipid control sample suggests the presence of a much bulkier substance than a formed nanodisc – possibly a lipid aggregate. This is consistent with the fact that lipids in a water-based solution tend to form globular aggregates, so that lipid hydrophobic tails are buried from the hydrophilic environment. These DMPC aggerates will have small ϯc and short T2 leading to formation of a broad peak (Figure 25d). Similar results were also observed in the 1D ^{31}P NMR studies by Lucyanna and colleagues in 2011 [170]. In their work, they also observed a broad peak at around −15 ppm which corresponded to the transition from bicellar aggregates to larger structures with slower motions – lipid aggregates [170]. In contrast, nanodiscs are much smaller and compact structures than lipid aggregates and rotated with larger correlation times, which made T2 long, producing sharp peaks (Figure 25 a, b, and c). Based on the results in Figure 25, the successful formation of all three (10, 8 and 6 nm) DMPC nanodiscs was established.

3.3.1. SEC and SDS-PAGE of 6 nm DMPC Nanodisc

Many nanodisc protocols have employed SEC for confirmation of nanodisc formation. Additionally, SEC is an excellent technique for dialysis of a sample into a MS compatible buffer while separating the nanodiscs from unbounded lipids, detergents and proteins. The SEC chromatogram for the 6 nm DMPC nanodisc (MSP1D1 ΔH5 belt) is shown in Figure 26 along with a SDS-PAGE gel depicting elution samples under representative chromatographic peaks. The blue peak trace represents the UV absorbance of aromatic amino acids (Phe, Tyr, Trp) at 280 nm from the MSP1D1 ΔH5 belt (Figure 26). The chromatogram has two main peaks: the first one eluting at 8 to 10 mL (elutions B8 to B5), and the second one at 13 mL (elution C1) (Figure 26).

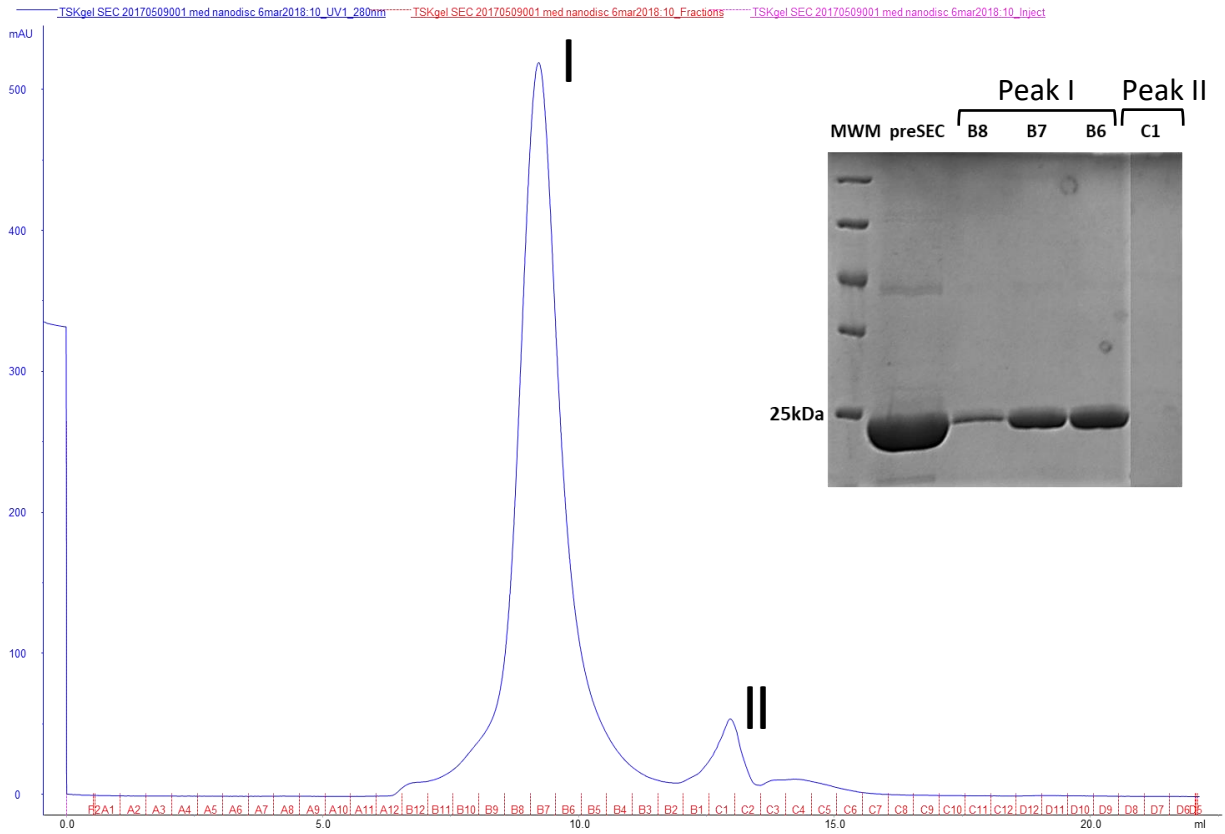

Figure 26. Size exclusion chromatogram of the 6nm DMPC nanodisc (MSP1D1 ΔH5 belt) with the corresponding SDS-PAGE of the main peak elutions. The blue peak trace in the chromatogram corresponds to UV absorbance at 280 nm. SDS-PAGE displays (from left to right) molecular weight marker (ThermoFisher #PI-26616), nanodisc sample before SEC, elutions B8 to B6 and C1.

Given that larger molecular weight species elute earlier, the first peak was assigned to correspond to a much heavier species than the second peak. According to SDS-PAGE, elutions under the first peak (B8 to B5) displayed only one band below the 25 kDa mark which was assigned to the MSP1D1 ΔH5 protein (molecular mass 22.2 kDa) (Figure 26). Hence, the first chromatographic peak corresponds to the 6 nm DMPC nanodisc. This deduction was also supported by various literature results. For example, Hagn *et al*. have shown that a single SEC peak at 14.3 mL corresponds to the 95kDa DMPC nanodisc with MSP1D1 ΔH5 belt (column used in their research was analogous to the TSKgel column BioAssist G3SWXL column and the flow rate

was identical to the one used in this study) [108]. Even though 14.3 mL corresponds more to the elution of the second peak in Figure 26, the discrepancy can be explained by different chromatographic properties of the column used by Hagn *et al* [108]. Another research paper by Helbing *et al*. has confirmed the MSP1D1:DOPC nanodisc through an elution peak at 18 min using the same column and flow rate as in this study [171]. Fraction B7 under the first peak in Figure 26 eluted at 18 min. Both Figure 26 and reported literature results support the successful formation and purification of the 6 nm DMPC nanodisc (MSP1D1 ΔH5 belt). The fraction under the second peak showed no protein bands (Figure 26). This likely corresponds to the elution of small peptide fragments and any excess MSP1D1 ΔH5 that was not associated with the 6 nm nanodisc.

3.4. Verification of αSN – 6 nm DMPC Nanodisc Complex by SEC, SDS-PAGE and ESI-MS

Protein-nanodisc complex was formed by mixing the DMPC nanodisc (MSP1D1 ΔH5 belt) with αSN at a 1:1 ratio and left incubating for 1 hour at 37°C with shaking at 100 rpm. The SEC experiment was performed in order to confirm complex formation, transfer the sample into an MS compatible buffer and purify it from any unbound material like lipids, detergents and proteins. The corresponding chromatogram and SDS-PAGE gel containing representative elution samples are shown in Figure 27. The blue peak trace represents UV absorbance of aromatic amino acids (Phe, Tyr, Trp) at 280 nm from the MSP1D1 ΔH5 belt and αSN (Figure 27). Similar to the SEC chromatogram of empty nanodiscs (Figure 26), the chromatogram in Figure 27 had two main peaks: the first one at 8-10 mL with fractions B7 to B5, and the second one at 11-13 mL with fractions B2 to C1. However, the intensities of the peaks are different, with the second peak

having a higher intensity than the first (Figure 27), signifying that smaller molecular weight species was present at a higher concentration or had more aromatic amino acid residues present.

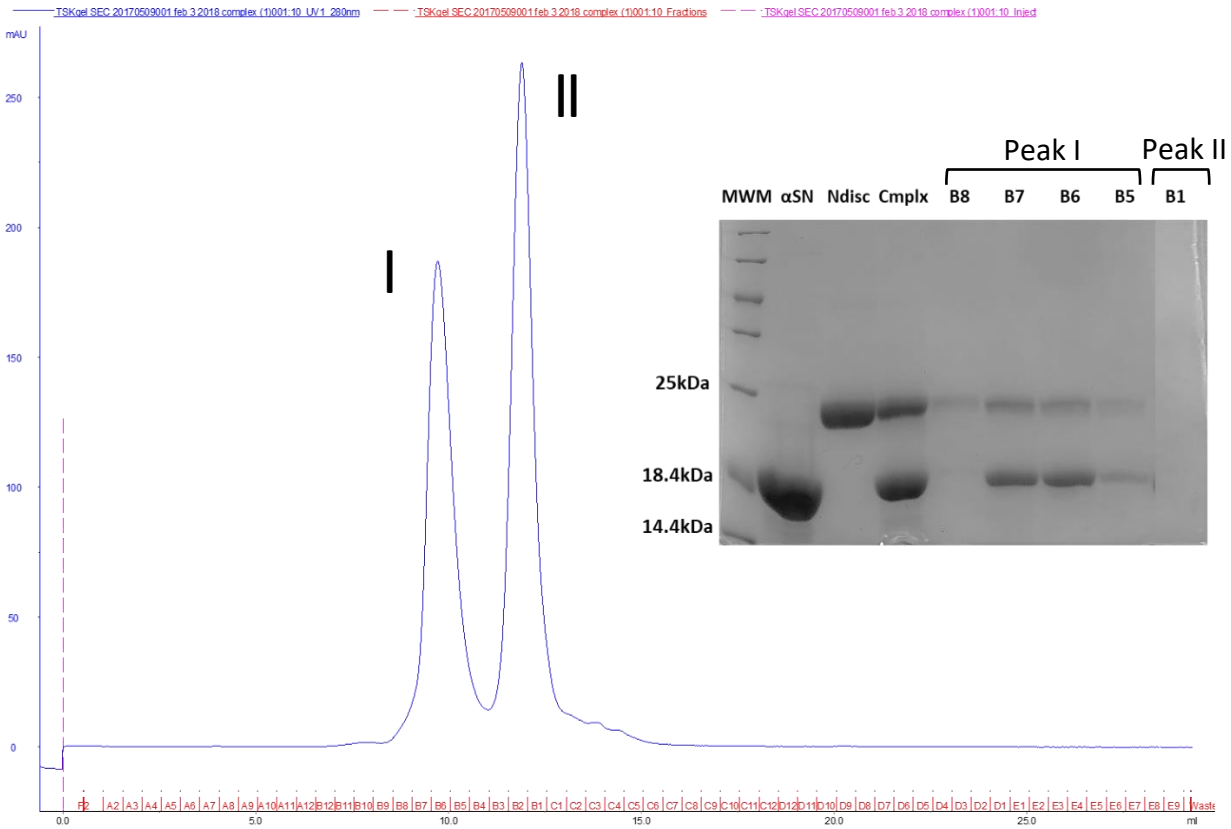

Figure 27. Size exclusion chromatogram of αSN - 6nm DMPC nanodisc complex with the corresponding SDS-PAGE of the main peak elutions. The blue peak trace in the chromatogram corresponds to UV absorbance at 280 nm. SDS-PAGE displays (from left to right) molecular weight marker (ThermoFisher #PI-26616), αSN before complex formation, nanodisc sample before complex formation, complex of αSN with nanodisc (1:1) before SEC, elutions B8 to B5 and B1.

SDS-PAGE was used to visualize the species eluted in these two peaks (Figure 27). An αSN sample prior to complex formation (2nd lane with a thick band between 18.4 and 14.4 kDa marks in Figure 27) and a nanodisc sample (3rd lane with a thick band just below the 25kDa mark) confirmed purity of the samples prior to complex formation (Figure 27). The formed complex before SEC is shown in the 4th lane to make sure that both αSN and MSP1D1 ΔH5 belt did not degrade during the incubation time (Figure 27). Two thick bands in the 5th lane corresponding to these proteins confirmed their presence and intactness (Figure 27). Elutions matching the first

chromatographic peak (B8, B7, B6 and B5) also contain two bands corresponding to αSN and MSP1D1 ΔH5 (Figure 27). This result suggests that fractions under the first peak contained the protein-nanodisc complex. The drop in concentration of B8-B5 protein bands was due to the dilution of the complex sample into four fractions (Figure 27). It is to be noted that B8 showed a thin but distinguishable band only for MSP1D1 ΔH5 and that the concentration of αSN was either too low to visualize or not present (Figure 27). Since the empty nanodisc in Figure 26 had eluted at the same volume and retention time as the complex in Figure 27, it is reasonable to propose that elution B8 corresponds to an empty nanodisc (as in Figure 26), with all downstream elutions starting to contain the complex sample (Figure 27). It was unexpected to observe no shift between the first peaks in Figure 26 and 27, as nanodiscs bound with αSN should elute earlier by means of being a heavier species. However, it is hypothesized that αSN can stabilize the nanodisc complex and make it more compact which would lead to a later than expected elution time. This argument is supported by evidence that αSN's binding to a lipid bilayer affects not only the properties of the protein but also the properties of the membrane (membrane remodeling, thinning and/or expansion) [172]. For example, Braun *et al*. on the basis of fluorescence correlation spectroscopy and POPG vesicle clearance assays had deducted that the NAC region of αSN was essential in stabilizing protein-lipid complexes and, in doing so, promotes the organization of the bilayer surface [173].

Solely relying on the SDS-PAGE results under the first peak in Figure 27, formation of the αSN – 6nm DMPC nanodisc complex was confirmed. As in Figure 26, the B1 fraction contained no proteins but was composed of small molecular weight peptides which was verified by using ESI-MS (results not shown).

Intact mass spectra of the 6nm DMPC nanodisc and complex of αSN - 6nm DMPC nanodisc were performed in order to confirm their masses. Mass spectra for both of these samples are shown in Figure 28. Both spectra displayed a broad peak distribution pattern looking almost like a "hump" – the top hump with a centroid around m/z 6000, and the bottom around m/z 5000. Unfortunately, the peak resolution of these two "humps" was too low for charge states to be identified, and, therefore, no deconvoluted mass was obtained (Figure 28). However, a comparison between the relative position of the centroids of these envelopes was performed.

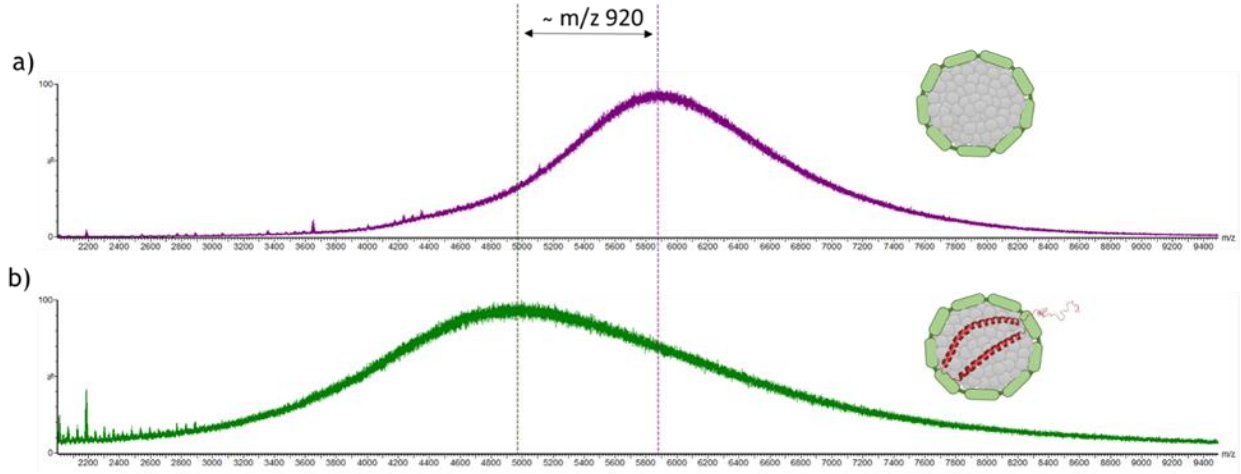

Figure 28. Mass spectra of a) intact 6nm DMPC nanodisc, and b) intact complex of αSN - 6nm DMPC nanodisc. Purple and green dotted lines represent the approximated centroids for each spectra. Data was obtained using a Waters Synapt G1 instrument with increased backing pressure to 5.32 bar.

The nanodisc centroid was approximated to be around m/z 5880 which is about 920 m/z higher than the approximated centroid for the complex (Figure 28). Even though the complex was expected to be heavier, it seemed to pick up more charge due to αSN's polar and positively charged (Lys) residues on the surface of the nanodisc. These additional charges could have caused the overall shift to a lower m/z range. To conclude, no deconvoluted masses of both 6 nm DMPC nanodisc or complex was obtained, so the MS identity of these two samples was failed to

be confirmed. However, the difference in mass spectra shape could be used as a guidance for differentiation of one sample from another (assuming future replicates of this experiment would be consistent).

3.5. Conformational Analysis of αSN When Bound to 6 nm DMPC Nanodisc; Equilibrium Studies

To obtain peptide specific insights into the interactions of αSN with the 6nm DMPC nanodisc, equilibrium TRESI-HDX-MS studies were performed. Figure 29 shows equilibrium data in the form of deuterium uptake difference plots and corresponding heat-mapped 3D protein structures of αSN on the nanodisc. Difference plots of two technical replicates have αSN's peptides in the order from N- to C-terminus on the x-axis, and percentage difference of deuterium uptake between complex and αSN alone (deuterium uptake of complex – deuterium uptake of αSN = ΔD uptake) on the y-axis (Figure 29). Heat-mapped 3D protein structures correspond only to the second replicate where red corresponds to an increase in deuterium uptake and blue to a decrease (Figure 29). Dotted red and blue lines represent two standard deviation values for each peptide.

In the earlier time points – 0.115 s and 0.332 s in the 2nd replicate and 0.38 s in the 1st replicate, the difference in deuterium uptake generally decreases (Figure 29). The three distinct peptide regions of αSN showing the most drastic decreases are AEKTKQGVAE (residues 19-28), VTNVGGAVVTGVTAVAQK (63-80), and TVEGAGSIAAATGFVKK (81-97) (Figure 29).

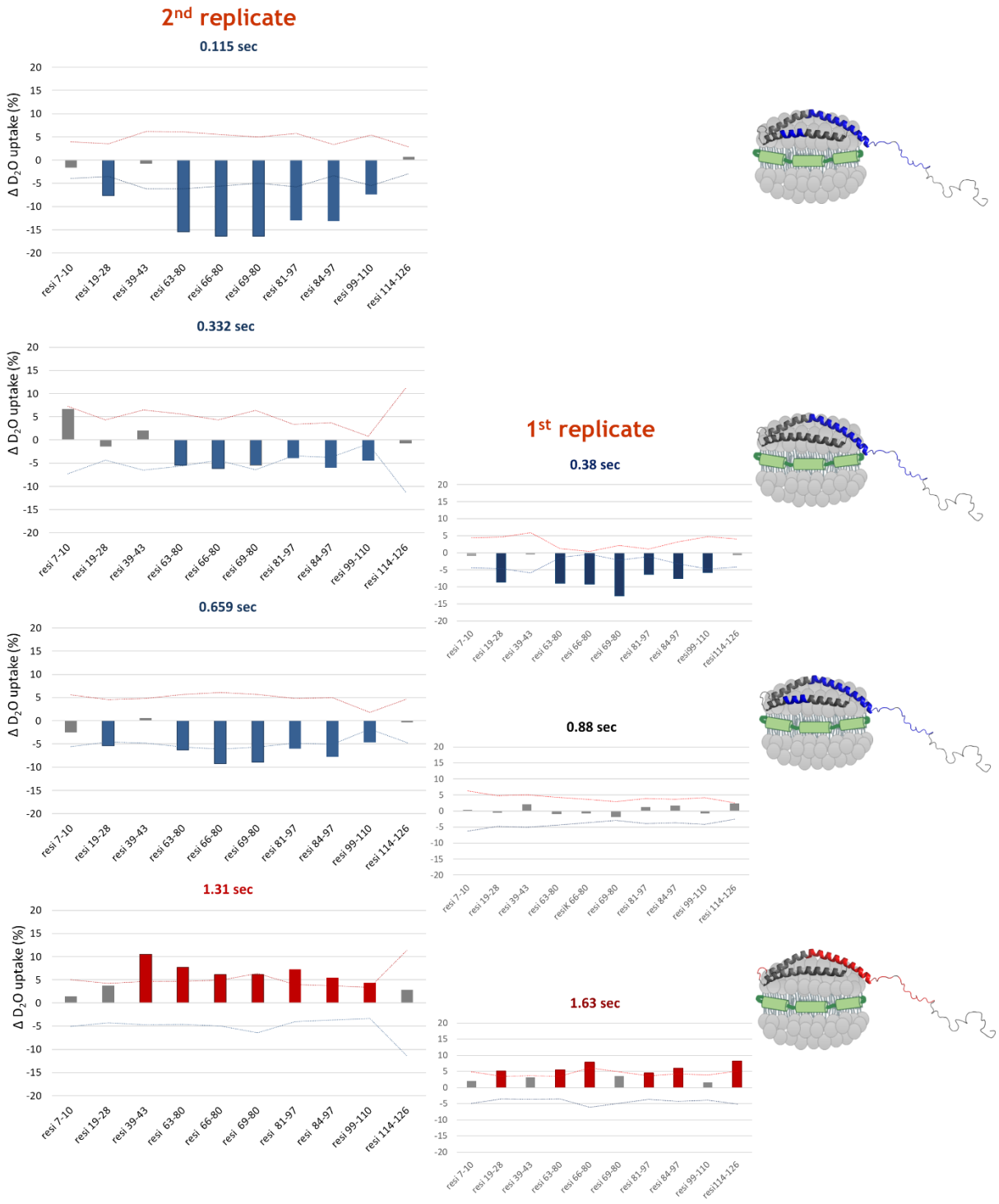

Figure 29. Two technical replicates of deuterium uptake difference plots between complex and αSN alone; equilibrium studies. The first replicate data is displayed in small boxes beside the second replicate data. The significant differences in deuterium uptake are mapped onto the structure of αSN (PDB ID:1XQ8), where blue color represents a decrease in deuterium uptake, and red an increase.

AEKTKQGVAE showed a decrease of about 7% at 0.115 s and 0.38 s (2nd and 1st replicate accordingly), but at 0.332 sec in the 2nd replicate was below the two standard deviations value and displayed a difference of about -3%. VTNVGGAVVTGVTAVAQK displayed the greatest decrease among the three regions – around -15% at 0.115 s (2nd rep), -10% at 0.38 sec (1st rep) and -5% at 0.332 s (2nd rep) (Figure 29). TVEGAGSIAAATGFVKK had a similar behaviour – around -13% at 0.115 s (2nd rep), -7% at 0.38 sec (1st rep) and -6% at 0.332 s (2nd rep) (Figure 29). These results indicate that when αSN was in a complex with the nanodisc, deuterium uptake of amide hydrogens decreased compared to free αSN. As mentioned in section 1.1.2.1, the HDX rate is highly dependent on hydrogen bonding and solvent accessibility, and deuterium exchange is slower in folded proteins which are characterized by extensive hydrogen bonding networks and restricted solvent accessibility. Therefore, our data suggests that the conformation of αSN was changed when complexed to nanodiscs toward a more dynamically restricted form with a slower deuterium uptake. In particular, peptides belonging to the NAC region (residues 63-80, 66-80, 69-80, 81-97 and 84-97) displayed the greatest protection from deuterium in the αSN-nanodisc complex which suggests that this is the specific interaction region with the lipid bilayer. In longer time points – 0.659 s in the 2nd replicate and 0.88 s in the 1st replicate, the difference in deuterium uptake still decrease or do not show any significant difference (Figure 29). Here, the longer time point from the second replicate did not change significantly from the 0.322 s or 0.38 s difference plots (Figure 29). The 0.88 s plot did not show any significant difference in deuterium uptake signifying no change in αSN's structural dynamics upon interaction with lipids. The longest time points, 1.31 s and 1.63 s (2nd and 1st replicate accordingly) showed increases in the difference in deuterium uptake (Figure 29). Except for AEKTKQGVAE (residues 19-28), peptides from the NAC

region and C-terminus tail showed higher deuterium uptake (5-10%) compared to peptides in free αSN.

The transition from a decrease to increase in deuterium uptake during longer time points was an unexpected result. If αSN was bound to nanodiscs, decreases in deuterium uptake were expected to become even more prominent. The results in Figure 29 could be justified by another model – that αSN exhibits transient interactions with the 6 nm DMPC nanodiscs. In the equilibrium study there are different populations of αSN that may form, for example, αSN bound to the nanodisc, αSN that partially interacts with the nanodisc, and completely unbound αSN. The interchange of αSN between these populations may occur making one population more dominant over the other. It seems that under 0.659 s the dominant population is where αSN is conformationally restricted or more structured than free αSN (either bound αSN to nanodiscs or transiently interacting with them). Therefore, the HDX "snapshot" of earlier time points show decreases in deuterium uptake. However, at the 1.63 s reaction time, the transition of αSN from a conformationally restricted state to a more extended structure takes place leading to domination of an extended (and possibly more amyloidogenic) αSN population. Therefore, the HDX "snapshot" of the longer time points show increases in deuterium uptake. Unfortunately, no third technical replicate was obtained to make any statistical conclusions regarding this model. This consistency issue was addressed by running HDX-MS experiments on free αSN and complex on the same day. In addition, complex preparation and SEC clean-up was performed on the same day as the HDX-MS experiment. Last but not least, the pH reading of the quenched peptide solution was taken after each time point in order to avoid back-exchange (loss of deuterium label) and ensure successful quenching. Figure 30 shows the percentage of deuterium

uptake for αSN peptides (free protein, no nanodiscs present) at four randomly selected days, yielding highly consistent data.

Figure 30. Deuterium uptake for free αSN on four randomly selected days. Percentage of deuterium uptake for each peptide is represented as a colored dot where each color belongs to one of the four days – 10Feb2018 dark red, 08Feb2018 violet, 11Dec2017 yellow, and 14Oct2017 brown.

Peptides from NAC region of αSN exhibited very consistent percentage for deuterium uptake in all time points for all four different dates (Figure 30). The only outstanding values were exhibited by the NAC region peptides at 1.3 s on 14OCT (brown), but the overall line trend was very similar to the three other dates (Figure 30). Parallel to the NAC region peptides, C-terminus peptides and AEKTKQGVAE showed little deviation from date-to-date and the overall line trend for all four dates were the same (Figure 30). The most differences between different dates were observed in peptide YVGSK (resi 39-43) which locates at the isthmus between two α-helices in αSN. Due to its position in αSN, YVGSK was expected to exhibit various HDX rates due to the steric effects of nearby amino acid groups composing αSN's helices. Therefore, it was proposed that

variety of conformational ensembles that YVGSK peptide may adapt influenced HDX rate and deuterium uptake profile (Figure 30). It is important to note that YVGSK is a very short peptide with only three deuterium exchange sites – this limited amount of exchange sites could also contribute to such date-to-date variability (Figure 30). Overall, it can be stated that free αSN's deuterium uptake was consistent in all four randomly selected days in Figure 30. Consequently, the most variability and inconsistency in deuterium uptake results came from the αSN-nanodisc complex which led to inconsistencies in difference plots between the complex and αSN.

To conclude, on the basis of equilibrium TRESI-HDX-MS data, αSN was proposed to exhibit transient interactions with lipid bilayer of the 6 nm DMPC nanodisc. The third technical replicate supporting this deduction was not obtained due to the inconsistencies in the subsequent acquired data sets. Based on Figure 30 results, it was determined that inconsistencies came from the αSN-nanodisc complex HDX profiles indicating an erratic and infrequent structural behaviour of αSN in the presence of DMPC bilayer. The deduction of transient interaction rather than stable binding of αSN to DMPC nanodisc was backed up by the recent study of Viennet *et al*. where TROSI-HSQC NMR proved no binding of αSN to DMPC nanodisc as no differences to the spectrum of αSN in the presence/absence of nanodiscs was detected [173].

3.6. Conformational Analysis of αSN During the Binding Event to 6 nm DMPC and DMPC-POPS Nanodisc; Kinetic Studies

Kinetic studies were performed in order to elucidate the folding pathway of αSN into an α-helix upon binding to the phospholipid bilayer of the 6 nm DMPC and DMPC-POPS nanodisc. The lipid-binding regions of αSN have been known for a while, but the peptides involved in early-on

launching on the membrane and transition folding states of αSN are not know yet [125,141,160]. It is important to note the difference between kinetic experiments in this section from equilibrium studies in section 3.4. In equilibrium studies, complex of αSN and the 6 nm DMPC nanodisc was pre-made and all structural transitions of αSN linked to the interaction with lipids bilayer took place before the HDX reaction. In contrast, kinetic studies involved hydrogen exchange while the complex was forming, meaning αSN meets up nanodiscs only in the HDX reaction chamber. Therefore, kinetic studies allows for probing the dynamics of weakly structured regions of αSN during the first moments of the interaction with the nanodisc bilayer. The results of kinetic TRESI-HDX-MS experiment were represented in Figure 31 in the form of deuterium uptake difference plots between the forming complex and αSN alone (deuterium uptake of forming complex – deuterium uptake of αSN = ΔD uptake). The correlated PyMOL structures of αSN with mapped difference in deuterium uptake were also presented in Figure 31 for better visualization of the regions most involved in structural changes.

Overall, kinetic data displayed the decrease in deuterium uptake across all time points, indicating a more dynamically-rigid structure of αSN in the presence of the 6 nm DMPC nanodiscs (Figure 31). The highest decreases in deuterium uptake were exhibited by the first two peptides AEKTKQGVAE (19-28) and YVGSK (39-43) – around -20% at 0.12 s and 0.33 s, and around -10% to -14% at 0.66 s and 1.31 s. AEKTKQGVAE and YVGSK belong to the αSN's amphipathic region which exploits the highest propensity of forming amphipathic helices, especially in the presence of lipid membranes [125,146]. These two peptides were proposed to be the first ones in αSN's sequence to start conformational changes in the presence of the lipid bilayer, presumably there are also the first ones to initiate folding process of αSN into the extended helical state.

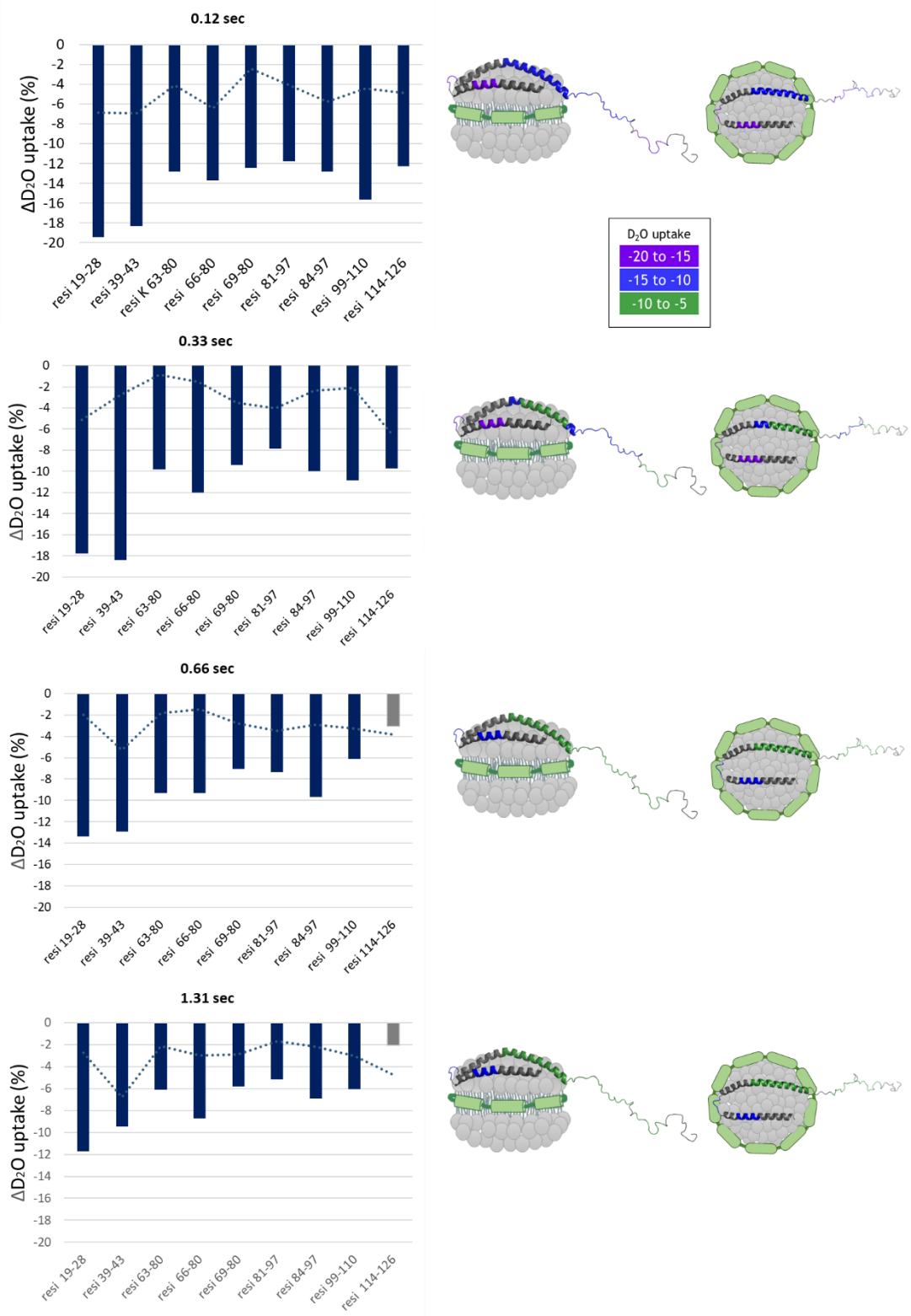

Figure 31. **Deuterium uptake difference plot between αSN – 6 nm DMPC nanodisc complex and αSN alone: kinetic studies.** The deuterium uptake mapped onto the structure of αSN (PDB ID:1XQ8), where purple represents -20 to -15 percent decrease in D_2O uptake, blue indicates -15 to -10 per cent, and green -10 to -5.

Unfortunately, this deduction cannot be fully evidenced unless all the peptides in amphipathic region are analyzed. Nevertheless, this data was partially supported by the findings of Bartels and his colleagues –the first 20 amino acids of amphipathic region were the earliest to transition into helical form pulling the rest of the lipid-binding region to undergo a coil/helix transition [78].

Peptides from the hydrophobic region of αSN (residues 63 to 97) showed lower deuterium uptake than the amphipathic region across all four time points: -15 to -10 % at 0.12 sec, and -10 to -5 % at 0.33 s, 0.66 s and 1.31 s (Figure 31). But the decrease in deuterium uptake still indicated that the HDX rate got slower in αSN when introduced to the nanodisc, possibly due to the newly formed hydrogen bonding and restricted solvent accessibility. This result suggested a more structured conformation of the NAC region compared to the intrinsically disordered αSN. Since the NAC region only follows the coil/helix transition after the amphipathic region, the lower intensity in deuterium uptake compared to the first two peptides in Figure 31 was expected. Also, according to Dikiy *et al*. second helix of αSN (attributed to the NAC region) was proposed to kick itself out with the help of C-terminus in order to obtain the partially helical intermediate state (Figure 14), meaning this region is less stabilized by the membrane bilayer and more structurally dynamic. This could also explain the higher level of deuterium uptake by the NAC region in the αSN - DMPC nanodiscs forming complex compared to AEKTKQGVAE and YVGSK peptides in the same sample.

The C-terminus peptides QLGKNEEGAPQE (99-110) and EDMPVDPDNEAYE (114-126) also exhibited substantial decrease in deuterium uptake in the earlier time points (0.12 s and 0.33 s) – up to -16% and -11% for QLGKNEEGAPQE, as well as, -13% and -10% for EDMPVDPDNEAYE (Figure 31). However, in later time points EDMPVDPDNEAYE (114-126) showed no significant

difference indicating the same structural behaviour as in free αSN. The decrease in deuterium uptake for QLGKNEEGAPQE (99-110) got lowered to around -10% (Figure 31). As mentioned earlier, the C-terminus of αSN usually remains unstructured and either works as a protein-protein interaction motif or provides long-range interactions for stabilization of NAC and N-terminus regions [125,156,157]. The data for the C-terminus peptides was conflicting, as no significant change was expected. But the lower deuterium uptake in this region clearly indicated structural rigidity and compactness of the C-terminus when introduced to the 6 nm DMPC nanodisc. The possible explanation was that the C-terminus region assisted in the reduction of αSN's disordered character towards a folded species through interaction with either other regions of αSN, or nanodisc. This explanation could not be proved by the kinetic data nor backed up by any scientific literature.

In addition to the kinetic studies with DMPC nanodiscs, similar studies were performed with the 6 nm DMPC-POPS nanodiscs. POPS lipids have negatively charged polar heads that can contribute to the increased binding ability of αSN to the vesicle's membrane [154,173]. Kinetic plots for the seven peptides covering the three major parts of αSN were shown in Figure 32 (Part 1 and 2). The x-axis represented six time points at which deuterium uptake measurements were acquired. The y-axis represented percentage of deuterium uptake at each time point starting from 60%. The 0 s time point was not measured and, therefore, omitted in the kinetics plots represented in Figure 32, Part 1 and 2. Two technical replicates were shown in Figure 32, Part 1 and 2, where the second replicate kinetic plots were slightly shaded for visual distinction between the two sets of the HDX results.

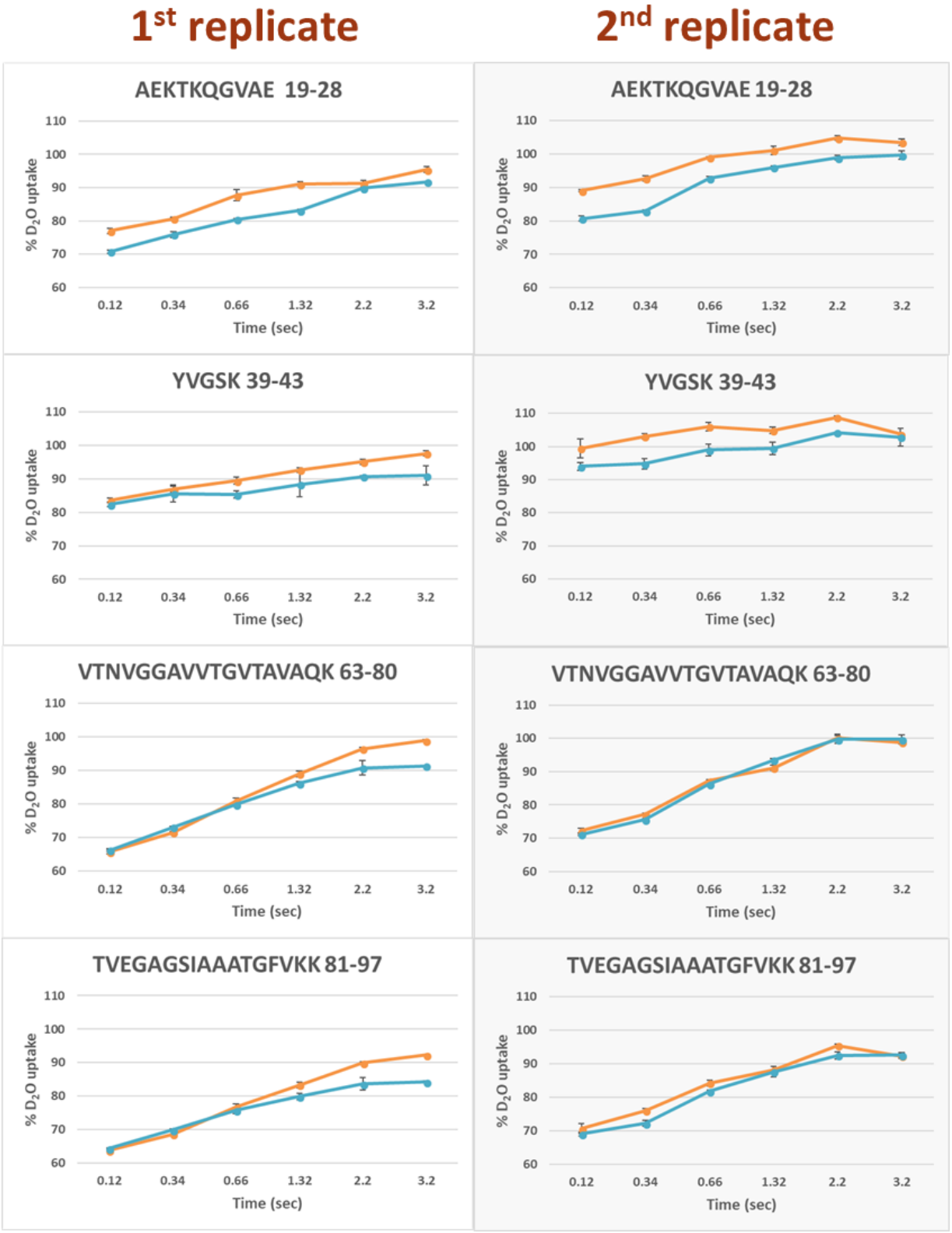

Figure 32. Part 1. Kinetic plots for αSN alone (orange line) and αSN exposed to 6nm DMPC-POPS nanodisc (turquoise line) during the kinetic studies.

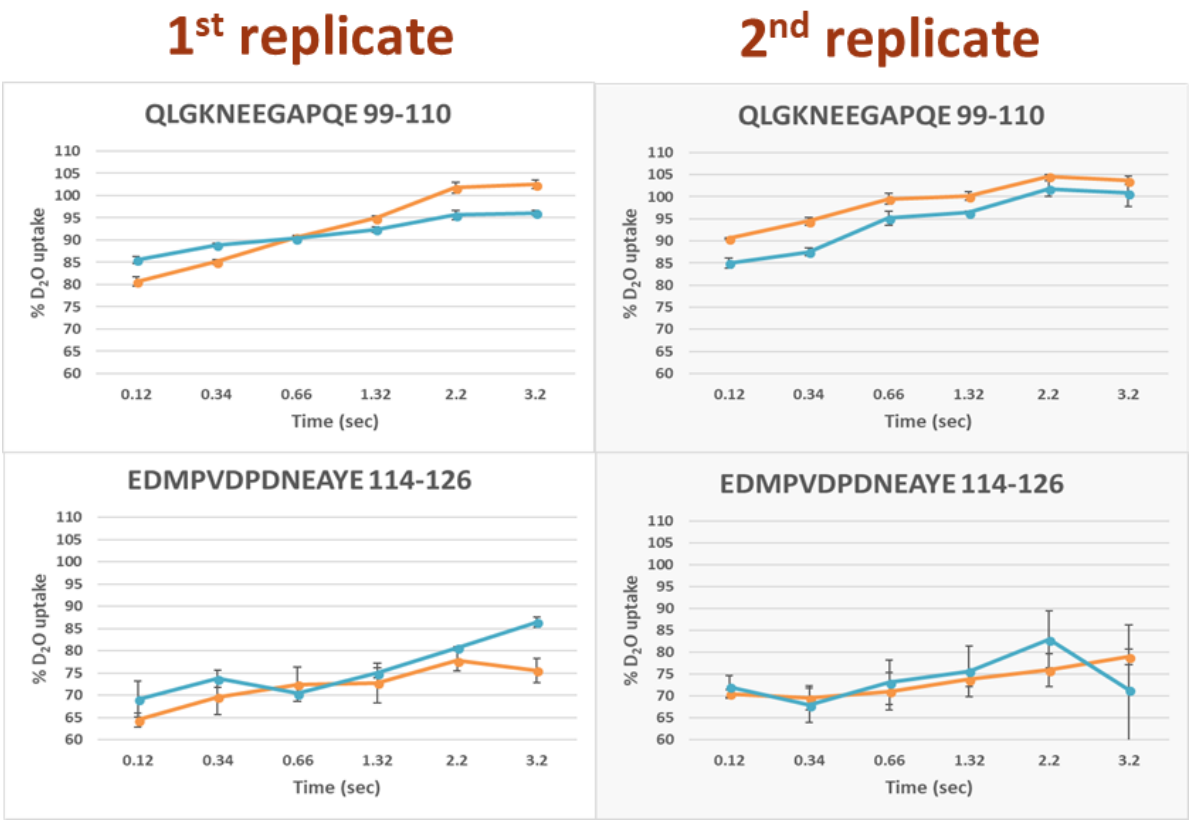

Figure 32. Part 2. Kinetic plots for αSN alone (orange line) and αSN exposed to 6nm DMPC-POPS nanodisc (turquoise line) during the kinetic studies experiment.

Analyzing Figure 32, Part 1 peptides from the amphipathic region of αSN, AEKTKQGVAE (19-28) and YVGSK (39-43), showed the highest difference in deuterium uptake between the αSN-nanodisc forming complex and the free αSN. This data agrees with the results obtained in Figure 31, except that deuterium uptake was within -10% for the both replicates in Figure 32, Part 1. The decrease in deuterium uptake for these two peptides supported the previous conclusion of initiating the folding process of αSN into an extended helix. Negatively charged POPS lipids did not increase the binding capacities of αSN to the nanodisc bilayer, but rather reduced it.

The NAC region peptides VTNVGGAVVTGVTAVAQK (63-80) and TVEGAGSIAAATGFVKK (81-97) gave similar results in both replicates for the early time points (0.12s, 0.33 s and 0.66 s) – deuterium uptake for free αSN and the αSN-nanodisc forming complex was almost the same

(Figure 32, Part 1). This data suggested that no lipid-protein interaction or folding of this region into a more structurally rigid state occurred. The longer time points (1.3 s, 2.3 s, and 3.2 s) displayed different results for different replicates. In the 1st replicate, deuterium uptake for the αSN-nanodisc complex exhibited decreases starting from 4-5% to ~8% (Figure 32, Part 1). No differences were present in the 2nd replicate (Figure 32, Part 1). Third replicate is needed in order to confidently interpret αSN's structural behaviour past 1.3 s. The HDX profiles for the NAC region peptides in Figure 32, Part 1 were quite dissimilar to Figure 31 results. Once more, the presence of 20% POPS lipids in the nanodiscs seemed to have no affect on binding properties of αSN to the membrane bilayer. Overall, NAC region displayed no signs of a protein-lipid interaction in kinetic studies with the 6 nm DMPC-POPS nanodiscs.

Kinetic plots for peptides in the C-terminus region, EDMPVDPDNEAYE (114-126) and QLGKNEEGAPQE (99-110) were represented in Figure 32, Part 2. The deuterium uptake results for EDMPVDPDNEAYE (114-126) demonstrated substantial error values for most of the time points, therefore, no clear result interpretation could be made (Figure 32, Part 1). However, this infrequent deuterium uptake may refer to the disordered behaviour of C-terminus region which obtains ensemble of conformational states with different HDX profiles. QLGKNEEGAPQE (99-110) displayed lower deuterium uptake after 0.66 s in both replicates for the αSN–nanodisc forming complex. Opposite results were observed before 0.66 s where the 1st replicate exhibited the higher deuterium uptake for the complex sample, and the 2nd replicate even a bigger decrease than after 0.66s (Figure 32, Part 1). The third replicate is needed to make any constructive observation about the C-terminus structural behaviour when αSN introduced to the DMPC-POPS nanodiscs.

Before any final conclusions were made about the kinetic studies results, the comparison of the three replicate data sets was analyzed in the form of summed difference plots in Figure 33. The differences in deuterium uptake were summed across all acquired time points for: A) 1st replicate corresponding to the HDX studies of αSN - 6 nm DMPC nanodisc complex (Figure 31), B) and C) 1st and 2nd replicates corresponding to the HDX studies of αSN - 6 nm DMPC-POPS nanodisc complex (Figure 32), respectively.

For all three plots in Figure 33, the most common feature was a substantial decrease in the deuterium uptake for peptides in the amphipathic region of αSN (amino acids 12 to 43). The TRESI-HDX-MS results here supported that the most structural folding occurred in the peptide 19-28, as it showed the highest decrease in deuterium uptake (Figure 33). These results were in agreement with literature where the amphipathic region peptides displayed the highest propensity to form α-helices and were assigned to be the first ones to initiate structural folding in the presence of the vesicle's membrane [78]. The NAC region for plots B) and C) displayed very little decrease in deuterium uptake across all 6 time points (Figure 33). Compared to the aliphatic region of αSN, little structural refolding happened in the NAC region. These results rejected the idea of αSN obtaining the extended-helix or the broken-helix states upon the first few seconds of interactions with the DMPC-POPS nanodiscs. However, as previously mentioned, the NAC region only follows the amphipathic part in a coil/helix transition (this was more distinct in the longer time points in Figure 32). Therefore, it takes time to fold into a structured helix which could not be captured in millisecond time-scale of the kinetic experiment [78]. The NAC region in plot A) showed more of a decrease in deuterium uptake than the other two plots, suggesting some structural folding due to some transient interaction with the nanodisc's membrane.

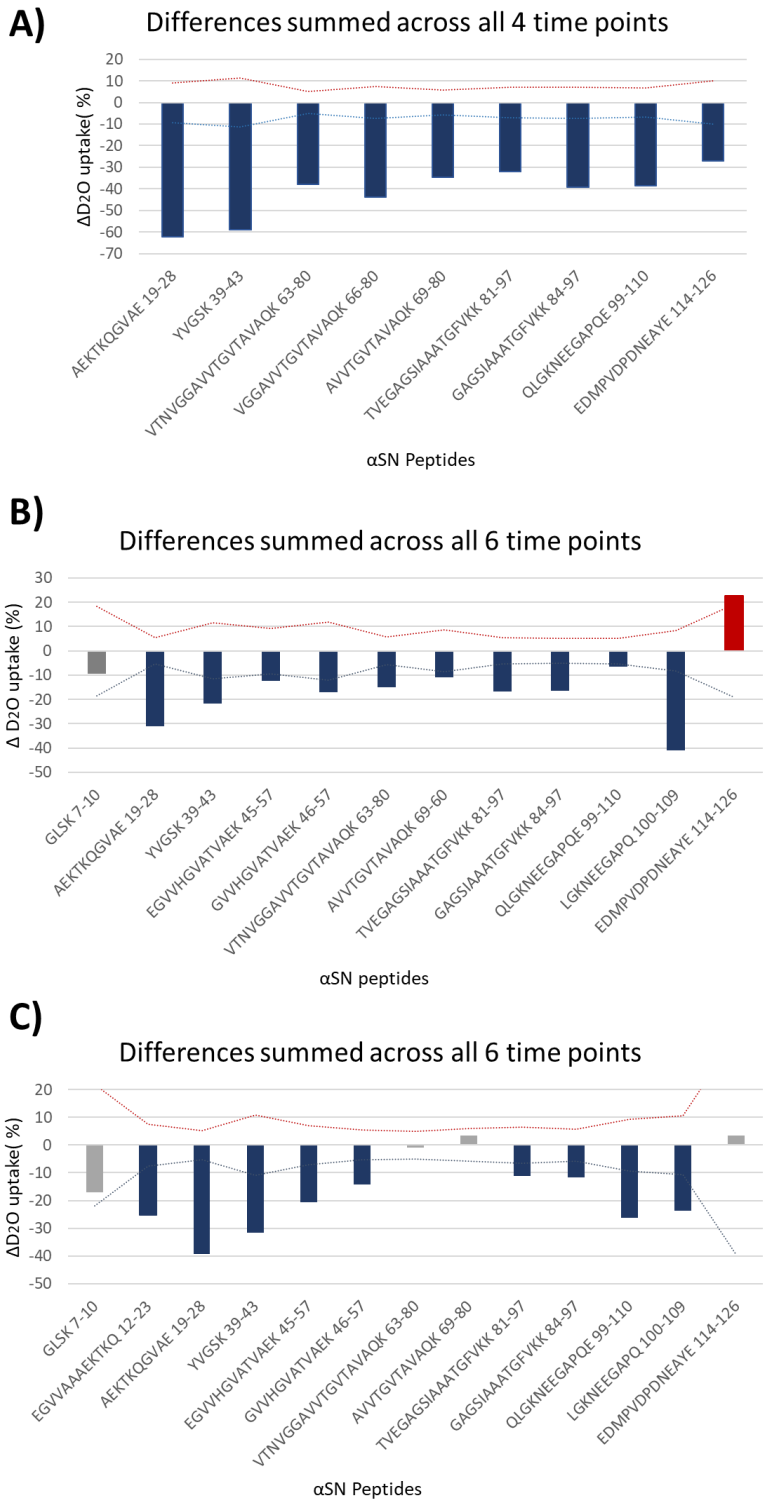

Figure 33. Summed deuterium uptake difference plot between A) αSN - 6 nm DMPC nanodisc complex and αSN alone, B) and C) αSN - 6 nm DMPC-POPS nanodisc complex and αSN alone. Blue color represents decrease in D_2O uptake, red increase, and grey - no significant change or no HDX data was obtained.

Such differences in the HDX profiles between all three plots in Figure 33 prevent from achieving any firm conclusions on the structural dynamics of the NAC region in the presence of the DMPC or DMPC-POPS nanodiscs. More replicates of the kinetic studies are needed in future.

The C-terminus peptides (amino acids 99-126) gave very infrequent deuterium uptake profiles as well. Overall, QLGKNEEGAPQE 99-110 and LGKNEEGAPQ 100-109 displayed decreases in deuterium uptake when exposed to the lipid bilayer of the nanodisc. EDMPVDPDNEAYE 114-126, in its turn, showed either decrease (plot A), increase (plot B), or no significant difference (plot C) in deuterium uptake. The HDX profiles for C-terminus peptides did not indicate any consistent structural behaviour during interaction with the lipid bilayer of the nanodiscs. However, it could be explained by the disordered character of the C-terminus which may form ensemble of different structural conformations resulting in different HDX results. The unexpected decreases in deuterium uptake mostly observed for LGKNEEGAPQ 100-109 were proposed to be result of assisting of this region in reducing αSN's disordered character towards a more folded species through the interaction with either regions of αSN or nanodiscs.

In conclusion, the kinetic studies have shown that αSN had exhibited rather transient interactions with the lipid membrane of the DMPC or DMPC-POPS nanodiscs. This deduction was supported by the recent NMR research by Viennet *et al.* which indicated no binding of αSN to the DMPC nanodisc or nanodiscs with less than 25% of negatively charged lipids [173]. However, compared to NMR, TRESI-HDX-MS (as a more sensitive technique to the structural perturbations in the amide backbone) was able to show that the presence of the nanodiscs resulted in the

transition of αSN towards a more conformationally-rigid structure. In addition, the overall decrease in deuterium uptake for the amphipathic region peptides compared to inconsistent HDX profiles for the other two regions of αSN could be the first indication of the partial-helical intermediate that was described by Dikiy and Eliezer in their model for the structural behaviour of this protein when interacting with synaptic vesicles (section 1.3.3.2. and Figure 14) [141].

Chapter 4: Conclusion and Future Work

4.1. Conclusion

The current study was successful in using TRESI-HDX-MS for the structural analysis of αSN in the presence of the nanodisc's phospholipid bilayer. Probing the dynamics of non- to weakly structured regions of αSN on the millisecond to seconds time scale has helped to elucidate the key regions involved in the structural changes during the protein-lipid interaction. Both equilibrium and kinetic studies have indicated the transient interaction of lipid-binding domain of αSN with the DMPC or DMPC-POPS nanodiscs, with the greatest transition to more structurally folded state in the amphipathic region of αSN. Nanodisc technology provided "nature-like" environment for αSN and gave more insights in possible *in vivo* conformational behavior of this protein, for example, the kinetic studies data could support the evidence for the formation of the partial-helical intermediate that was described by Dikiy and Eliezer.

The main research objective of this Master's thesis was to elucidate conformational dynamics of αSN's folding pathway into an extended-helix or broken-helix state. Understanding of the key transitional intermediates in this pathway may facilitate investigation for a drug that can stabilize the native folded state of αSN and prevent aggregation of this protein in neuronal cytosol.

4.2. Future Work

To address inconsistency issues in sections 3.5 and 3.6, as well as, complement the results in this research the set of future experiments was proposed. The main goals of the future experimental workflow are depicted in Figure 24.

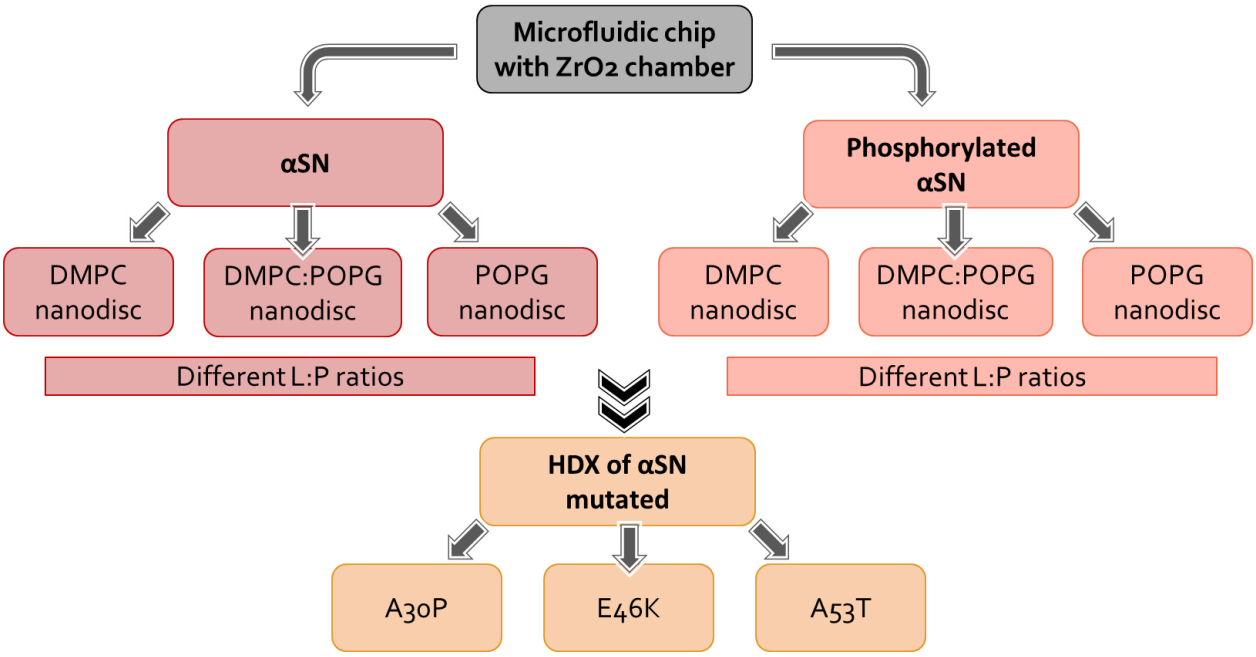

Figure 34. Diagram featuring the plan for future work experiments. The first step includes the implementation of microfluidic chip with zirconium oxide beads in TRESI-HDX-MS workflow. This will be followed by the testing of two different protein samples – αSN and phosphorylated αSN against three different nanodiscs (DMPC, DMPC:POPG, and POPG) with different lipid-to-protein ratios. Lat step involves testing mutated versions of αSN against DMPC, DMPC:POPG, and POPG nanodiscs with different lipid-to-protein ratios.

The first proposed improvement is the implementation of the second microfluidic chip filled with zirconium oxide beads right before ESI capillary in the TRESI set up. Zirconium oxide will help to clean up the sample from detergents and lipids which substantially supress peptide signal in MS. This will allow for a greater peptide coverage of the amphipathic region of αSN. Once TRESI system is successfully upgraded with zirconium oxide chip, TRESI-HDX-MS would be run on αSN with DMPC nanodiscs to obtain missing replicates. More negatively charged DMPC-POPG and

POPG nanodiscs will also be tested with αSN as actual binding with these two types of lipid bilayer nanodiscs was proved by Viennet *et al.* in 2018 [173]. Different lipid-to-protein (L:P) ratios were also proposed to be tried out due to the reported aggregation propensities of αSN in response to the different L:P ratios [172]. Similar to αSN TRESI-HDX-MS experiments are planned for the phosphorylated αSN. Phosphorylated αSN at Ser129 has been reported to enhance αSN's toxicity both *in vivo* and *in vitro*, possibly by increasing the formation of αSN's aggregates [174]. In a long-term future, TRESI-HDX-MS experiments with the three different nanodisc bilayers could be extended to the three main mutations in αSN (A30P, E46K and A53T) which were shown to exhibit an impact on the binding capacities to the vesicle's membrane *in vitro* [141].

References

1. Price, P. Standard Definitions of Terms Relating to Mass Spectrometry : A report from the Committee on Measurements and Standards of the American Society for Mass Spectrometry. *J. Am. Soc. Mass Spectrom.* **2,** 336–348 (1991).
2. Glish, G. L. & Vachet, R. W. The basics of mass spectrometry in the twenty-first century. *Nat. Rev. Drug Discov.* **2,** 140–150 (2003).
3. Wien, W. Untersuchungen über die electrische Entladung in verdünnten Gasen. *Ann. Phys.* **301,** 440–452 (1898).
4. Münzenberg, G. Development of mass spectrometers from Thomson and Aston to present. *Int. J. Mass Spectrom.* **349–350,** 9–18 (2013).
5. Thomson, P. S. J. J., M, O. & S, F. R. Bakerian Lecture:—Rays of positive electricity. *Proc. R. Soc. Lond. A* **89,** 1–20 (1913).
6. Tanaka, K. *et al.* Protein and polymer analyses up to m/z 100 000 by laser ionization time-of-flight mass spectrometry. *Rapid Commun. Mass Spectrom.* **2,** 151–153 (1988).
7. Fenn, J. B., Mann, M., Meng, C. K., Wong, S. F. & Whitehouse, C. M. Electrospray ionization for mass spectrometry of large biomolecules. *Science* **246,** 64–71 (1989).
8. Fenn, J. B. Electrospray Wings for Molecular Elephants (Nobel Lecture). *Angew. Chemie Int. Ed.* **42,** 3871–3894 (2003).
9. The Nobel Prize in Chemistry 2002. Available at: https://www.nobelprize.org/nobel_prizes/chemistry/laureates/2002/.
10. Englander, S. W., Downer, N. W. & Teitelbaum, and H. Hydrogen Exchange. *Annu. Rev. Biochem.* **41,** 903–924 (1972).
11. Englander, S. W., Mayne, L., Bai, Y. & Sosnick, T. R. Hydrogen exchange: the modern legacy of Linderstrøm-Lang. *Protein Sci.* **6,** 1101–1109 (1997).
12. Oganesyan, I., Lento, C. & Wilson, D. J. Contemporary hydrogen deuterium exchange mass spectrometry. *Methods* (2018). doi:10.1016/J.YMETH.2018.04.023
13. Hvidt, A. & Linderstrøm-Lang, K. Exchange of hydrogen atoms in insulin with deuterium atoms in aqueous solutions. *Biochim. Biophys. Acta* **14,** 574–575 (1954).
14. Hvidt, A., Johansen, G., Linderstrøm Lang, K. & Vaslow, F. Exchange of deuterium and

18O between water and other substances. I. Methods. *C. R. Trav. Lab. Carlsberg. Chim.* **29,** 129–157 (1954).

15. Hvidt, A. & Linderstrøm-Lang, K. Exchange in deuterium and 18O between water and other substances. 3. Deuterium exchnage of short peptides, Sanger's A-chain and insulin. *C. R. Trav. Lab. Carlsberg. Chim.* **29,** 385–402 (1955).
16. Hvidt, A. Deuterium exchange between ribonuclease and water. *Biochim. Biophys. Acta* **18,** 306–308 (1955).
17. Linderstrøm-Lang, K. Deuterium exchange between peptides and water. *Chem. Soc. Spec. Publ* **2,** 1–20 (1955).
18. Krause, I. M. & Linderstrøm-Lang, K. Exchange in deuterium and 18O between water and other substances. 2. Alternative Methods. *C. R. Trav. Lab. Carlsberg. Chim.* **29,** 367–384 (1955).
19. Berger, A. & Linderstrøm-Lang, K. Deuterium exchange of poly-dl-alanine in aqueous solution. *Arch. Biochem. Biophys.* **69,** 106–118 (1957).
20. Benson, E. E. & Linderstrøm-Lang, K. Deuterium exchange between myoglobin and water. *Biochim. Biophys. Acta* **32,** 579–581 (1959).
21. Hvidt, A. & Nielsen, S. O. Hydrogen exchange in proteins. *Adv. Protein Chem.* **21,** 287–386 (1966).
22. Linderstrøm-Lang, K. Deuterium Exchnage and Protein Structure. in *Symposium on Protein Structure* (ed. Neuberger, A.) 23–34 (Methuen, 1958).
23. Konermann, L., Pan, J. & Liu, Y.-H. Hydrogen exchange mass spectrometry for studying protein structure and dynamics. *Chem. Soc. Rev.* **40,** 1224–1234 (2011).
24. Engen, J. R. & Smith, D. L. Peer Reviewed: Investigating Protein Structure and Dynamics by Hydrogen Exchange MS. *Anal. Chem.* **73,** 256 A-265 A (2001).
25. Masson, G. R., Jenkins, M. L. & Burke, J. E. An overview of hydrogen deuterium exchange mass spectrometry (HDX-MS) in drug discovery. *Expert Opin. Drug Discov.* **12,** 981–994 (2017).
26. Eyles, S. J. & Kaltashov, I. A. Methods to study protein dynamics and folding by mass spectrometry. *Methods* **34,** 88–99 (2004).

27. Suchanova, B. & Tuma, R. Folding and assembly of large macromolecular complexes monitored by hydrogen-deuterium exchange and mass spectrometry. *Microb. Cell Fact.* **7,** 12 (2008).
28. Eigen, M. Proton Transfer, Acid-Base Catalysis, and Enzymatic Hydrolysis. Part I: ELEMENTARY PROCESSES. *Angew. Chemie Int. Ed. English* **3,** 1–19 (1964).
29. Marcsisin, S. R. & Engen, J. R. Hydrogen exchange mass spectrometry: what is it and what can it tell us? *Anal. Bioanal. Chem.* **397,** 967–972 (2010).
30. Wales, T. E. & Engen, J. R. Hydrogen exchange mass spectrometry for the analysis of protein dynamics. *Mass Spectrom. Rev.* **25,** 158–170 (2006).
31. Engen, J. R. Analysis of protein conformation and dynamics by hydrogen/deuterium exchange MS. *Anal. Chem.* **81,** 7870–5 (2009).
32. Hoofnagle, A. N., Resing, K. A. & Ahn, N. G. Protein analysis by hydrogen exchange mass spectrometry. *Annu. Rev. Biophys. Biomol. Struct.* **32,** 1–25 (2003).
33. Wei, H. *et al.* Hydrogen/deuterium exchange mass spectrometry for probing higher order structure of protein therapeutics: methodology and applications. *Drug Discov. Today* **19,** 95–102 (2014).
34. Chait, B. T. Mass spectrometry — a useful tool for the protein X-ray crystallographer and NMR spectroscopist. *Structure* **2,** 465–467 (1994).
35. Lento, C., Wilson, D. J. & Audette, G. F. Dimerization of the type IV pilin from Pseudomonas aeruginosa strain K122-4 results in increased helix stability as measured by time-resolved hydrogen-deuterium exchange. *Struct. Dyn.* **3,** (2015).
36. Zhu, S., Campbell, J. L., Chernushevich, I., Le Blanc, J. C. Y. & Wilson, D. J. Differential Mobility Spectrometry-Hydrogen Deuterium Exchange (DMS-HDX) as a Probe of Protein Conformation in Solution. *J. Am. Soc. Mass Spectrom.* **27,** 991–999 (2016).
37. Liuni, P., Olkhov-Mitsel, E., Orellana, A. & Wilson, D. J. Measuring Kinetic Isotope Effects in Enzyme Reactions Using Time-Resolved Electrospray Mass Spectrometry. *Anal. Chem.* **85,** 3758–3764 (2013).
38. Brown, K. A. *et al.* Distinct Dynamic Modes Enable the Engagement of Dissimilar Ligands in a Promiscuous Atypical RNA Recognition Motif. *Biochemistry* **55,** 7141–7150 (2016).

39. Resetca, D., Haftchenary, S., Gunning, P. T. & Wilson, D. J. Changes in signal transducer and activator of transcription 3 (STAT3) dynamics induced by complexation with pharmacological inhibitors of Src homology 2 (SH2) domain dimerization. *J. Biol. Chem.* **289,** 32538–47 (2014).
40. Gallagher, E. S. & Hudgens, J. W. in *Methods in enzymology* **566,** 357–404 (2016).
41. Schellman, J. A. & Schellman, C. G. Kaj Ulrik Linderstrøm-Lang (1896–1959). *Protein Sci.* **6,** 1092–1100 (1997).
42. Englander, S. W. Hydrogen Exchange and Mass Spectrometry: A Historical Perspective. *J. Am. Soc. Mass Spectrom.* **17,** 1481–1489 (2006).
43. Bai, Y., Milne, J. S., Mayne, L. & Englander, S. W. Primary structure effects on peptide group hydrogen exchange. *Proteins Struct. Funct. Genet.* **17,** 75–86 (1993).
44. Kaltashov, I. A. & A., I. Probing protein dynamics and function under native and mildly denaturing conditions with hydrogen exchange and mass spectrometry. *Int. J. Mass Spectrom.* **240,** 249–259 (2005).
45. Smith, D. L., Deng, Y. & Zhang, Z. Probing the Non-covalent Structure of Proteins by Amide Hydrogen Exchange and Mass Spectrometry. *J. Mass Spectrom.* **32,** 135–146 (1997).
46. Venable, J. D., Okach, L., Agarwalla, S. & Brock, A. Subzero Temperature Chromatography for Reduced Back-Exchange and Improved Dynamic Range in Amide Hydrogen/Deuterium Exchange Mass Spectrometry. *Anal. Chem.* **84,** 9601–9608 (2012).
47. Englander, S. W. & Kallenbach, N. R. Hydrogen exchange and structural dynamics of proteins and nucleic acids. *Q. Rev. Biophys.* **16,** 521–655 (1983).
48. Dempsey, C. E. Hydrogen exchange in peptides and proteins using NMR spectroscopy. *Prog. Nucl. Magn. Reson. Spectrosc.* **39,** 135–170 (2001).
49. Baldwin, R. L. Early days of protein hydrogen exchange: 1954–1972. *Proteins Struct. Funct. Bioinforma.* **79,** 2021–2026 (2011).
50. Molday, R. S., Englander, S. W. & Kallen, R. G. Primary structure effects on peptide group hydrogen exchange. *Biochemistry* **11,** 150–158 (1972).
51. Brown, K. A. & Wilson, D. J. Bottom-up hydrogen deuterium exchange mass

spectrometry: data analysis and interpretation. *Analyst* **142,** 2874–2886 (2017).

52. Hvidt, A. & Linderstrøm-Lang, K. The kinetics of the deuterium exchange of insulin with D2O; an amendment. *Biochim. Biophys. Acta* **16,** 168–169 (1955).
53. Konermann, L., Tong, X. & Pan, Y. Protein structure and dynamics studied by mass spectrometry: H/D exchange, hydroxyl radical labeling, and related approaches. *J. Mass Spectrom.* **43,** 1021–1036 (2008).
54. Guttman, M. & Lee, K. K. Isotope Labeling of Biomolecules: Structural Analysis of Viruses by HDX-MS. *Methods Enzymol.* **566,** 405–426 (2016).
55. Ens, W. & Standing, K. G. Hybrid Quadrupole/Time-of-Flight Mass Spectrometers for Analysis of Biomolecules. *Methods Enzymol.* **402,** 49–78 (2005).
56. Scigelova, M. & Makarov, A. Orbitrap Mass Analyzer – Overview and Applications in Proteomics. *Proteomics* **6,** 16–21 (2006).
57. Lanucara, F., Holman, S. W., Gray, C. J. & Eyers, C. E. The power of ion mobility-mass spectrometry for structural characterization and the study of conformational dynamics. *Nat. Publ. Gr.* **6,** (2014).
58. Udgaonkar, J. B. & Baldwin, R. L. NMR evidence for an early framework intermediate on the folding pathway of ribonuclease A. *Nature* **335,** 694–699 (1988).
59. Roder, H., Elöve, G. A. & Englander, S. W. Structural characterization of folding intermediates in cytochrome c by H-exchange labelling and proton NMR. *Nature* **335,** 700–4 (1988).
60. and, K. D. & Smith*, D. L. Mass Spectrometric Determination of Isotopic Exchange Rates of Amide Hydrogens Located on the Surfaces of Proteins. (1996). doi:10.1021/AC9601526
61. Konermann, L. & Simmons, D. A. Protein-folding kinetics and mechanisms studied by pulse-labeling and mass spectrometry. *Mass Spectrom. Rev.* **22,** 1–26 (2003).
62. Rob, T. *et al.* Measuring Dynamics in Weakly Structured Regions of Proteins Using Microfluidics-Enabled Subsecond H/D Exchange Mass Spectrometry. *Anal. Chem.* **84,** 3771–3779 (2012).
63. Lento, C., Audette, G. F. & Wilson, D. J. Time-resolved electrospray mass spectrometry —

a brief history. *Can. J. Chem.* **93,** 7–12 (2015).

64. Lento, C. *et al.* Time-resolved ElectroSpray Ionization Hydrogen-deuterium Exchange Mass Spectrometry for Studying Protein Structure and Dynamics. *J. Vis. Exp.* (2017). doi:10.3791/55464

65. Lento, C., Ferraro, M., Wilson, D. & Audette, G. F. HDX-MS and deletion analysis of the type 4 secretion system protein TraF from the *Escherichia coli* F plasmid. *FEBS Lett.* **590,** 376–386 (2016).

66. Zhu, S., Khatun, R., Lento, C., Sheng, Y. & Wilson, D. J. Enhanced Binding Affinity via Destabilization of the Unbound State: A Millisecond Hydrogen–Deuterium Exchange Study of the Interaction between p53 and a Pleckstrin Homology Domain. *Biochemistry* **56,** 4127–4133 (2017).

67. Deng, B., Lento, C. & Wilson, D. J. Hydrogen deuterium exchange mass spectrometry in biopharmaceutical discovery and development - A review. *Anal. Chim. Acta* **940,** 8–20 (2016).

68. Lugo, M. R., Lyons, B., Lento, C., Wilson, D. J. & Merrill, A. R. Dynamics of Scabin toxin. A proposal for the binding mode of the DNA substrate. *PLoS One* **13,** e0194425 (2018).

69. Zhu, S. *et al.* Hyperphosphorylation of Intrinsically Disordered Tau Protein Induces an Amyloidogenic Shift in Its Conformational Ensemble. *PLoS One* **10,** e0120416 (2015).

70. Dunker, A. K. *et al.* Intrinsically disordered protein. *J. Mol. Graph. Model.* **19,** 26–59 (2001).

71. Dyson, H. J. & Wright, P. E. Intrinsically unstructured proteins and their functions. *Nat. Rev. Mol. Cell Biol.* **6,** 197–208 (2005).

72. Wright, P. E. & Dyson, H. J. Intrinsically unstructured proteins: re-assessing the protein structure-function paradigm. *J. Mol. Biol.* **293,** 321–331 (1999).

73. Iakoucheva, L. M. *et al.* The importance of intrinsic disorder for protein phosphorylation. *Nucleic Acids Res.* **32,** 1037–1049 (2004).

74. Iakoucheva, L. M., Brown, C. J., Lawson, J. D., Obradović, Z. & Dunker, A. K. Intrinsic disorder in cell-signaling and cancer-associated proteins. *J. Mol. Biol.* **323,** 573–84 (2002).

75. Tompa, P. Intrinsically unstructured proteins. *Trends Biochem. Sci.* **27,** 527–33 (2002).

76. Resetca, D., Haftchenary, S., Gunning, P. T. & Wilson, D. J. Changes in Signal Transducer and Activator of Transcription 3 (STAT3) Dynamics Induced by Complexation with Pharmacological Inhibitors of Src Homology 2 (SH2) Domain Dimerization. *J. Biol. Chem.* **289,** 32538–32547 (2014).
77. Zhu, S. Characterization of Structures and Dynamics of Intrinsically Disordered Domain and Proteins Using Time Resolved-Hydrogen Deuterium Exchange Mass Spectrometry. (York University, 2017).
78. Bartels, T. *et al.* The N-Terminus of the Intrinsically Disordered Protein α-Synuclein Triggers Membrane Binding and Helix Folding. *Biophys. J.* **99,** 2116–2124 (2010).
79. Wallin, E. & Heijne, G. Von. Genome-wide analysis of integral membrane proteins from eubacterial, archaean, and eukaryotic organisms. *Protein Sci.* **7,** 1029–1038 (2008).
80. Terstappen, G. C. & Reggiani, A. In silico research in drug discovery. *Trends Pharmacol. Sci.* **22,** 23–6 (2001).
81. Moraes, I., Evans, G., Sanchez-Weatherby, J., Newstead, S. & Stewart, P. D. S. Membrane protein structure determination - the next generation. *Biochim. Biophys. Acta* **1838,** 78–87 (2014).
82. Almén, M. S., Nordström, K. J. V, Fredriksson, R. & Schiöth, H. B. Mapping the human membrane proteome: a majority of the human membrane proteins can be classified according to function and evolutionary origin. *BMC Biol.* **7,** 50 (2009).
83. Lin, Y. *et al.* The substitution of Arg149 with Cys fixes the melibiose transporter in an inward-open conformation. *Biochim. Biophys. Acta - Biomembr.* **1828,** 1690–1699 (2013).
84. Landreh, M. & Robinson, C. V. A new window into the molecular physiology of membrane proteins. *J. Physiol.* **593,** 355–362 (2015).
85. Cournia, Z. *et al.* Membrane Protein Structure, Function, and Dynamics: a Perspective from Experiments and Theory. *J. Membr. Biol.* **248,** 611–640 (2015).
86. Almeida, J. G., Preto, A. J., Koukos, P. I., Bonvin, A. M. J. J. & Moreira, I. S. Membrane proteins structures: A review on computational modeling tools. *Biochim. Biophys. Acta - Biomembr.* **1859,** 2021–2039 (2017).
87. Engel, A. & Gaub, H. E. Structure and Mechanics of Membrane Proteins. (2008).

doi:10.1146/annurev.biochem.77.062706.154450

88. Carpenter, E. P., Beis, K., Cameron, A. D. & Iwata, S. Overcoming the challenges of membrane protein crystallography. *Curr. Opin. Struct. Biol.* **18,** 581–6 (2008).

89. Seddon, A. M., Curnow, P. & Booth, P. J. Membrane proteins, lipids and detergents: not just a soap opera. *Biochim. Biophys. Acta - Biomembr.* **1666,** 105–117 (2004).

90. Drew, D., Fröderberg, L., Baars, L. & de Gier, J.-W. L. Assembly and overexpression of membrane proteins in *Escherichia coli*. *Biochim. Biophys. Acta* **1610,** 3–10 (2003).

91. Kalipatnapu, S. & Chattopadhyay, A. Critical Review Membrane Protein Solubilization: Recent Advances and Challenges in Solubilization of Serotonin 1A Receptors. doi:10.1080/15216540500167237

92. Smith, S. M. in *Methods in molecular biology (Clifton, N.J.)* **1485,** 389–400 (2017).

93. Antignac, J.-P. *et al.* The ion suppression phenomenon in liquid chromatography-mass spectrometry and its consequences in the field of residue analysis. *Anal. Chim. Acta* **529,** 129–136 (2005).

94. Annesley, T. M. Ion suppression in mass spectrometry. *Clin. Chem.* **49,** 1041–4 (2003).

95. MiliÄ‡, D. & Veprintsev, D. B. Large-scale production and protein engineering of G protein-coupled receptors for structural studies. *Front. Pharmacol.* **6,** 66 (2015).

96. Dü, U. H. N., Gildenberg, M. & Ramamoorthy, A. The Magic of Bicelles Lights Up Membrane Protein Structure. *Chem. Rev*. 112 (11), 6054-6074 (2012). doi:10.1021/cr300061w

97. Catoire, L. J. *et al.* 2.1 Introduction Micelles, Bicelles, Amphipols, Nanodiscs, Liposomes, or Intact Cells: The Hitchhiker's Guide to the Study of Membrane Proteins by NMR. doi:10.1007/978-1-4939-0662-8_12

98. Laganowsky, A., Reading, E., Hopper, J. T. S. & Robinson, C. V. Mass spectrometry of intact membrane protein complexes. *Nat. Protoc.* **8,** 639–651 (2013).

99. Akbarzadeh, A. *et al.* Liposome: classification, preparation, and applications. *Nanoscale Res. Lett.* **8,** 102 (2013).

100. Seigneuret, M. & Rigaud, J.-L. Use of the fluorescent pH probe pyranine to detect heterogeneous directions of proton movement in bacteriorhodopsin reconstituted large

liposomes. *FEBS Lett.* **188,** 101–106 (1985).

101. Lu, Z. *et al.* Bicelles at low concentrations. *Mol. Pharm.* **9,** 752–61 (2012).
102. Denisov, I. G. & Sligar, S. G. Nanodiscs for structural and functional studies of membrane proteins. *Nat. Struct. Mol. Biol.* **23,** 481–486 (2016).
103. Timothy H. Bayburt, †, Yelena V. Grinkova, † and & Stephen G. Sligar*, †,‡,§. Self-Assembly of Discoidal Phospholipid Bilayer Nanoparticles with Membrane Scaffold Proteins. (2002). doi:10.1021/NL025623K
104. Schuler, M. A., Denisov, I. G. & Sligar, S. G. Nanodiscs as a new tool to examine lipid-protein interactions. *Methods Mol. Biol.* **974,** 415–33 (2013).
105. Nath, A., Atkins, W. M. & Sligar, S. G. Applications of Phospholipid Bilayer Nanodiscs in the Study of Membranes and Membrane Proteins. doi:10.1021/bi602371n
106. Rouck, J. E., Krapf, J. E., Roy, J., Huff, H. C. & Das, A. Recent advances in nanodisc technology for membrane protein studies (2012-2017). *FEBS Lett.* **591,** 2057–2088 (2017).
107. Grinkova, Y. V, Denisov, I. G. & Sligar, S. G. Engineering extended membrane scaffold proteins for self-assembly of soluble nanoscale lipid bilayers. *Protein Eng. Des. Sel.* **23,** 843–8 (2010).
108. Hagn, F., Etzkorn, M., Raschle, T. & Wagner, G. Optimized Phospholipid Bilayer Nanodiscs Facilitate High-Resolution Structure Determination of Membrane Proteins. doi:10.1021/ja310901f
109. Denisov, I. G. & Sligar, S. G. Nanodiscs in Membrane Biochemistry and Biophysics. *Chem. Rev.* **117,** 4669–4713 (2017).
110. Bender, G., Schexnaydre, E. E., Murphy, R. C., Uhlson, C. & Newcomer, M. E. Membrane-dependent Activities of Human 15-LOX-2 and Its Murine Counterpart. *J. Biol. Chem.* **291,** 19413–19424 (2016).
111. Yin, L., Kim, J. & Shin, Y.-K. Complexin splits the membrane-proximal region of a single SNAREpin. *Biochem. J.* **473,** 2219–24 (2016).
112. Hu, A. *et al.* Soft Matter Lipid-based nanodiscs as models for studying mesoscale coalescence – a transport limited case Lipid-based nanodiscs as models for studying

mesoscale coalescence – a transport limited case. **10,** 5019–5222 (2014).

113. Denisov, I. G., McLean, M. A., Shaw, A. W., Grinkova, Y. V & Sligar, S. G. Thermotropic phase transition in soluble nanoscale lipid bilayers. *J. Phys. Chem. B* **109,** 15580–8 (2005).
114. Shaw, A. W., McLean, M. A. & Sligar, S. G. Phospholipid phase transitions in homogeneous nanometer scale bilayer discs. *FEBS Lett.* **556,** 260–4 (2004).
115. Denisov, I. G. & Sligar, S. G. Nanodiscs for structural and functional studies of membrane proteins. *Nat. Struct. Mol. Biol.* (2016). doi:10.1038/nsmb.3195
116. Rouck, J. E., Krapf, J. E., Roy, J., Huff, H. C. & Das, A. Recent advances in nanodisc technology for membrane protein studies (2012-2017). *FEBS Lett.* **591,** 2057–2088 (2017).
117. Hebling, C. M. *et al.* Conformational Analysis of Membrane Proteins in Phospholipid Bilayer Nanodiscs by Hydrogen Exchange Mass Spectrometry. *Anal. Chem.* **82,** 5415–5419 (2010).
118. Parker, C. H. *et al.* A conformational investigation of propeptide binding to the integral membrane protein γ-glutamyl carboxylase using nanodisc hydrogen exchange mass spectrometry. *Biochemistry* **53,** 1511–20 (2014).
119. Postis, V. *et al.* The use of SMALPs as a novel membrane protein scaffold for structure study by negative stain electron microscopy. *Biochim. Biophys. Acta - Biomembr.* **1848,** 496–501 (2015).
120. Pollock, N. L., Lee, S. C., Patel, J. H., Gulamhussein, A. A. & Rothnie, A. J. Structure and function of membrane proteins encapsulated in a polymer-bound lipid bilayer. *Biochim. Biophys. Acta - Biomembr.* **1860,** 809–817 (2018).
121. Uversky, V. N. Wrecked regulation of intrinsically disordered proteins in diseases: pathogenicity of deregulated regulators. *Front. Mol. Biosci.* **1,** 6 (2014).
122. Uversky, V. N., Gillespie, J. R. & Fink, A. L. Why are ?natively unfolded? proteins unstructured under physiologic conditions? *Proteins Struct. Funct. Genet.* **41,** 415–427 (2000).
123. Uversky, V. N. & Dunker, A. K. Understanding protein non-folding. *Biochim. Biophys. Acta* **1804,** 1231–64 (2010).

124. Uversky, V. N., Oldfield, C. J. & Dunker, A. K. Intrinsically Disordered Proteins in Human Diseases: Introducing the D 2 Concept. (2008). doi:10.1146/annurev.biophys.37.032807.125924

125. Uversky, V. N. & Eliezer, D. Biophysics of Parkinson's disease: structure and aggregation of alpha-synuclein. *Curr. Protein Pept. Sci.* **10,** 483–99 (2009).

126. Madan Babu, M. *et al.* Intrinsically disordered proteins: regulation and disease This review comes from a themed issue on Sequences and topology Edited. *Curr. Opin. Struct. Biol.* **21,** 1–9 (2011).

127. Kirkitadze, M. D., Condron, M. M. & Teplow, D. B. Identification and characterization of key kinetic intermediates in amyloid β-protein fibrillogenesis11Edited by F. Cohen. *J. Mol. Biol.* **312,** 1103–1119 (2001).

128. Hollstein, M., Sidransky, D., Vogelstein, B. & Harris, C. C. p53 mutations in human cancers. *Science* **253,** 49–53 (1991).

129. Yacoubian, T. A. Neurodegenerative Disorders: Why Do We Need New Therapies? *Drug Discov. Approaches Treat. Neurodegener. Disord.* 1–16 (2017). doi:10.1016/B978-0-12-802810-0.00001-5

130. Lotharius, J. & Brundin, P. Pathogenesis of parkinson's disease: dopamine, vesicles and α-synuclein. *Nat. Rev. Neurosci.* **3,** 932–942 (2002).

131. de Rijk, M. C. *et al.* Prevalence of parkinsonism and Parkinson's disease in Europe: the EUROPARKINSON Collaborative Study. European Community Concerted Action on the Epidemiology of Parkinson's disease. *J. Neurol. Neurosurg. Psychiatry* **62,** 10–5 (1997).

132. FERNANDEZ, H. H. 2015 Update on Parkinson disease. *Cleve. Clin. J. Med.* **82,** 563–568 (2015).

133. Heisters, D. Parkinson's: symptoms, treatments and research. *Br. J. Nurs.* **20,** 548–554 (2011).

134. Lücking, C. B. & Brice*, A. Alpha-synuclein and Parkinson's disease. *Cell. Mol. Life Sci.* **57,** 1894–1908 (2000).

135. Cookson, M. R. Molecular Neurodegeneration α-Synuclein and neuronal cell death. (2009). doi:10.1186/1750-1326-4-9

136. Lanciego, J. L., Luquin, N. & Obeso, J. A. Functional neuroanatomy of the basal ganglia. *Cold Spring Harb. Perspect. Med.* **2,** a009621 (2012).
137. Graybiel, A. M. Basal ganglia: New therapeutic approaches to Parkinson's disease. *Curr. Biol.* **6,** 368–371 (1996).
138. Lotharius, J. & Brundin, P. Pathogenesis of parkinson's disease: dopamine, vesicles and α-synuclein. *Nat. Rev. Neurosci.* **3,** 932–942 (2002).
139. Burre, J. *et al.* -Synuclein Promotes SNARE-Complex Assembly in Vivo and in Vitro. *Science (80-.).* **329,** 1663–1667 (2010).
140. Stefanis, L. α-Synuclein in Parkinson's disease. *Cold Spring Harb. Perspect. Med.* **2,** a009399 (2012).
141. Dikiy, I. & Eliezer, D. Folding and misfolding of alpha-synuclein on membranes. *Biochim. Biophys. Acta - Biomembr.* **1818,** 1013–1018 (2012).
142. Alderson, T. R. & Markley, J. L. Biophysical characterization of α-synuclein and its controversial structure. *Intrinsically Disord. Proteins* **1,** e26255 (2013).
143. Allen Reish, H. E. & Standaert, D. G. Role of α-synuclein in inducing innate and adaptive immunity in Parkinson disease. *J. Parkinsons. Dis.* **5,** 1–19 (2015).
144. Xu, L. & Pu, J. Alpha-Synuclein in Parkinson's Disease: From Pathogenetic Dysfunction to Potential Clinical Application. *Parkinsons. Dis.* **2016,** 1720621 (2016).
145. Collier, T. J. *et al.* Is Alpha-Synuclein Loss-of-Function a Contributor to Parkinsonian Pathology? Evidence from Non-human Primates. *Front. Neurosci.* **10,** 12 (2016).
146. Breydo, L., Wu, J. W. & Uversky, V. N. α-Synuclein misfolding and Parkinson's disease. *Biochim. Biophys. Acta - Mol. Basis Dis.* **1822,** 261–285 (2012).
147. Payton, J. E., Perrin, R. J., Clayton, D. F. & George, J. M. Protein-protein interactions of alpha-synuclein in brain homogenates and transfected cells. *Brain Res. Mol. Brain Res.* **95,** 138–45 (2001).
148. Uversky, V. N. Alpha-synuclein misfolding and neurodegenerative diseases. *Curr. Protein Pept. Sci.* **9,** 507–40 (2008).
149. Dev, K. K., Hofele, K., Barbieri, S., Buchman, V. L. & van der Putten, H. Part II: α-synuclein and its molecular pathophysiological role in neurodegenerative disease.

Neuropharmacology **45,** 14–44 (2003).

150. Steiner, J. A., Quansah, E. & Brundin, P. The concept of alpha-synuclein as a prion-like protein: ten years after. *Cell Tissue Res.* **373,** 161–173 (2018).
151. Lashuel, H. A., Hartley, D., Petre, B. M., Walz, T. & Lansbury, P. T. Neurodegenerative disease: Amyloid pores from pathogenic mutations. *Nature* **418,** 291–291 (2002).
152. Volles, M. J. & Lansbury, P. T. Vesicle permeabilization by protofibrillar alpha-synuclein is sensitive to Parkinson's disease-linked mutations and occurs by a pore-like mechanism. *Biochemistry* **41,** 4595–602 (2002).
153. Soper, J. H. *et al.* Alpha-synuclein-induced aggregation of cytoplasmic vesicles in Saccharomyces cerevisiae. *Mol. Biol. Cell* **19,** 1093–103 (2008).
154. Galvagnion, C. *et al.* Lipid vesicles trigger α-synuclein aggregation by stimulating primary nucleation. *Nat. Chem. Biol.* **11,** 229–34 (2015).
155. Cordeiro, Y., Macedo, B., Silva, J. L. & Gomes, M. P. B. Pathological implications of nucleic acid interactions with proteins associated with neurodegenerative diseases. *Biophys. Rev.* **6,** 97–110 (2014).
156. Villar-Piqué, A., Lopes da Fonseca, T. & Outeiro, T. F. Structure, function and toxicity of alpha-synuclein: the Bermuda triangle in synucleinopathies. *J. Neurochem.* **139,** 240–255 (2016).
157. Bertoncini, C. W. *et al.* From The Cover: Release of long-range tertiary interactions potentiates aggregation of natively unstructured -synuclein. *Proc. Natl. Acad. Sci.* **102,** 1430–1435 (2005).
158. Uversky, V. N. What does it mean to be natively unfolded?
159. Uversky, V. N. A Protein-Chameleon: Conformational Plasticity of α-Synuclein, a Disordered Protein Involved in Neurodegenerative Disorders. *J. Biomol. Struct. Dyn.* **21,** (2003).
160. Auluck, P. K., Caraveo, G. & Lindquist, S. α-Synuclein: Membrane Interactions and Toxicity in Parkinson's Disease. *Annu. Rev. Cell Dev. Biol* **26,** 211–233 (2010).
161. Chandra, S., Chen, X., Rizo, J., Jahn, R. & Südhof, T. C. A broken alpha -helix in folded alpha -Synuclein. *J. Biol. Chem.* **278,** 15313–8 (2003).

162. Ulmer, T. S., Bax, A., Cole, N. B. & Nussbaum, R. L. Structure and Dynamics of Micelle-bound Human -Synuclein. *J. Biol. Chem.* **280,** 9595–9603 (2005).
163. Bussell, R. & Eliezer, D. A structural and functional role for 11-mer repeats in alpha-synuclein and other exchangeable lipid binding proteins. *J. Mol. Biol.* **329,** 763–78 (2003).
164. Georgieva, E. R., Ramlall, T. F., Borbat, P. P., Freed, J. H. & Eliezer, D. The Lipid-binding Domain of Wild Type and Mutant α-Synuclein. *J. Biol. Chem.* **285,** 28261–28274 (2010).
165. Georgieva, E. R., Ramlall, T. F., Borbat, P. P., Freed, J. H. & Eliezer, D. Membrane-Bound α-Synuclein Forms an Extended Helix: Long-Distance Pulsed ESR Measurements Using Vesicles, Bicelles, and Rodlike Micelles. *J. Am. Chem. Soc.* **130,** 12856–12857 (2008).
166. Gattiker, A., Bienvenut, W. V., Bairoch, A. & Gasteiger, E. FindPept, a tool to identify unmatched masses in peptide mass fingerprinting protein identification. *Proteomics* **2,** 1435–1444 (2002).
167. Rey, M. *et al.* Mass spec studio for integrative structural biology. *Structure* **22,** 1538–48 (2014).
168. PyMOL | pymol.org. Available at: https://pymol.org/2/.
169. Fink, A. L. The Aggregation and Fibrillation of α-Synuclein. *Acc. Chem. Res.* **39,** 628–634 (2006).
170. Lucyanna, B.-B. *et al.* Structural Versatility of Bicellar Systems and Their Possibilities as Colloidal Carriers. *Pharmaceutics* **3,** 636–664 (2011).
171. Hebling, C. M. *et al.* Conformational Analysis of Membrane Proteins in Phospholipid Bilayer Nanodiscs by Hydrogen Exchange Mass Spectrometry. *Anal. Chem.* **82,** 5415–5419 (2010).
172. Galvagnion, C. The Role of Lipids Interacting with α-Synuclein in the Pathogenesis of Parkinson's Disease. *J. Parkinsons. Dis.* **7,** 433–450 (2017).
173. Viennet, T. *et al.* Structural insights from lipid-bilayer nanodiscs link α-Synuclein membrane-binding modes to amyloid fibril formation. *Commun. Biol.* **1,** 44 (2018).
174. Wang, Y. *et al.* Phosphorylated α-synuclein in Parkinson's disease. *Sci. Transl. Med.* **4,** 121ra20 (2012).